7-2020

Nanoscale Carbon-Based Electrochemical and Temperature Sensors

Olivia Viola Scheibel
ovs8379@rit.edu

Recommended Citation

Scheibel, Olivia Viola, "Nanoscale Carbon-Based Electrochemical and Temperature Sensors" (2020). Thesis. Rochester Institute of Technology. Accessed from

R·I·T

NANOSCALE CARBON-BASED ELECTROCHEMICAL AND TEMPERATURE SENSORS

by

Olivia Viola Scheibel

A dissertation submitted in partial fulfillment of the requirements
for the degree of Doctorate of Philosophy in Engineering

PhD Engineering Program
Kate Gleason College of Engineering

Rochester Institute of Technology
Rochester, New York
July, 2020

Nanoscale Carbon-Based Electrochemical and Temperature Sensors

by

Olivia Viola Scheibel

Committee Approval:

We, the undersigned committee members, certify that we have advised and/or supervised the candidate on the work described in this dissertation. We further certify that we have reviewed the dissertation manuscript and approve it in partial fulfillment of the requirements of the degree of Doctor of Philosophy in Engineering.

Michael Schrlau, Ph.D. Date
Associate Professor of Mechanical Engineering

Christopher Collison, Ph.D. Date
Professor of Chemistry

Thomas Gaborski, Ph.D. Date
Associate Professor of Biomedical Engineering

Michael Schertzer, Ph.D. Date
Associate Professor of Mechanical Engineering

Certified by:

Edward Hensel, Ph.D. Date
Director, PhD Engineering Program

ABSTRACT

Kate Gleason College of Engineering
Rochester Institute of Technology

Degree: Doctor of Philosophy **Program**: Engineering
Author: Olivia V. Scheibel **Advisor**: Dr. Michael G. Schrlau
Dissertation Title: Nanoscale Carbon-Based Electrochemical and Temperature Sensors

Nanoscale sensors are required to study the interesting and complex physical, chemical, and biological phenomenon which occurs in microdomains. Carbon-based nanostructures (CNS) have been utilized in nanosensors with applications in many fields due to their versatility and unique properties. Several manufacturing processes can be used to produce CNSs though they often are expensive and require time-consuming purification and micro-assembly processes to integrate them into larger structures.

Here, novel silica-based structures are explored as unique templates on which to form CNSs that are easily integrated into sensors which can directly interface with standard laboratory equipment. The high electrical conductivity of CNSs enables the structures to be modified through an electrodeposition process to produce a chemical and a physical sensor. Specifically, this work describes the design, fabrication, and characterization of a nanoscopic thermocouple and electrochemical sensor. The thermocouple developed through this research uses a novel manufacturing method and set of materials to overcome the reduction in thermoelectric performance associated with small sensor sizes. The electrochemical sensor presented in this work overcomes challenges associated with other nanoscale sensors by allowing a working and reference electrode to be located within 50 nm of each other, minimizing the overall sensor footprint.

This work presents a novel and efficient method of preparing unique carbon-based sensors.

Acknowledgements

This dissertation is the culmination of the efforts of many people who have influenced me personally and academically over the years. Firstly, I must thank Dr. Schrlau for providing me the opportunity to conduct both undergraduate and graduate level research in the NBIL. Your continued guidance and support have been invaluable to my growth as an engineer.

My sincere thanks go to the members of my committee who generously gave their time and expertise to strengthen my research. I would like to thank the many professors and students who attended my Lab Talk presentations over the years, particularly Dr. Schertzer for his continued questions, comments, and suggestions. I thank Mr. Richard Hailstone and the NanoImaging Laboratory for his guidance and support on using the SEM. I am appreciative of the time, guidance and resources provided by Dr. Leslie Kate Wright regarding cell culture. Additionally, I would like to acknowledge Dr. Edward Hensel for his support and guidance throughout my doctoral studies. I would also like to thank Mr. William Finch and Jan Manetti for all their help and patience over many years.

I am grateful to Dr. Peter Lamberg for his insight, guidance, and useful discussion on electrochemical experimentation techniques. My gratitude is extended to David Lanza for his work towards the fabrication of diatom-based carbon structures. Thank you to my present and former RIT colleagues particularly Göker Türkakar, Indranil Joshi, Munther Alsudais, Atrisa Samadi, Collin Burkhart, and Cassie Robinson for their friendship and encouragement.

This work was completed with the support of my family, Kenneth, Sandra, Dieter, and Bailey, to whom I am immeasurably grateful. Thank you for making learning a joyful

experience and helping me build the foundation on which I could pursue higher education.

Above all, I thank my husband Mustafa Koz for his unending love, support, and guidance. Thank you for always believing in me and for being more excited about my research than I was at times. You have helped me grow into a better engineer, researcher, and person.

Finally, I gratefully acknowledge the funding provided by grants from the National Science Foundation (NSF Advance 1209115 and NSF CBET 1604893) and the Rochester Institute of Technology Engineering and Mechanical Engineering Departments.

Table of Contents

List of Figures

List of Tables

Nomenclature

Term	**Description**
Re	Reynolds Number
μ	Dynamic viscosity
A	Surface area
C	concentration
c_p	Specific heat
D	Pipe Diameter, Diffusion coefficient
d	Film thickness
e	Electron charge
E	Electron energy, potential
$E^{0'}$	Formal potential
F	Faraday's constant
h_{conv}	Convective heat transfer coefficient
i	Current
i_d	Diffusion limited current
I_p	Plasma current
k	Boltzmann constant
K	Vapor deposition constant
K_0	Heterogeneous electron transfer rate constant
K_m	Michaelis−Menten constant
m	mass

M	Molar mass
n	Number of electrons
Pr	Prandtl number
Q	Electric charge
R	Molar gas constant
r	radius
S	Seebeck coefficient
T	Temperature
t	Time
V	Electric potential
V_{avg}	Average fluid velocity
V_e	Volume of evaporated droplet
V_{emf}	Voltage generated by *emf*
V_j	Volume of the thermocouple junction
V_o	Volume of original droplet
$V_{p\text{-}p}$	Peak to peak magnitude of electric noise and ripple
V_{rms}	RMS of noise and ripple of electric potential
$x_{fd,\mathrm{t}}$	Thermal entrance length
Z	Ioffe criteria
z	Number of valence ions
α	Thermoelectric power, charge transfer coefficient
ζ	Fermi energy
κ	Thermal conductivity

λ	Mean free path of conduction
ρ	mass density, electrical resistivity
τ_J	Time constant of thermocouple junction

Abbreviations

AFM	Atomic force microscopy
CVD	Chemical vapor deposition
CNF	Carbon nanofiber
CNP	Carbon nanopipe
CNS	Carbon nanostructure
CNT	Carbon nanotube
emf	Electromotive force
HF	Hydrofluoric acid
PAP	*Para*-aminophenol
PAPG	p-aminophenyl galactopyranoside
SPM	Scanning probe microscopy
XPS	X-ray photoelectron spectroscopy
β-gal	β-galactosidase

Chapter 1

1. INTRODUCTION

Microenvironments, defined as domains with at least one dimension of less than 1 mm, have relevance in many fields including cellular and subcellular biology, “green” chemistry, microelectomechanical devices, turbulent flows and boiling, and interfacial phenomena, among others [1–4]. Macroscale sensors are prohibitively large for investigating these small domains. Even microscale sensors, with dimensions of the same length scale as microenvironments, can disrupt the physical processes that are being interrogated. Thus, the need for sensors approaching or at the nanoscale arises.

The development of nanosensors is a critical step in understanding many physical and biological processes [3,4]. To create technologies capable of interrogating microscopic domains and elucidating useful information, this work focuses on the synthesis of carbon-based nanostructures (CNS) and their modification to enable them to function as sensors. Nanoscale sensors are typically categorized as either biological, physical, or chemical depending on the property they quantify [5]. In this work, a physical sensor and a chemical sensor was developed. More specifically, an thermal sensor and electrochemical sensor were designed, fabricated, and characterized to demonstrate their utility. The aim of this work was to develop nanodevices capable of elucidating electrochemical and thermal data within microenvironments.

CNSs have made significant impacts as nanoscale sensors because of their versatility and unique properties [6]. CNSs are suitable for a range of sensing applications due to their nanoscopic size, high aspect ratio, high surface-to-volume ratio, electrical conductivity, and mechanical robustness [7]. For example, the electrical conductivity, and high surface-to-volume ratio of CNSs has made them an attractive candidate for electrochemical sensing applications with improved resolution and sensitivity relative to traditional electrodes [8,9]. The nanoscopic size, hollow geometry, and mechanical robustness has allowed CNSs to be used in fluid flow and phase change studies and intracellular delivery and sensing [10,11]. While CNSs offer useful properties for a variety of applications, they can be difficult to produce and integrate into sensors and devices [12–14].

This work focuses on the low-cost synthesis of unique CNSs which are directly integrated into macroscale devices to reduce the complexity of forming CNS-based sensors. These integrated CNSs are then modified to develop two novel carbon-based sensors with the potential to become widely accessible tools for the electrochemical and thermal characterization of microenvironments.

1.1. AIMS AND OBJECTIVES

Low cost and efficient manufacturing methods must be developed to facilitate the widespread use of ultramicro and nanosensors. This work achieves this through three objectives.

OBJECTIVE 1: Synthesize carbon micro and nanostructures

OBJECTIVE 2: Develop an ultramicro thermocouple

OBJECTIVE 3: Develop an electrochemical nanosensor

1.2. CARBON-BASED NANOSTRUCTURES

Carbon nanostructures is an all-encompassing term for a variety of carbon-based forms with nanoscopic dimensions including carbon nanofibers (CNF), nanotubes (CNT), and amorphous nanopipes (CNP) [6]. CNFs are conventionally defined as solid fiber-like carbon structures with at least one dimension of 100 nm or less while CNTs are defined as hollow tube-like carbon structures with at least one dimension of 100 nm or less [15,16]. Amorphous CNPs encompass those nanoscale carbon structures with a hollow tube-like structure but without the highly ordered, crystalline structure associated with CNTs [17]. This variation in CNSs is significant as it results in structures with varying physical properties.

1.2.1. Fabrication

Many fabrication methods have been developed to produce carbon structures of varying geometries and scales. Electric arc discharge, laser ablation, and chemical vapor deposition (CVD) are useful methods of producing CNSs [18–21]. Arc discharge, defined as the electrical breakdown of a gas, was the first method used to produce CNTs [22]. In this method, a direct current (DC) voltage is applied across two electrodes in an inert gaseous environment [23]. Typically, the anode contains a powdered carbon precursor and catalyst and the cathode is a pure graphite rod. As the voltage is applied, the gap between the electrodes is reduced and maintained at approximately 1 – 2 mm with the spacing constantly adjusted to maintain a constant arc. The current generates a 3000 to 4000 °C plasma which sublimes the powdered carbon precursor in the anode to form a carbon vapor which agglomerates at the graphitic cathode as it cools due to the large temperature gradient between the two electrodes. The process lasts for several minutes before the system is allowed to cool. While the agglomerate on the cathode as well as the soot on the chamber walls contains the CNTs additional purification steps are required as the collected materials contain large amounts of amorphous carbon metal particles, and CNTs with an undesirable number of walls. Current industrial purification methods rely on oxidation and acid-refluxing [24].

In the laser ablation method, a pulsed laser vaporizes a graphitic target to produce CNTs [24]. A block of graphite and catalyst is heated inside a quartz tube at approximately 1200 °C in an inert environment [19]. A high-power laser vaporizes the graphite target which is carried by the argon into a cooled collector located downstream. The vapor self-assembles into CNTs which condense onto the collector. The laser ablation process results in CNTs with higher purities than those produced via arc discharge and a diameter determine by the reaction temperature [24,25]. However, this method is more costly than the arc-discharge method and can result in branched CNTs that are not uniformly straight which can be undesirable for some applications [25].

High quality single and multi-walled CNTs can be achieved using electric arc discharge and laser ablation but can require expensive processes and complex purification and filtration steps to remove unwanted carbon particles and other byproducts of the process [24,25]. Chemical vapor deposition methods are employed to produce larger quantities of carbon nanostructures [26]. Typically, a metal catalyst is used in a high-temperature processing furnace to facilitate the decomposition of a hydrocarbon gas, resulting in carbon tubes and fibers with uniform diameters dictated by the diameter of the catalyst particle, as shown in Figure 1-1 A. It is possible to achieve aligned arrays of carbon nanostructures by prefabricating the catalyst particles into patterned arrays although this creates additional processing requirements increasing both the time and cost of the synthesis [27]. The CVD process can be coupled with a porous substrate to form amorphous CNPs in a process known as template-based CVD, as depicted in Figure 1-1 B [11,28,29]. Template-based CVD enables the fabrication of CNSs in a variety of dimensions, geometries, and shapes. Perhaps the greatest advantage of template-based CVD is that it enables the production of CNSs that are aligned and directly integrated into larger structures and therefore do not require additional manufacturing processes to maneuver or position. The simple manufacturing process results in one of the lowest-cost methods of producing CNSs. In this work, template-based CVD is explored as a method to produce integrated CNSs in a variety of geometries, length-sales, and aspect ratios.

1.2.2. Electrical Properties

While carbon-based nanostructures are renowned for their unique mechanical, electrical, thermal, and optical properties, this work relies mostly on the good electrical conductivity of CNSs [28,30]. The first objective of this work involves manufacturing integrated CNSs. The second and third objectives are focused on how those CNSs can be transformed into useful structures. The electrodeposition of materials onto the carbon film enables the devices to function as thermal and electrochemical sensors. As electrodeposition is used, it is critical that the nanostructures be electrically conductive so that a current can be applied.

Carbon nanotubes are excellent electrical conductors and, depending on the type, can exhibit metallic or semiconducting behavior [30]. In 1996, Ebbesen *et al.* investigated the electrical conductivity of CNTs formed via the carbon-arc method. For eight samples, the electrical resistivity varied orders of magnitude from $5.1 \times 10^{-6} – 0.8$ Ω·cm at room temperature [31]. This variation is likely due to the presence of impurities and variance from strictly one-dimension electron transport [32].

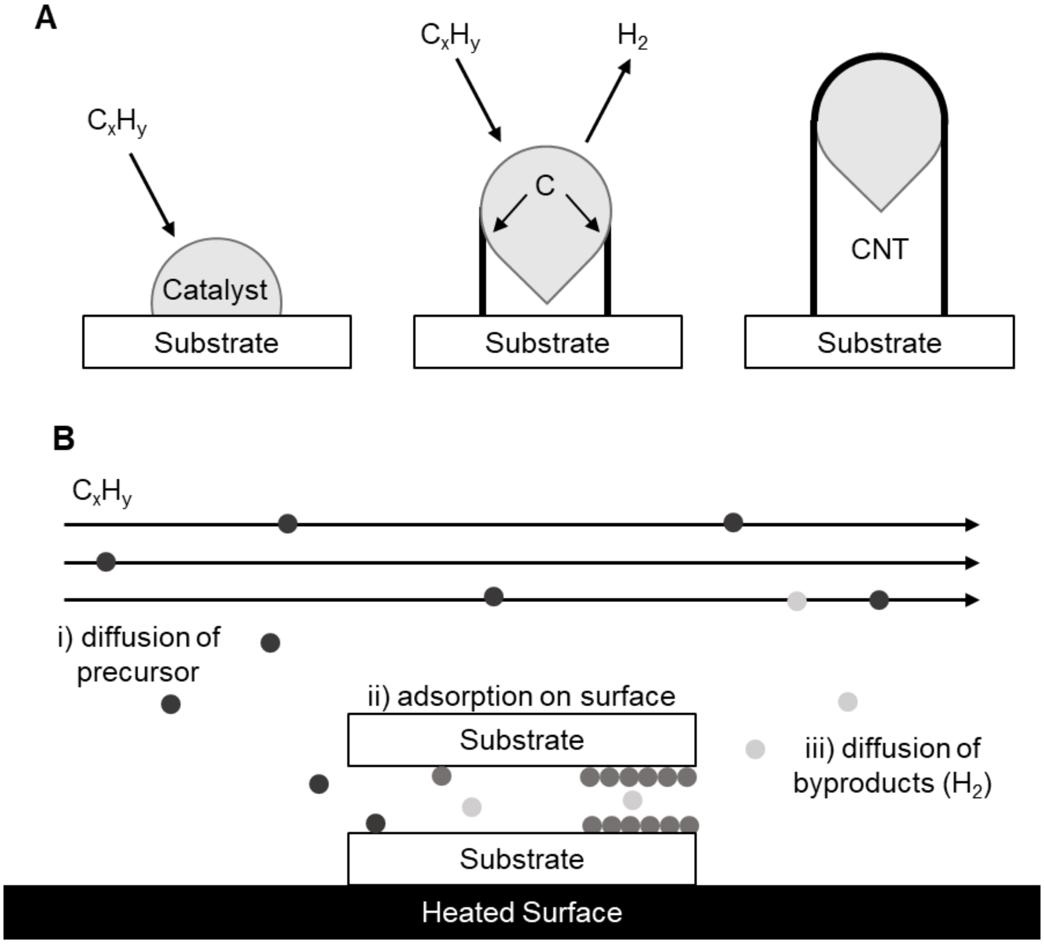

Figure 1-1: Formation of CNSs using chemical vapor deposition
A) Schematic of CNTs formed via chemical vapor deposition using a catalyst. B) Schematic of amorphous carbon CNPs formed via template-based chemical vapor deposition.

Several sources have investigated the electrical resistivity of thin-film amorphous carbon. In 1914, Stransfield reported the resistivity of amorphous carbon as 1.60×10^{-3} Ω·cm at ambient temperature [33]. More recently, Schrlau *et al*. reported the resistivity of

CNSs formed via template-based CVD as $1.07 \times 10^{-3}\ \Omega\cdot\text{cm}$ [34]. Although these values are less than those of some of the most conductive CNTs, amorphous CNSs are still electrically conductive and therefor amenable to the electrodeposition process crucial for this work. Further, amorphous CNSs maintain this good electrical conductivity while relying on a simpler and less costly fabrication process than CNTs and can be more easily integrated into a variety of sensors when produced with template-based methods [6].

Table 1-1: Electrical resistivity of common carbon nanostructures

CNS Type	Electrical Resistance [$\Omega\cdot$cm]
CNT	$5.1 \times 10^{-6} – 0.8$ [31]
Thin-film Amorphous Carbon	1.07×10^{-3} - 1.60×10^{-3}

1.2.3. Manufacturing Devices from Carbon Nanostructures

Carbon-based sensors can be manufactured in many configurations based on the application requirements. Some configurations which have been explored include electrodes with randomly dispersed CNTs on their surfaces. This configuration can include conductive CNT films and CNT-coated electrodes. CNT films and composites are well suited for macro- and microscale sensing platforms including electronic smart wearable yarns and fabrics and lab-on-chip devices [35,36]. Many groups have integrated CNTs onto electrodes with tips ranging from hundreds of nanometers to micrometers to improve their sensitivity. For example, Chen *et al*. coated CNTs onto flame-etched carbon fiber nanoelectrodes with tips ranging from 100 – 300 nm enabling the detection of nM concentrations of analyte [9].

Vertically aligned CNTs and CNFs have been integrated into sensing devices. The array of CNSs provide multiple detection sites and improve the signal-to-noise ratios and temporal resolution relative to conventional flat electrodes [37]. Vertically aligned arrays of CNSs have been used for micro and nanofluidic applications including delivery of biologically relevant cargo into plated cells [11,38]. Carbon-based electrodes consisting of dense arrays of vertically aligned CNPs have been produced from sputtered iron catalysts on silicon wafers [39]. These three-dimensional electrodes exhibited an increased electroactive surface area and thereby provided enhanced sensitivity.

In contrast to CNS arrays, devices with single or multiple CNSs integrated into their tips have been used for the highly localized interrogation of small domains. The nanoscopic tip provides high spatial resolution coupled with easy handling and positioning due to the integration to a micro or even macroscopic structure. CNS Nanostructure-tipped devices are frequently used in scanning probe microscopy (SPM), nanoscale electrochemistry, and cellular and intracellular studies.

1.2.4. Carbon Nanostructure-Tipped Devices

Atomic force microscope (AFM) cantilevers have been modified with single CNTs to improve imaging resolution and enable intracellular delivery [40–42]. This was first achieved in 1996 by Dai *et al*. CNTs were prepared using the direct-current carbon arc method. A 1 – 2 µm section of a traditional silicon AFM tip was coated with an acrylic adhesive. This adhesive-coated tip was brought into contact with a bundle of 5 – 10 CNTs under view of an optical microscope. Once the bundle was attached, the AFM tip was lifted, and the nanotube bundle was detached from its connection with other nanotubes, resulting in an approximately 6 μm long CNT bundle tip with a single CNT extending for the final 250 nm.

Aligned bundles of CNTs have been adhered to the tips of thin wires using contact assembly methods to form electrochemical sensors [43]. CNTs were grown using a CVD process with an iron catalyst to produce aligned forests of tubes. The tip of a thin platinum wire was coated with silver epoxy and brought into contact with one of the CNT forests using an optical stereo microscope and a translation stage. The CNTs were prepared several mm in length to simplify the process of attaching them to the wire however bundles with this length proved to be very fragile and were disrupted even by small air currents. The authors reduced the length of the bundles after attachment to the platinum wire via a 10 – 15 V dc voltage applied between the CNT bundle and another wire. By positioning the wire close to the bundle, an arc was formed which led to the bundle being controllably cut off near its tip.

Due to the hydrophobic nature of CNTs, the CNT electrode Dai *et* al. reported difficulty overcoming the surface tension of an aqueous droplet. The electrodes which could enter the droplet were reported to bend significantly in the fluid. The authors noted that the creation of a short and stiff bundle would overcome this obstacle however that could not be achieved with this manufacturing method which resulted in bundles of over 1 mm in length. Instead, the authors applied a platinum coating to the CNT bundle via electrodeposition to overcome the hydrophobic nature of the electrode.

Similarly, other works have reported nanoelectrodes fabricated by attaching bundles of CNTs to existing tungsten microelectrodes via an AC electric field and using a magnetic force to attach bundles of CNTs to the tips of glass micropipettes [44,45].

Glass micropipettes have been further explored as a template for forming CNPs by using chemical vapor deposition to deposit a thin carbon film onto surfaces of the pipette. Template-based manufacturing has been employed to form CNPs since the 1990s however it was difficult to integrate these structures into devices [46]. In 2005, Kim *et al*. described a novel technique of forming integrated CNPs by using pulled aluminosilicate glass capillaries as templates [14]. These glass micropipettes were placed in an inert environment and heat to 670 °C and exposed to a 30% ethylene/ 70% helium feedstock for 0.5, 6 or 16 hours. The pyrolytic decomposition of ethylene lead to the deposition of a thin carbon film on all surfaces of the pipette. The carbon on the outer surface of the template was removed via plasma oxidation. The tip of the micropipette was submerged in hydrofluoric acid to selectively remove the glass and expose the CNP. This method is generally regarding as more efficient that adhering single of bundles of CNTs to larger structures as it is a scalable process which produces an aligned CNP directly integrated into a macroscale handle without any tedious nanoassembly processes.

This method was refined so that the carbon film was preferentially deposited on the micropipette lumen with the assistance of a catalyst [34]. Quartz capillaries were filled with ferric nitrate dissolved in isopropyl alcohol and allowed to air dry. The capillaries were drawn into micropipettes, as above, and used as templates in a CVD process. In this work, the micropipettes were heated to 900 °C and methane was used as the carbon feedstock. The CVD process was operated at parameters that enabled the pyrolytic decomposition of methane only in those regions with catalyst. As a result, carbon was not deposited on the exterior surface of the micropipette and the plasma oxidation step required in the previous work was not needed. Again, buffered hydrofluoric acid was used as a wet etchant to selectively expose the carbon at the tip of the micropipette. This resulted in an integrated CNPs with diameters of 10 s to 100 s of nanometers, depending on the parameters used to form the quartz template. These CNPs were used to spear oral squamous carcinoma cells and deliver fluorescent dye into the cytoplasm of the cell.

1.3. STRUCTURE OF THESIS

Chapter 1: Introduction – An overview of CNSs and ultramicro- and nanoscale sensors is discussed in this section.

Chapter 2: Synthesis of Carbon Micro- and Nanostructures - A low-cost, high-throughput CVD process was utilized to deposit carbon within novel silica-based templates. This simple template-based manufacturing process allows the carbon devices to be integrated into millimeter scale silica-based templates without micro- or nanoassembly. This helps reduce the time and resource requirements typically associated with integrating CNSs into sensors. This work explores a wide variety of templates and serves as the foundation for the sensors developed in Chapters 3 and 4. The manufacturing process facilitates the integration of CNSs into standard laboratory equipment, promoting broad utilization in a variety of applications.

Chapter 3: Design and Fabrication of a Nanoscopic Thermocouple - The process of modifying a CNP to enable it to serve as a thermocouple is detailed. This nanoscale thermocouple is directly integrated into a glass pipette providing ease-of-handling. Micro and nanoscale thermocouples have found use in applications including the characterization of the boiling process in microchannels, the surface temperature of plasmonic devices, temperature changes in cells, and the temperature profile in fuel cells and combustion processes [4]. Micropipette-based thermocouples are an area of interest as the provide a simple, low-cost method of preparing sensors. The thermocouple described in this work exhibits enhanced spatial resolution and sensitivity compared to micropipette-based thermocouples currently available in the literature.

Chapter 4: Design and Fabrication of an Electrochemical Nanosensor - The development, fabrication, and characterization of a novel self-contained, two-electrode nanosensor contained within the tip of a needle-like probe is described. Such small domains have significance in biological research, portable devices or in the pursuit of “green” analytical chemistry which aims to minimize the economic and ecological costs of research by reducing the quantity of expensive reagents required and waste produced [3,47]. Due to the low-cost manufacturing process, this nanoprobe has the potential to become a unique and widely accessible tool for the electrochemical characterization of microenvironments.

Chapter 5: Contributions and Future Directions - The outcomes and key contributions of this work are summarized in this section. In addition, several possible future directions are described.

Chapter 2

2. SYNTHESIS OF CARBON MICRO- AND NANOSTRUCTURES

A low-cost, high-throughput CVD process was utilized to deposit carbon within novel silica-based templates. This simple template-based manufacturing process, described in Figure 2-1, allows the carbon devices to be integrated into millimeter scale silica-based templates without micro- or nanoassembly, facilitating commercialization. Briefly, silica-based templates are prepared, carbon is deposited on the templates via a CVD process, and finally the template is selectively removed using wet-etchants to expose the CNSs. The carbon-based devices were designed to readily integrate into standard laboratory equipment, promoting broad utilization. Herein, a repeatable methodology for fabricating multifunctional, carbon-based micro- and nanofluidic devices as well as establishing relationships between parameters at each stage of fabrication and the final geometry, including diameter and wall thickness of the carbon structures, of the device is presented.

2.1. BACKGROUND

2.1.1. Template-Based Manufacturing and Chemical Vapor Deposition

Template-based chemical vapor deposition was developed as an extension of catalyst-based CVD processes. Porous substrates including alumina oxide membranes and glass capillaries are employed often, but not necessarily, along with a catalyst to promote and control carbon deposition. Again, a hydrocarbon gas is introduced to a high-temperature furnace where it is deposited onto the surface of the template. After the CVD process, the substrate is selectively removed to produce aligned arrays, individual nanostructures, or single integrated nanostructures, depending on the choice of template [11,14,34,48,49]. Template-based CVD allows the geometry, size, and arrangement of the carbon structures to be controlled by the template selection and the thickness of the carbon layer to be controlled by the process parameters used during the carbon deposition process. It should be noted however, that unlike in the aforementioned fabrication methods, carbon structures fabricated via the template-based CVD method are in the form of amorphous carbon and thus have different physical and mechanical properties.

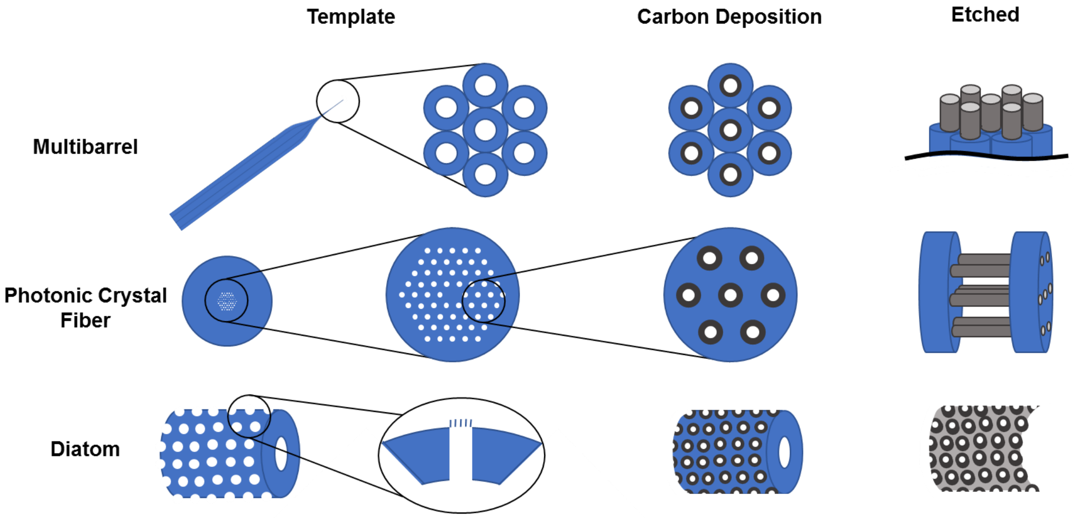

Figure 2-1: Template-based fabrication of aligned CNSs
Three-step manufacturing process utilized to deposit and expose carbon on various templates. Please note that schematic is not to scale.

Many hydrocarbon source gases have been utilized in CVD process to produce amorphous carbom structures. Ethylene, pyrene, acetylene, butane, and methane have been demonstrated to be sucessful precourser options [11,29,49–52]. Both experimental and numerical methods have been used to establish that the deposition rate is dependent on hydrogen:carbon (H:C) ratio of the source gas [53,54]. Specifically, it has been determined that as the source H:C ratio increases, the deposition rate of carbon decreases exponentially. Methane was used as a carbon source in this work as it has a higher H:C ratio than some of the other available carbon source gases which provides additional control over the carbon deposition. Further, methane has been previously used in combination with quartz pipettes [29].

2.1.2. Glass Micropipettes

Pulled glass micropipettes provide an electrically insulating template for which to manufacture an array of tools. Although glass needles have been employed for centuries, Barber was the first to produce glass capillary micropipettes with tips fine enough to capture a single bacterium by heating capillary tubing over a burner and drawing the softened glass using forceps [55,56]. Taylor and Whitaker developed a fine-tipped cellular probe consisting of a platinum/platinum black electrode housed within an electrolyte-filled glass micropipette [57]. This probe was capable of measuring membrane potential and protoplasm pH of individual algae while maintaining cell viability. Graham et al. and later Ling developed 2 - 5 µm and sub-micrometer electrolyte-filled glass micropipettes, respectively, and utilized them to study the membrane potential of muscle fibers [58–60].

Enhanced control over tip geometry including diameter, taper, and length was provided as glass micropipette manufacturing methods advanced from hand-drawn to complex mechano-electrical pulling systems [61,62]. Although this advancement enabled the production of even finer-tipped electrodes better suited for cellular studies, it inadvertently led to challenges using the micropipettes as electrodes [63,64]. As the tip diameter decreased, increasing electrolyte concentrations were required to maintain a sufficient electrode resistance to measure the small electrical signals generated within individual cells [65]. These relatively high electrolyte concentrations can reduce cell viability if they leak into the cytoplasm. Further, the rigid tips can lead to organelle damage and are prone to breaking upon contacting a rigid surface.

By using quartz micropipettes as templates to produce integrated carbon nanopipes, we can exploit the beneficial features of the quartz structures, namely electrical insulation and rigid macroscale barrel, while avoiding the drawbacks associated with liquid electrolytes. By depositing and subsequently exposing a thin carbon layer within the micropipette, probes with fine, conductive, and flexible tips and insulated, rigid, and macroscale barrels can be produced and serve as the scaffold on which to produce unique small-scale sensors [34,66].

2.2. QUARTZ CAPILLARIES

Established template-based nanomanufacturing processes will be built upon to produce carbon-based nanoprobes suitable for potential applications including fluid transport, biomedical interfacing, and electrochemical and thermal sensors [34,67]. A low-cost, high-throughput CVD process is utilized to deposit carbon within novel silica-based templates. This simple template-based manufacturing process allows the carbon devices to be integrated into millimeter scale silica-based templates without nano-assembly, facilitating commercialization.

2.2.1. Template Selection and Formation

Fabrication of the electrochemical nanoprobes begins with the preparation of a silica-based template. Glass templates were selected because glass is an electrically resistive, biocompatible material. While any type of glass with a softening temperature above that required for carbon film deposition could serve as a template, quartz glass substrates were selected for use in this study as they have the highest softening temperature and resistivity of the available glass capillaries.

Three quartz capillaries were investigated in this work. Initially, single barrel capillaries (Sutter Instrument Co.) were investigated as they have the most basic geometry. Quartz Theta Capillaries (Sutter Instrument Co.) were selected as templates as they possess a geometry of two independent channels separated by a quartz septum. Finally, Multibarrel Quartz (Sutter Instrument Co.) capillaries consisting of seven fused quartz barrels each with an initial outer and inner diameter of 0.33 mm and 0.16 mm, respectively, were employed. A cross section of the Multibarrel Quartz capillaries is presented in Figure 2-1.

To form a nanoscale tip, it was required to “pull” the quartz capillaries, following the well-established methodology of drawing glass capillaries into micropipettes [62]. Due to the high softening temperature of quartz, a CO_2 laser-based micropipette puller (Sutter Instrument Co., P-2000F) was used to pull the capillaries into nanopipettes. Pulling parameters including heat, filament, delay, velocity, and pull strength enabled control over the micropipette tip size and geometry. The resulting pipettes had tips in the micro- to nanoscale, depending on the pulling parameters utilized during template formation. The pulling parameters used for each template are described in Table 2-1.

Table 2-1: Template formation parameters used to fabricate single barrel and theta quartz templates. Note that the values are unitless

Template	Line	Heat	Filament	Velocity	Delay	Pull
Single Barrel	1	700	4	55	130	55
	2	700	4	55	130	250
Theta	1	750	4	50	175	100
	2	750	4	60	135	175
Multibarrel	1	800	4	80	160	160

2.2.2. Carbon Deposition

The quartz micropipettes served as a template for a CVD process which, under controlled conditions, was capable of depositing carbon on the inner lumen of the pipette. As mentioned above, the shape of the template was determined by the parameters used during the pulling process ultimately providing control of the shape of the deposited carbon film.

The CVD process includes three phases: ramp-up, deposition, and cool-down, as shown in Figure 2-2. During the ramp-up phase the furnace is heated to the desired temperature under an argon environment to purge the system of oxygen. Once the desired temperature is reached, the deposition period begins by flowing a hydrocarbon gas through the heated furnace where it decomposes and deposits a carbon film on the template. The deposition phase is maintained until the desired film thickness is achieved at which point the flow of hydrocarbon gas is ceased and the furnace is allowed to cool under an argon flow to maintain the oxygen-free environment and thereby prevent oxidation of the carbon layer.

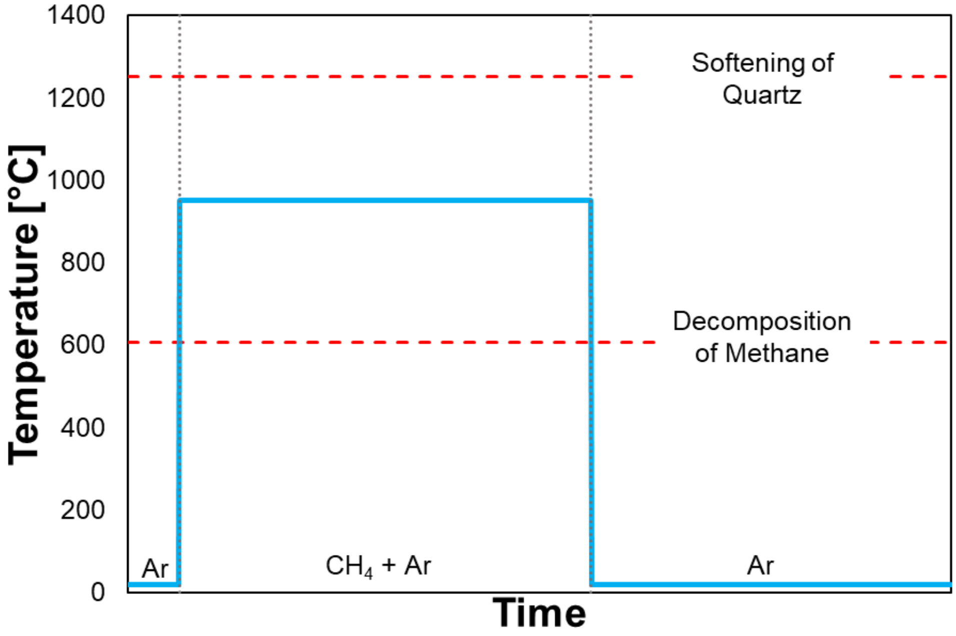

Figure 2-2: Chemical Vapor Deposition Process
Chemical vapor deposition (CVD) process parameters used to produce nanosensors by thermally decomposing a carbon-based vapor on the surface of quartz templates. The solid blue line indicates the temperature setting of the furnace while the red dashed lines indicate the temperature limits of the process imposed by the softening temperature of quartz and the thermal decomposition temperature of methane.

The CVD process was performed in a single stage, tube furnace (Thermo Scientific Lindberg Blue M Mini-Mite Tube Furnace, 30 cm heated length) at atmospheric pressure as illustrated in Figure 2-3. Methane and argon were utilized as carbon source and carrier gasses, respectively, as previously established [34]. The argon flow rate was regulated by a floating ball rotameter (Airgas Y21 B652). The methane flow rate was regulated by a mass flow controller (Aalborg GFC17). Samples were loaded into a quartz tube (inner tube diameter: 25mm, tube length: 60cm) located in the resistance heated furnace. Samples were positioned towards the middle of the tube to encourage full thermal development of the gas.

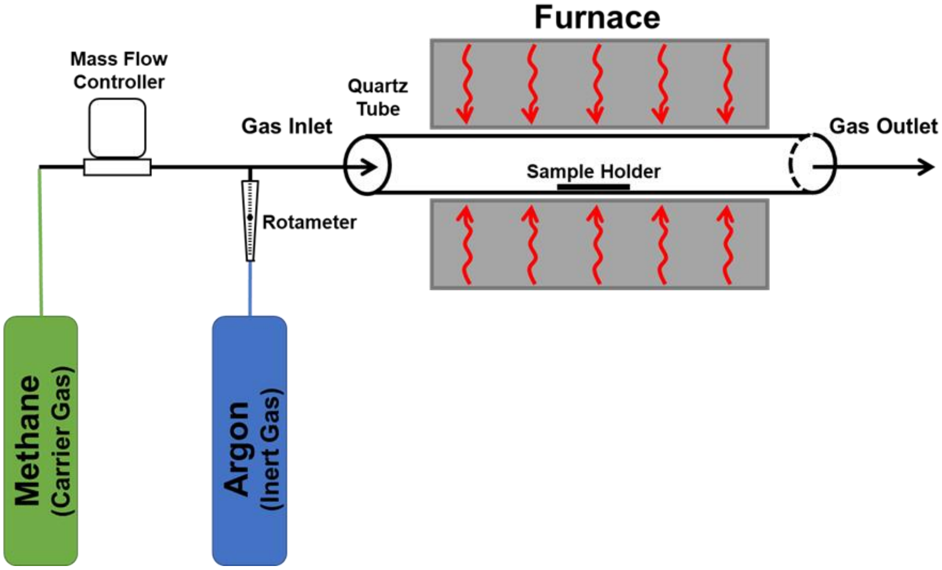

Figure 2-3: Schematic of CVD system.

To calculate the thermal entrance length ($x_{\mathrm{fd,t}}$), it is first necessary to determine whether the flow of interest is within the laminar or turbulent regime by calculating the Reynolds Number (Re). The Reynolds number, defined as the ratio of inertial to viscous forces within a fluid, is defined as follows for flow within a circular pipe.

$$\mathrm{Re} = \frac{\rho V_{\mathrm{avg}} D_p}{\mu} \qquad \text{2-1}$$

where ρ is the fluid density, V_{avg} is the average fluid velocity, D_p is the pipe diameter, and μ is the dynamic viscosity of the fluid. It should be noted that the CVD process relies on a mixture of argon and methane and thus special consideration must be taken when determining the Re of the flow. However, to simplify the analysis the combined flow will be considered to be comprised of a single component at the combined flow rate. The most extreme case will be utilized to demonstrate the highest possible thermal entrance length.

The properties used in the analysis, as seen in Table 2-2, are at atmospheric pressure and 950°C and the flow conditions were 165 sccm through a 25 mm diameter tube. For both the methane and argon cases, Re was found to be less than 2040 and thus can be considered laminar.

Table 2-2: Properties used to calculate the thermal entrance length of the CVD furnace. Properties are at atmospheric pressure and 950 °C

	Methane	Argon
Density [kg·m^{-3}]	0.246	0.614
Dynamic Viscosity [Pa·s]	2.33×10^{-5}	2.82×10^{-5}
Specific Heat [K·kg·K^{-1}]	435	520
Thermal Conductivity [W·m^{-1}·K^{-1}]	0.1290	0.09.36268
Reynolds Number	8.65	9.36
Prandtl Number	0.0786	0.5470
Thermal Entrance Length [mm]	0.85	6.4

For laminar flow in a pipe, the thermal entrance length ($x_{\mathrm{fd,t}}$) can be expressed as a function of the pipe diameter (*D*), and Prandtl number (*Pr*) [68].

$$x_{\mathrm{fd,t}} \approx 0.05DRePr \qquad 2\text{-}2$$

where *Pr* represents the ratio of momentum to thermal diffusivity and can be expressed as follows:

$$Pr = \frac{c_p\mu}{\kappa} \qquad 2\text{-}3$$

where c_p is specific heat, κ is thermal conductivity. Again, these properties are at atmospheric pressure and 950°C.

The most extreme thermal entrance length is 6.40 cm which is less than the location of the samples (15 cm from entrance) and thus the gas can be considered as fully thermally developed. As shown in Figure 2-4, this predicted thermal entrance length of 6.40 cm is consistent with the deposition of carbon visible on the tube furnace walls.

As described in Section 1.2.4, previous reports of carbon nanostructure-tipped devices have relied on the use of an iron-based catalyst to promote carbon deposition on the interior of the template. In this work, it was found that by adjusting the CVD process parameters, specifically the temperature and gas flow rates, the use of a catalyst could be avoided. While some carbon was deposited on the exterior of the pipette, this was minimal compared to the carbon deposited on the template lumen. This is likely due to an increased number of molecule-surface interactions in the confined region of the lumen resulting in a higher rate of carbon deposition [69]. By refining the process parameters (minimizing temperature and adjusting the ratio of argon to carbon source flow rate, seen in Figure 2-8) to promote deposition on the lumen and minimize deposition on the exterior the use of a catalyst was avoided which simplified the manufacturing process and reduced the manufacturing time by one day.

2.2.3. Template Removal

The CVD process resulted in silica-based structures with a carbon film along the entire length of the lumens. To remove the template and expose tubular structures of carbon, established microfabrication procedures were employed [70]. Hydrofluoric acid (HF), a wet etchant commonly used to remove silica-based materials, was employed to selectively etch the tip of the quartz templates to expose the carbon structures. The carbon structure appeared to remain unaffected by the HF etchant. Buffered hydrofluoric acid (BHF, 10:1) was employed to reduce the etch rate and thereby provide improved control over the length of exposed carbon.

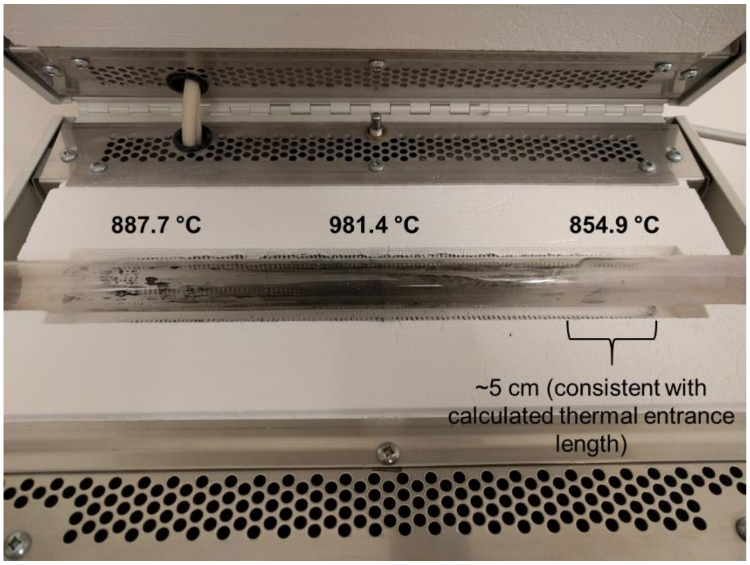

Figure 2-4: Quartz tube used in CVD process showing carbon deposition.

The thickness of the quartz template increases as the distance from the tip increases. When the tip of the pipette was dipped in a BHF bath, “layers” of quartz are removed, subsequently exposing additional lengths of carbon. This allows for the etching rate to be controlled by time, regardless of how far the tip is submerged in the BHF bath, as seen in Figure 2-5. With this method, large quantities of carbon tips could be etched simultaneously.

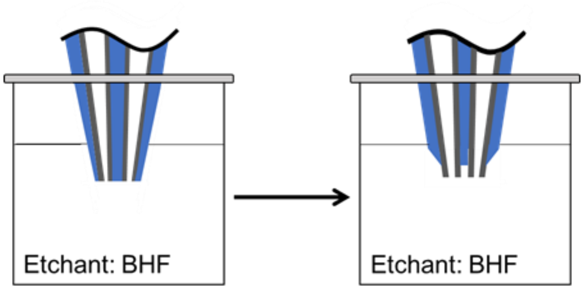

Figure 2-5: Schematic of the etching process.
Etching process used to selectively remove the quartz template from the tip of the nanoprobe. Time is used to control the length of exposed carbon as the quartz thins near the tip and is etched more rapidly.

2.2.4. Results and Discussion

Furnace Characterization

The temperature profile of the furnace was characterized parallel to the direction of the gas flow. As seen in Figure 2-6, it was found that there was a large variation in temperature along the central axis, but the temperature was consistent over time. Further, it took 90 minutes for the temperature to stabilize, as shown in Figure 2-7, but it was found that it was only necessary to wait 30 minutes from the start of the heating process until the introduction of the reactant gas.

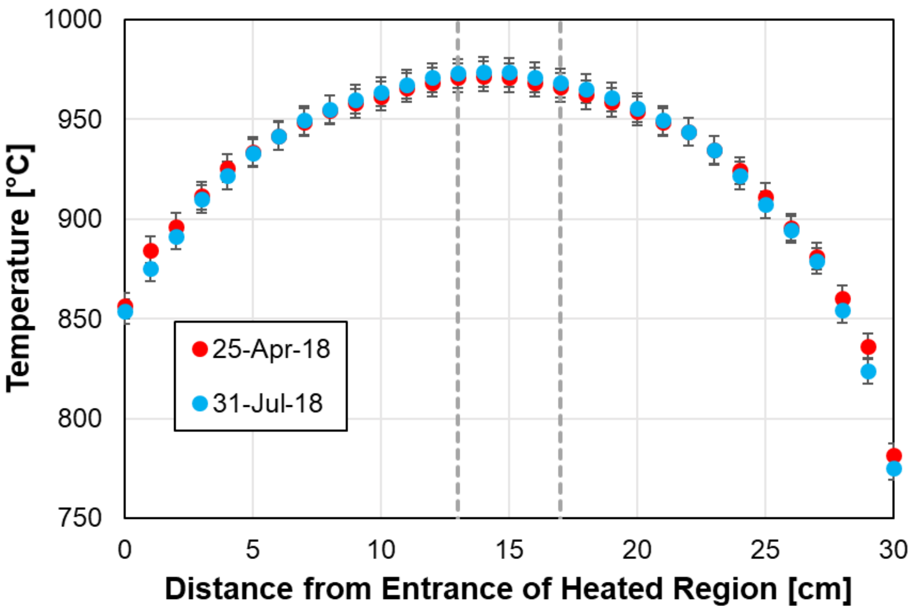

Figure 2-6: Thermal characterization of furnace tube.
Temperature profile along the central axis of the furnace tube under the influence of 1000 sccm Ar. Data from two different dates were recorded and found to be consistent. Grey dashed line represents region where the sample holder is located.

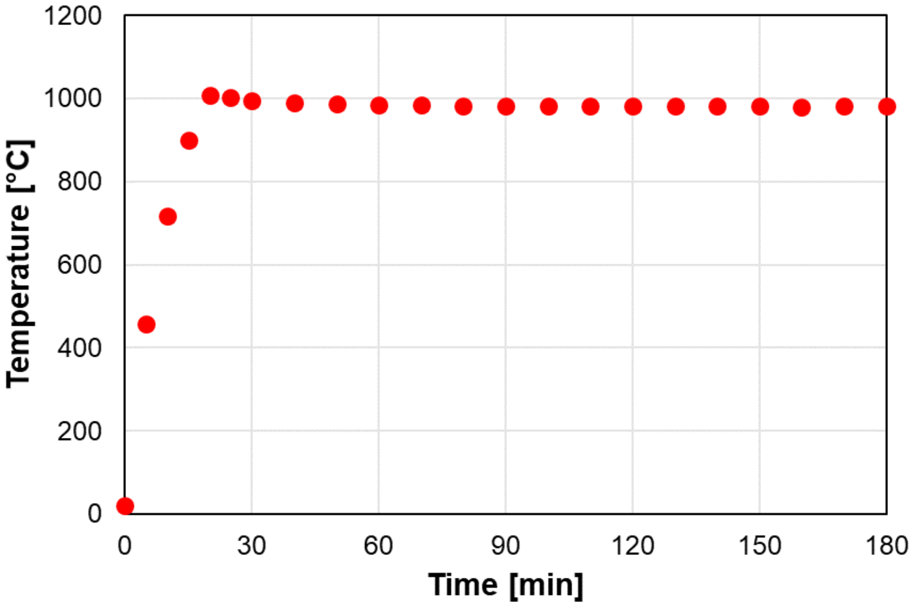

Figure 2-7: Time dependent temperature of the center of the furnace.

Table 2-3: Flow rates investigated for CVD process.

Scenario	Temperature [°C]	Ratio (Ar: CH_4)	Argon Flow Rate [sccm]	Methane Flow Rate [sccm]	Duration [h]
(1)	950	1:3	124	372	4
(2)	950	2:1	330	165	4
(3)	950	3:1	372	124	4

Figure 2-8: Effect of Ar:CH_4 ratio on carbon deposition.
Variation in qualitative carbon deposition as a function of Ar:CH_4 flow rate. The Ar:CH_4 flow rate ratios are defined as follows – 1) 1:3, 2) 2:1, 3) 3:1

Table 2-4: Carbon Deposition Parameters for Silica-Based Templates

Template	Temperature [°C]	Argon Flow Rate [sccm]	Methane Flow Rate [sccm]	Duration [h]
Single	950	330	165	4
Theta	950	330	165	4
Multibarrel	950	1000	165	4
Photonic Crystal Fiber	950	300	200	4

Single Barrel Pipettes

The manufacturing parameters that lead to consistent production of single-barrel pipettes were investigated. A previously-developed program was employed to form the quartz pipette templates, described in Table 2-1 [71].

Table 2-3 describes some of the argon to methane ratios investigated. As shown in Figure 2-8, a 2:1 ratio of argon to methane was found to deposit a sufficient amount of carbon while a 1:3 ratio led to an over-deposition on the template exterior and a 3:1 ratio resulted in insufficient carbon deposition on the lumen.

A half-cylinder quartz sample holder was used to constrain the quartz micropipettes during the CVD process as when the samples were placed directly into the tube furnace, variation in carbon deposition along the pipette axis was observed, as shown in Figure 2-9. The samples were placed directly on the bottom of the sample holder. Three different sample holders were investigated to determine which resulted in the best carbon deposition: 1) a half cylinder with one open end and one closed end positioned downstream, 2) a half cylinder with two closed ends, and 3) a half cylinder with on open end and one closed end positioned upstream. As seen in Figure 2-10, when the open end of the sample holder was positioned upstream, the carbon deposited near the tip of the micropipette was more opaque than scenario 1 or 2. A more opaque carbon deposition qualitatively indicates that more carbon was deposited on the template. As such, sample holder orientation 2 was used in subsequent CVD processes.

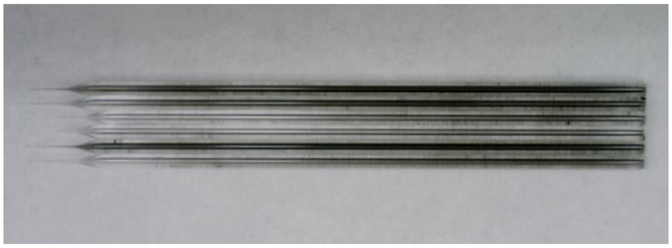

Figure 2-9: Carbon deposition when micropipettes were placed directly in tube furnace.

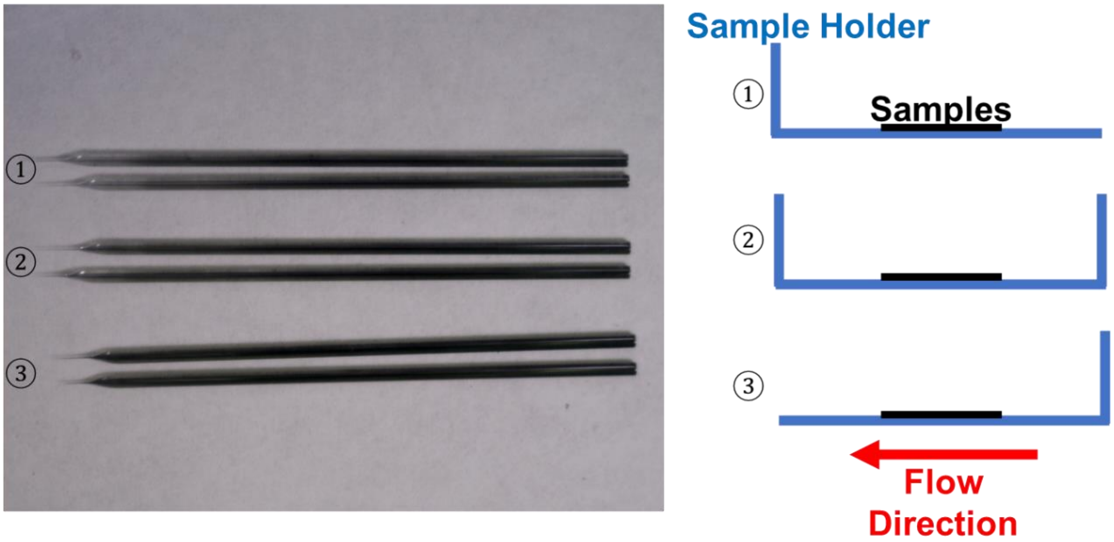

Figure 2-10: Effect of sample holder orientation on opacity of carbon film.

Chemical vapor deposition parameters presented in Table 2-4 were demonstrated to be capable of producing probes. The carbon-coated probes were etched in BHF for 3 minutes to expose approximately 2 μm of carbon at the tip, as seen in Figure 2-11. The average tip diameter and length with standard deviation are presented in Table 2-5.

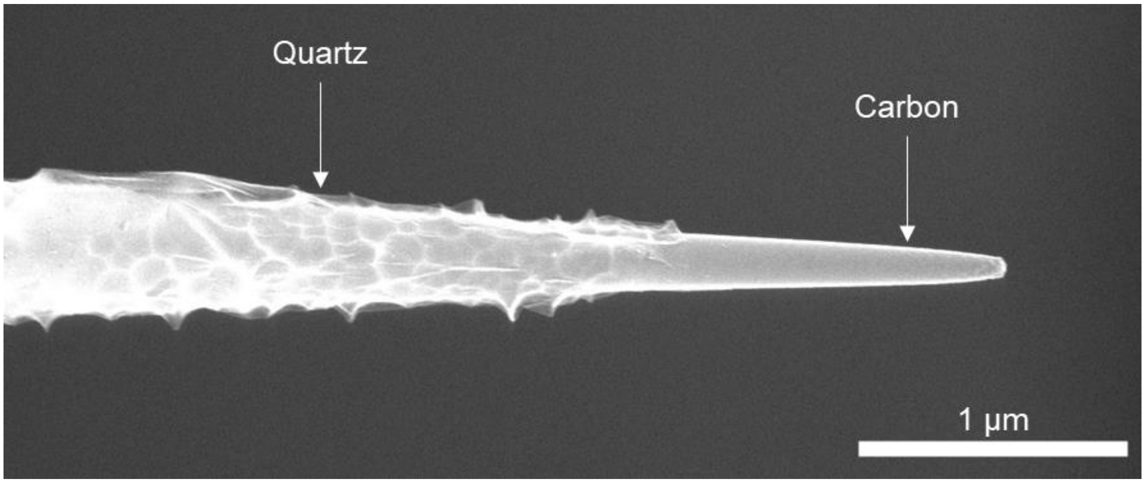

Figure 2-11: SEM micrograph of a single barrel pipette showing the carbon tip and partially etched quartz template

Table 2-5: Tip Diameter and Length for Pipettes

Template	Number of Samples	Tip Diameter [nm]	Etch Time [s]	Length [nm]	Pipe Width [nm]	Pipe Separation [nm]
Single	10	181 ± 101	180	2273 ± 1239	n/a	n/a
Theta	20	315 ± 100	30	194 ± 112	113 ± 50	43 ± 3
Multibarrel	7	222 ± 29	60	325 ± 162	58 ± 7	n/a

Theta Pipettes

A template-forming program was developed for producing double-barrel nanoprobes, described in Table 2-1. The program was designed such that it reduced the tip diameter of the probes as small as possible without closing the tip. This was confirmed by demonstrating that the probe was capable of ejecting filtered (20 nm pore size filter, Anotop 10 Plus, Whatman™) Allura Red and Brilliant Blue FCF dye from the tip of the pipette using an injection system (Eppendorf Femtojet) observed under an optical microscope (AxioObserver.A1m, Zeiss). As shown in Figure 2-12 A, each barrel was loaded with a unique dye color. When the system was pressurized, dye was ejected from both barrels as shown in Figure 2-12 B.

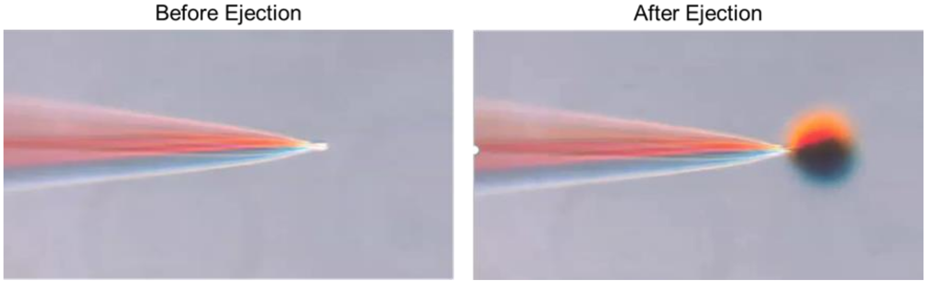

Figure 2-12: Before and after ejection of dye from the tip of a theta pipette into an aqueous environment.

It was found that alternative CVD parameters to those used for single-barrel probes were required and are described in Table 2-4. A micrograph of the resulting probe can be seen in Figure 2-13. The total tip size of the pipette and size of the individual carbon pipes is described in Figure 2-14 B and C. The width of the septum at the pipette tip, shown in Figure 2-14 D, indicates that this method was able to produce two carbon structures with a sub-50 nm spacing without the need of complicated nano-assembly procedures. The effect of etch time on the exposed length was investigated for etching times of 30, 60, 180, and 300 s. The slope of the resulting data was used to calculate the etch rate. As show in Figure 2-14 E, the etch rate was 3.5 nm · s^{-1}. An optical micrograph of a theta pipette etched for 300 s is shown in Figure 2-15.

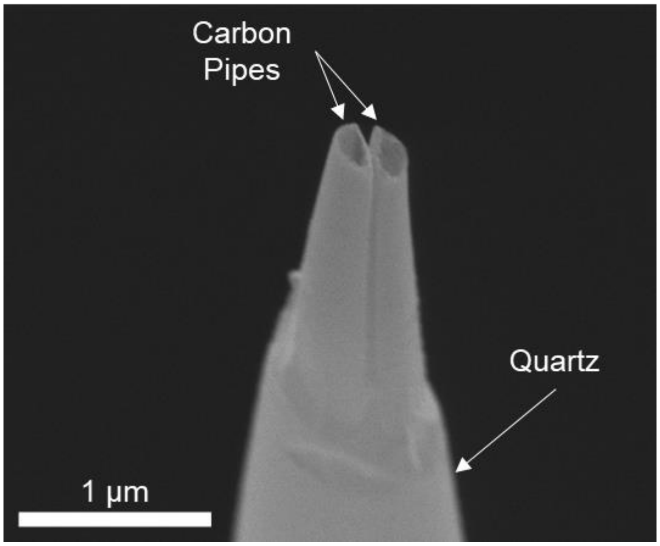

Figure 2-13: SEM micrograph of a theta pipette showing the two independent carbon pipes and partially etched quartz template.

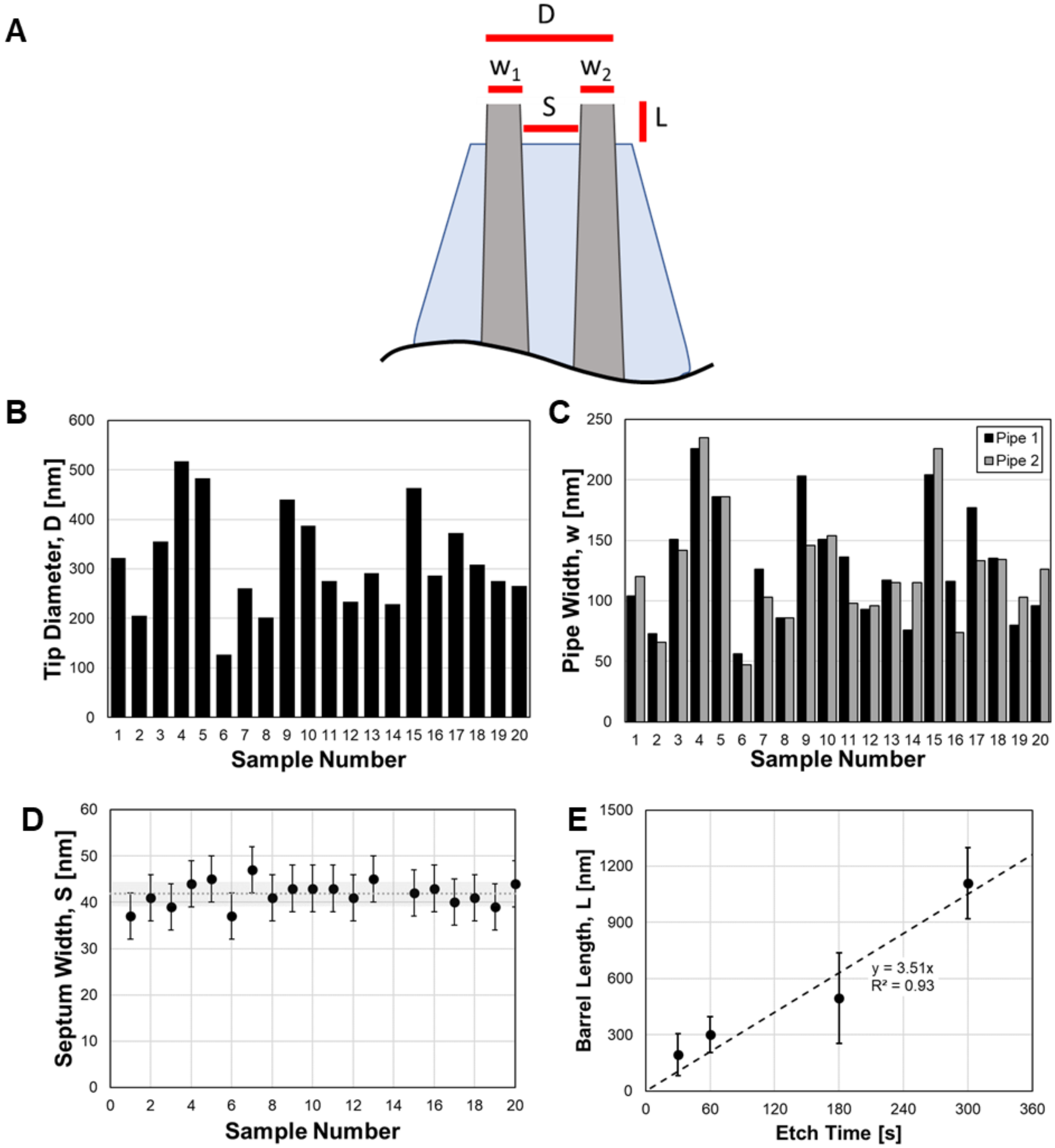

Figure 2-14: Characterization of theta dimensions.
A) Schematic of theta pipette. B) Overall tip diameter of theta. C) Individual pipe width. D) Spacing between the two independent carbon pipes. The grey dotted line indicates the average separation and the shaded grey area indicates two standard deviations. E) Average length of exposed carbon as a function of etch time. All measurements were collected to the nearest 5 nm. Data represents a sample size of 20 pipettes.

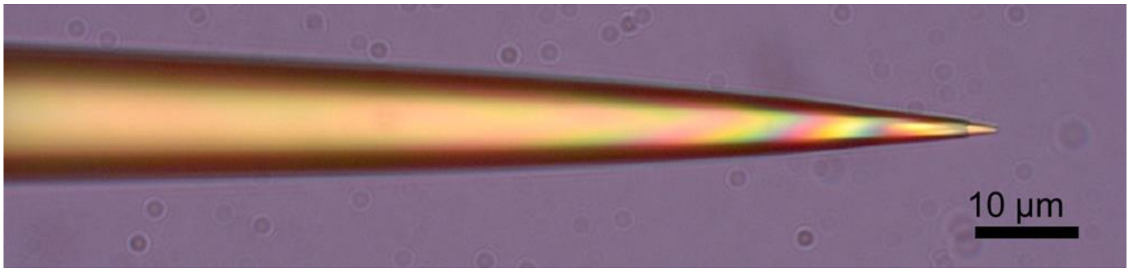

Figure 2-15: Optical micrograph of theta pipette etched for 300 s.

Multibarrel Pipettes

A third template-forming program was developed for drawing the Multibarrel Capillaries into pipettes, described in Table 2-1. The CVD parameters used to deposit carbon on the 7 lumens is described in Table 2-4.

Carbon nanopipes with average diameters of 58 nm were integrated into a total tip diameter of approximately 315 nm. An average exposed carbon length of 325 nm was produced by wet-etching for 1 min. The resulting integrated nanostructure can be seen in Figure 2-16. Typically, it was not possible to resolve all 7 tips as they would collapse onto each other and form bundles. This could be resolved by reducing the etch time to expose short segments of the carbon tips. Additionally, the carbon tips were not a uniform length. This variation is likely stemming from the template formation process and could be resolved by refining the parameters used when drawing the capillary into a micropipette.

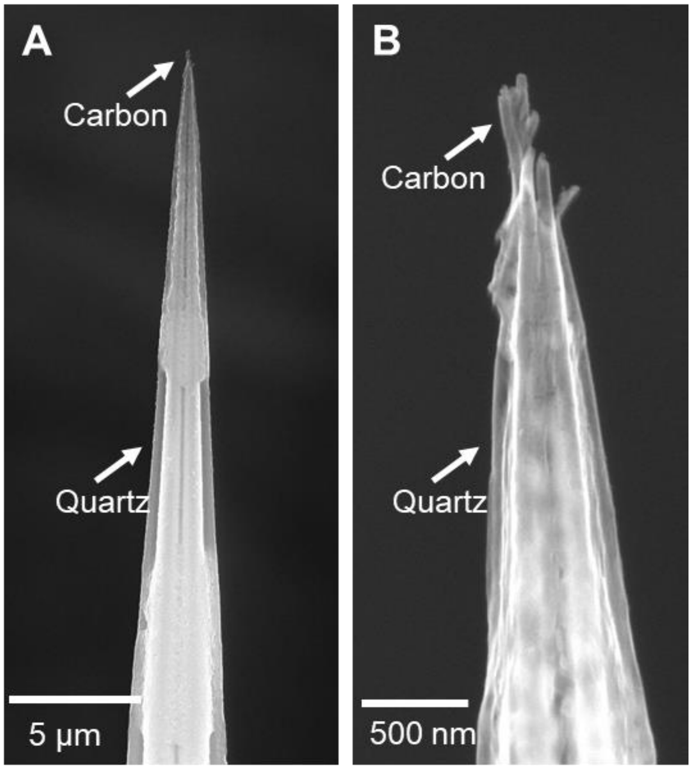

Figure 2-16: SEM micrograph of multibarrel pipette
A) Partially etched tip and B) individual carbon pipes

2.3. Photonic Crystal Fibers

The ESM Large-Mode-Area Photonic Crystal Fiber (Thorlabs, Inc.) contains 60, 1.25 µm diameter bores within a 125 µm diameter quartz fiber. A schematic of the cross section of this fiber is illustrated in Figure 2-1. Photonic Crystal Fibers are typically used as optical fibers however in this work they serve as a unique template for the production of high-aspect ratio carbon pipes.

2.3.1. Template Selection and Formation

Photonic crystal fibers were cut to lengths of approximately 25 mm to serve as templates. The protective acrylate casing was removed to expose the quartz fiber by briefly soaking the sample in acetone and then pulling the fiber out from the casing. As the photonic crystal fiber already has micro-scale bores, no additional template formation steps were required.

2.3.2. Carbon Deposition

The carbon deposition process for the photonic crystal fiber templates closely resembles that described above for multibarrel capillaries. The same furnace set-up was utilized for deposition; however, different deposition parameters were used to achieve a carbon film on each of the 60 lumens of the template. These parameters are detailed in Table 2-4.

2.3.3. Template Removal

To etch the photonic crystal fibers, both ends of the fiber were attached to an acrylic slide with epoxy. As both acrylic and epoxy are unaffected by BHF, they shielded those regions of template from being etched by the BHF while the exposed regions of template were etched. The photonic crystal fibers and acrylic slide were completely submerged in a BHF bath for 24 h to completely remove the exposed region of template, leaving only the 60 carbon microstructures attached to the remaining quartz template on both ends.

2.3.4. Results and Discussion

Carbon micropipes with uniform diameters of 1.25 µm and a wall thicknesses of 95 nm were produced utilizing the three-step manufacturing process. As seen in Figure 2-17 A and B, the carbon pipes were cut to enable visualization of the cross section. The length of the pipes can be controlled by varying the distance between the two fixation points for the etching process, described above, allowing for the fabrication of carbon structures with high aspect ratios as shown in Figure 2-17 C. Carbon pipes with further reduced diameters could be fabricated by employing a similar pulling process utilized to fabricate the multibarrel templates to further reduce the diameter of the template.

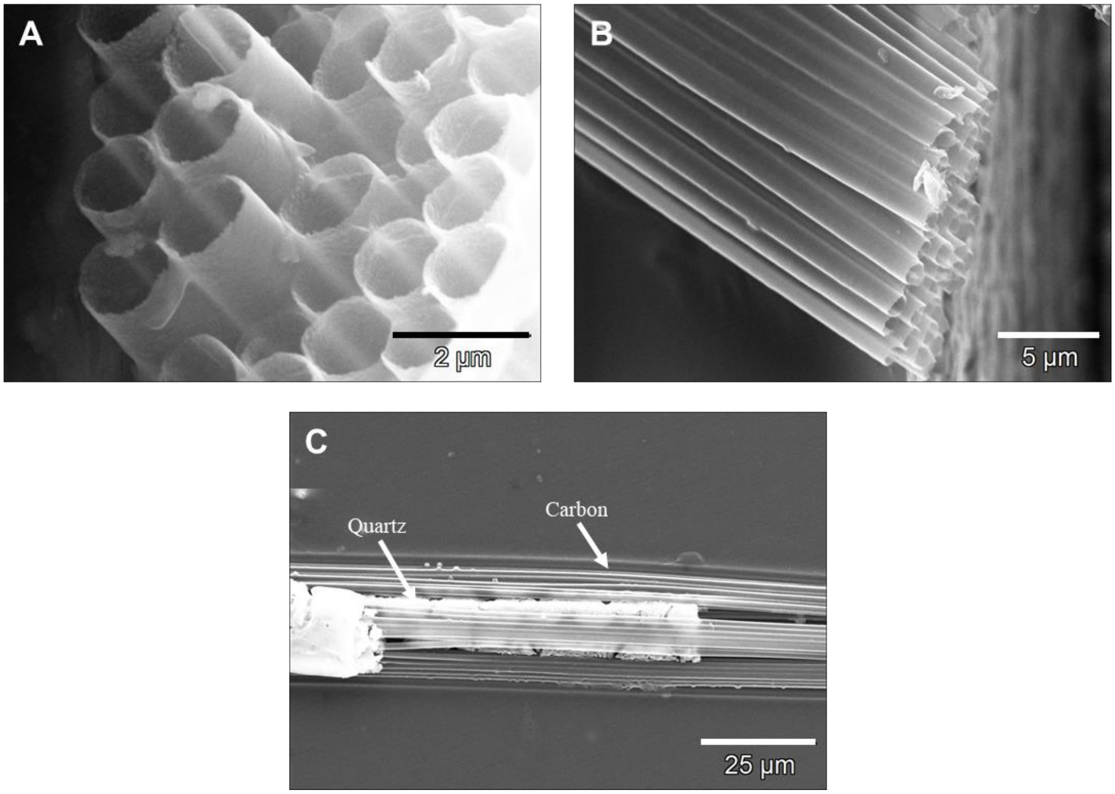

Figure 2-17: SEM micrograph of photonic crystal fiber CNSs. A) and B) Exposed carbon micropipes formed using photonic crystal fiber as a template for CVD C) The three-step template-based manufacturing process enables the fabrication of carbon micropipes with high aspect ratios.

2.4. Diatom

Diatoms contain nanometer to micrometer dimensioned pores within a cell wall ranging from approximately 2 µm to 2000 µm diameter cell wall [72]. Diatoms are unique in that they contain species-specific, hierarchically organized pores as small as 10 nm in diameter and spanning orders of magnitude. This enables the fabrication of integrated micro- and nano- carbon pipes in a single manufacturing process.

Table 2-6: Carbon Deposition Parameters for Diatoms

Template	Temperature [°C]	Ethylene/Helium [sccm]	Duration [h]
Diatoms	500	165	4

2.4.1. Template Selection and Formation

As diatoms already have micro- and nanoscale pores, no additional template formation steps were required. Diatomaceous earth was mixed with distilled water and droplets were placed on a quartz sample holder for the CVD process.

2.4.2. Carbon Deposition

The diatoms were utilized in a CVD process performed in a three-stage furnace (Carbolite, TZF17/600, inner tube diameter: 7cm, tube length: 152cm). Again, argon was utilized to remove oxygen from the system while a 30/70 (vol%/vol%) ethylene/helium gas mixture was used as the carbon source, as described in Table 2-6. A floating ball rotameter and electronic flow meter were utilized to regulate the flow of the argon and ethylene/helium mixture, respectively. As in the case of the other templates described above, the samples were positioned in the center of the tube.

2.4.3. Template Removal

Carbon flakes that encapsulated the diatoms, visible in Figure 2-15 B, were removed from the sample holder after CVD and epoxied to an acrylic slide. The slide was completely submerged in a BHF bath overnight (~15 h) to selective etch the diatom template leaving carbon structures embedded in a carbon film shown in Figure 2-15 C.

2.4.4. Results and Discussion

Removal of the diatom template via selective wet-etching resulted in carbon micro- and nanostructures embedded on a carbon flake. These carbon micro-structures had an average diameter of 0.42 µm with a wall thickness of 65 nm while the carbon nanostructures had diameters of sub 200 nm. Although a sample geometry of an etched diatom is presented in Figure 2-18 B-E, it can be expected from Figure 2-18 A that many different formations of nanostructures could be fabricated from diatom templates depending on the specific species of diatom used.

2.5. CONCLUSIONS

The work presented here demonstrates a methodology for fabricating a diverse range of carbon micro- and nanostructures using a three-step template-based manufacturing technique. The scale and geometry of the carbon structures is controlled by template selection. A low-cost, high-throughput CVD process was utilized to deposit carbon within novel macroscale silica-based templates with micro- and nanoscale bores and pores. This work demonstrates the versatility of this manufacturing process and the effect that template selection has on the resultant CNS. The resulting carbon-structures were designed to readily interface with standard laboratory equipment due to their direct integration into macroscale devices without additional micro- or nanoassembly.

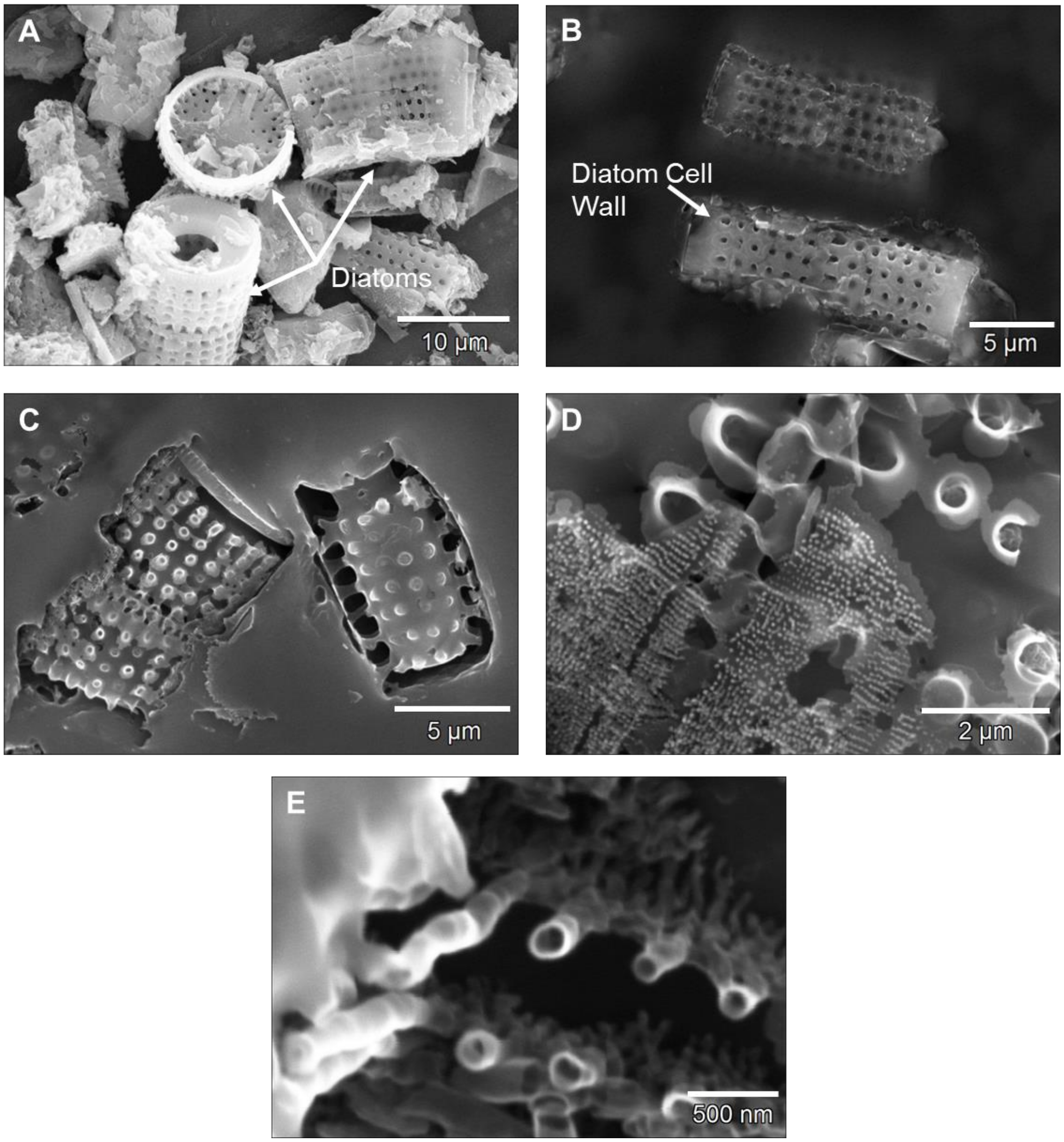

Figure 2-18: SEM micrograph of diatomaceous CNSs.
A) Diatomaceous earth containing many diatom geometries which are utilized as templates for CVD B) Diatoms coated and embedded in carbon after CVD C) Exposed carbon microstructures after template removal via selective wet-etching of the diatom cell wall D) Exposed carbon structures spanning orders of magnitude in diameter E) Carbon nanopipes formed using diatoms as a template.

Chapter 3

3. DESIGN AND FABRICATION OF A NANOSCOPIC THERMOCOUPLE

The template-based manufacturing process described in Chapters 2 inspired the development of a nanoscopic thermocouple. The single barrel micropipette described in Section 2.2 was used as a scaffold on which to deposit thin dissimilar metallic films. These films generate electromotive forces when exposed to temperature gradients enabling the sensor to provide thermal characterization of environments. The performance of the thermocouple was characterized in aqueous baths. The material selection provided an improved thermoelectric power compared to other pipette-based thermocouples. In this section the development and characterization of the thermocouple is described.

3.1. BACKGROUND

3.1.1. Thermocouple Principles

Thermocouples produce a temperature-dependent voltage because of the thermoelectric effect. When two dissimilar metals (A and B) are joined at two junctions (T_{sense} and T_{ref}), an electromotive force (*emf*) is generated due to the temperature differential of the two junctions, as described in Figure 3-1. If both junctions are maintained at the same temperature, an equal and opposite emf will be generated at the junctions and the net *emf* will be zero. However, if the junctions are held at dissimilar temperatures, a non-zero emf will be generated. This temperature-dependent voltage,

V_{emf}, generation is known as the Seebeck effect. When connected to a voltmeter, thermocouples exploit the Seebeck effect to enable temperature measurements.

$$V_{emf} = \int_{T_{ref}}^{T_{sense}} (S_B - S_A)\, dT \tag{3-1}$$

where S is the Seebeck coefficient of conductors A and B, a measure of the magnitude of the emf generated in response to a temperature difference across the material. Temperature, crystal structure, and impurities influence the value of the Seebeck coefficient. Most importantly, the Seebeck effect is attributed to charge carrier diffusion [73].

Charge carriers, such as electrons, exist and constantly diffuse inside conductive materials [74]. Within the material, the energy with which these electrons travel varies in response to thermal fluctuations [75]. In the absence of a temperature difference, the charge carrier diffusion balances and thus no current is generated. However, when a temperature gradient is applied across the material, the hot end of the material experiences an increase in the concentration of high-energy charge carriers and a decrease in the concentration of low-energy carriers. The high-energy charge carriers diffuse from the high-energy hot end of the material and move towards the lower energy cold regions. Simultaneously, the low-energy charge carriers diffuse away from the low-energy cold regions to the higher energy hot regions. As these two diffusion processes work counter to each other, a net current is only generated if one of these drifts is stronger than the other. Thus, the thermoelectric coefficient, S, of a material depends on how conductive the high-energy charge carriers are relative to the low-energy charge carriers. The sign of S indicates which direction of charge carrier diffusion dominates.

The distance between the hot and cold junction does not affect the temperature-dependent voltage however practical considerations of thermal conduction forces the junctions to be positioned apart such that a known reference temperature can be maintained.

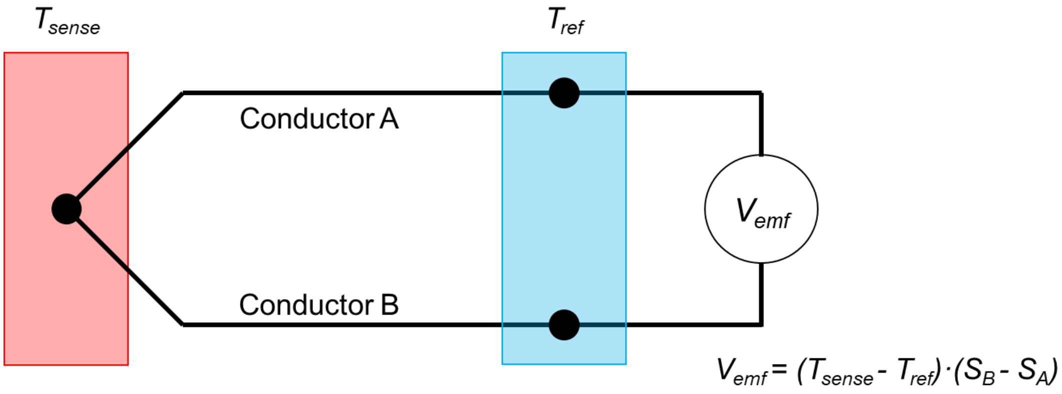

Figure 3-1: Schematic of the thermocouple working principles.

Care needs to be taken when selecting materials for the thermocouple. Dissimilar metals must be used when designing a thermocouple. If the materials used for each leg are the same or have an equivalent Seebeck coefficient, the same voltage will be generated along the length of each wire and no voltage difference will be generated at the sensing junction. It is advantageous to select two materials with very dissimilar Seebeck coefficients to ensure a large voltage difference is generated between the two metals. The difference of the Seebeck coefficients of the two materials determines the thermoelectric power, and thus the sensitivity, of the thermocouple. It should be noted that the term thermoelectric *power* (unit of $V \cdot K^{-1}$) is a misnomer as this term does not express a power (unit of W) quantity. A high sensitivity will allow the thermocouple to better overcome the overall noise in the data acquisition system and thus, resolve smaller temperature variations. A high sensitivity is required to adequately resolve and characterize the temperature profile in such a system especially as the measurement tip diameter becomes smaller. This requirement has led to the investigation of micro and submicron thermocouples.

3.1.2. Micro and Submicron Thermocouples

The maximum thermoelectric power of micro and submicron thermocouples is limited by the Seebeck coefficient for the bulk materials. However, the thermoelectric power achieved by these thermocouples is often less than that predicted using the bulk values. As described above, the thermoelectric behavior of a metal is dependent on the conduction mechanisms of the charge carriers in the crystal lattice. The thermoelectric power of a thin film can be related to the conduction mechanism of free electrons as follows:

$$\alpha = \frac{\pi^2 k^2 T}{3e\zeta}\left\{\frac{d\ln\lambda(E)}{d\ln(E)}\right\}_{E=\zeta} \qquad 3\text{-}2$$

where α is the thermoelectric power, k is the Boltzmann constant, e is the electron charge, T is the absolute temperature, ζ is the Fermi energy, λ is the mean free path of conduction, and E is the electron energy [76]. It is well established that the mean free path depends on the film thickness and quality [77,78]. As the film thickness is reduced, charge carriers are no longer able to be transferred as effectively from the hot and cold regions of the thermocouple. Thus, the thermoelectric power of micro- and ultramicro-thermocouples will be lower compared to macroscale thermocouples made of the same materials. This phenomenon is reflected in the literature as the submicron thermocouples reported have a reduced thermoelectric power indicating that the quality of the thin metal films and wires is insufficient. Due to this inevitable reduction in thermoelectric power as the scale of the thermocouple is minimized, care should be taken to select materials that have a large difference in Seebeck coefficient.

Beckman *et al.* developed chromel-alumel and chromel-constantan microscale thermocouple and reported the subsequent characterization [79]. In this work, two 0.02 mm wires were welded to form a 0.06 mm diameter junction. This spherical junction was clamped between two tungsten plates to flatten it into a thin disk with a thickness of 2.5 µm and diameter of 80 µm. The two lead wires were inserted into a thin and flexible double-bore quartz rod to electrically insulate the wires. This assembly was inserted into a stainless-steel sheath and the wire element leads were fused to larger diameter wires. Finally, the device was inserted into a 3.22 mm diameter stainless-steel tube and the lead wires were separated from the tube with epoxy. This micro thermocouple was used at a stationary point in a subcooled flow boiling experiment which consisted of discreet vapor bubbles in a flow of Refrigerant-113. In this experiment the vapor remains at or close to the saturation temperature while the liquid temperature may be significantly lower. The authors demonstrated that the thermocouple was able to distinguish the temperature of individual vapor bubbles from the continuous fluid. As predicted, the vapor bubbles had a temperature of approximately the saturation temperature of 80.1 °C while the mean fluid temperature was considerably lower at approximately 75 °C.

Thin-film thermocouples which rely on junctions formed by evaporated metal films have been used as small scale temperature sensors [80,81]. For example, Allen *et* *al*. used microfabrication patterning techniques and electroless and deposition to create a silver-nickel thermocouple [82]. To achieve this, a glass slide was prepared by sonicating in acetone, hydrolyzing the surface in a boiling water/ammonium hydroxide/hydrogen peroxide mixture, and then cleaning in soap, water, and ethanol. Then microchannel mold was prepared by contact photolithography on a silicon wafer. This mold was used to prepare PDMS stamps for the electroless and electrolytic patterning of thin metallic films. Firstly, the PDMS stamp was placed on the prepared glass slide and the microchannels were filled with a sensitizing agent composed of stannous (II) chloride in hydrochloric acid. This procedure was repeated with an activating solution consisting of palladium (II) chloride in hydrochloric acid. Both the sensitizing and activating solutions degrade rapidly and therefore must be prepared daily. The PDMS microchannel stamp was filled with an electroless nickel plating solution was used to deposit a thin line of metal. The nickel film was annealed and then electrolytically plated with another thin layer of nickel. The PDMS stamp was rotated to create an intersecting, perpendicular line to the nickel line. A commercially available electroless silver plating solution was used to deposit a thin line of metal as above. The device was annealed again, and a thin layer of silver was electrolytically deposited. The PDMS stamp was removed and the device was annealed in an inert environment. Through this procedure the authors were able to fabricate thermocouples with sensing areas of 50 – 500 μm^2. This thermocouple was used to monitor on-chip temperature fluctuations induced by temperature fluctuations. The device was positioned within a microchannel and two inlets were used to introduce and mix hydrochloric acid and sodium hydroxide resulting in an exothermic reaction with a predicted maximum temperature change of 7.1 °C. The thermocouple measured a temperature increase of approximately 5 °C.

Flat nanoscale thermocouples based on nanowires have also been explored. Shapira *et al*. developed a thermocouple based on segmented gold and nickel nanowires [83]. First, silver was evaporated onto a 60 µm thick porous alumina oxide membrane with 170 nm pores. This layer served as an electrode for an electrodeposition process to deposit gold and nickel segments into the pores. The silver layer was then dissolved with nitric acid and then the alumina membrane was dissolved in heated sodium hydroxide to release the gold-nickel nanowires. A drop of the suspended nanowires was placed onto a silicon wafer coated with a 1 µm thick oxide layer and 80 μm^2 contact pads were fabricated using electron beam lithography and evaporation of a chromium/gold layer. The resulting devices consisted of 10 – 20 µm long nanowires. The location of the gold-nickel junction was not consistent among multiple devices. The design of this device results in three temperature junctions: one at the gold-nickel junction of the nanowire, one at the gold contact pad, and one at the nickel contact pad. The maximum distance between the sensing region (gold-nickel junction) and the reference region (the contact pads) is 10 µm and can be as little as 5 µm which can lead to challenges in maintaining the reference temperature. Thus, the authors induced self-heating in the device by applying a 50 µA current for a local heat generation. The authors did not report a measured Seebeck coefficient of the thermocouple and relied on the values for bulk materials to predict the thermoelectric power of the device and interpret measured voltages.

3.1.3. Micropipette Based Thermocouples

In a review article published in 2019, Brandner expressed the importance of and difficulty in maintaining a reference temperature in miniaturized thermocouples [84]. The metals used in thermocouples leads to very fast conduction from the sensing area to the reference area and thus the temperature difference between the sensing and reference junctions can diminish rapidly.

Micropipette-based thermocouples have been explored as they can be produced without tedious microassembly processes and are readily integrated into scanning probe microscopes. This enables their use in characterizing orders-of-magnitude larger regions with extremely high spatial resolution. Moreover, their high aspect ratio (tip diameter versus the distance between the junctions) allows one junction to be maintained at a reference temperature easily.

Fish *et al.* reported a thermocouple consisting of a solid platinum core encased in a gold-coated glass micropipette [85]. To achieve this, an 80 μm diameter platinum wire was inserted into a borosilicate capillary with an inner and outer diameter of 0.3 mm and 1.2 mm, respectively. This assembly was drawn using a commercially available laser pipette puller resulting in a platinum-filled micropipette with a tip as small as 50 nm. A gold film was vacuum-evaporated onto the outer surface of the platinum-filled micropipette with a maximum thickness of 300 Å. This work reported a thermoelectric power of 7 $\mu V \cdot K^{-1}$. However, using Seebeck coefficients available in the literature and, assuming the best scenario that bulk properties are retained, it was predicted that the thermoelectric power of the thermocouple was 5.83 $\mu V \cdot K^{-1}$. As described in Section 3.1.1, it is well established in the literature that it is not possible for the measured thermoelectric power of a microscale thermocouple to exceed that predicted by the Seebeck coefficients of the bulk materials [73–78,86]. This is because the mean free path of electrons is known to decrease as the film thickness is reduced and thus the charge carriers are unable to flow as efficiently in response to a thermal gradient. The authors did not attempt to explain why the measured thermoelectric power exceeded the theoretical limit which casts doubt on the validity of their results.

The response time of the thermocouple developed by Fish *et al*. was characterized by using the thermocouple measure temperature changes in an aqueous droplet induced by a focused argon-ion laser beam with a wavelength of 1.064 μm. The thermocouple was submerged in droplets with no obvious convection. Sub-microsecond pulses of near-infrared laser light was used to illuminate the droplet. As the droplet was transparent at the wavelength of the laser, only the thermocontact region of the thermocouple adsorbed heat. The kinetics of the thermocontact region cooling was monitored with sub-microsecond resolution and a response time of 300 ns was measured. The thermocouple was also used to monitor laser-induced cavitation bubbles to demonstrate its ability to monitor rapid thermal processes. The thermocouple was held at a fixed distance from an optical fiber. The optical fiber was used to deliver 20 ns pulses of a 193 nm wavelength laser to an aqueous NaCl droplet positioned on the end of the fiber. The energy delivered to the droplet caused evaporation of the fluid near the fiber, resulting in boiling within the droplet. As these bubbles grew, they would contact the thermocouple which would record the temperature as it passed through the liquid and vapor phases. Finally, the thermocouple was used with a near-field scanning optical microscope to demonstrate the thermal imaging capabilities of the sensor. The thermocouple was scanned through the tip of a 2 μm laser beam spot with a maximum temperature of 150 °C. Through this work the authors were able to generate thermal images of the focal spot of the laser beam.

The technology developed by Fish *et al*. was commercialized through Nanonics Imaging Ltd. The thermocouple probe is marketed as a tool for static and dynamic thermal measurements when used as an atomic force microscopy probe. This sensor has been used to characterize the heat transport through gold electrodes on silicon and the temperature distribution of plasmonic structures for applications in controlled heating of liquids, thermal photovoltaics, nano-electrochemistry, heat-assisted magnetic memories, and nanolithography.

In 2001, Kakuta *et al*. reported a hollow pipette-based thermocouple [86]. A glass micropipette was used as a scaffold onto which layers of platinum, polyimide, gold, and 2-methacryloyloxyethyl phosphorylcholine copolymer were deposited. To produce this thermocouple, first a glass capillary was drawn into a 50 mm long micropipette with a 1 μm diameter tip using a hot wire pipette puller. Next, a 10 nm thick chrome film and 30 nm thick platinum film were deposited onto the surface of the micropipette by physical vapor deposition. An insulating polyimide layer was then applied to the micropipette surface. A gold thin film was deposited by physical vapor deposition. Another coating of polyimide was applied to the gold. Finally, a coating of 2-methacryloyloxyethyl phosphorylcholine copolymer was applied to provide biocompatibility. This process produced a hollow thermocouple with a tip diameter of over 1 micron. The authors reported that there was issue with the coatings at the junction which resulted in leakage current which would need to be investigated in future work.

The thermoelectric power of the thermocouple developed by Kakuta *et al*. was determined by calibrating the sensor in a temperature controlled aqueous bath. While gold and platinum were selected as they are amenable to ion-sputtering however, the theoretical Seebeck coefficient between the two metals is 5.83 $\mu V \cdot K^{-1}$ and the averaged measured thermoelectric power of the thermocouple was 2.1 $\mu V \cdot K^{-1}$ (max 5.0 $\mu V \cdot K^{-1}$). The authors articulated the necessity of using a pair of metals whose thermoelectric power is greater than that of platinum/ gold to improve the performance of future thermocouples. While the thermocouple was designed to enable the delivery of reagents, the capability was not explored in this work.

Later, the same group attempted to utilize the thermocouple to characterize cellular thermal responses [87]. The thermocouple was used to deliver norepinephrine into brown adipocytes. The authors proposed that the introduction of norepinephrine into cells would lead to a thermal response that could be captured by the thermocouple. However, the thermocouple was unable to detect any temperature change in the cell. The authors proposed to investigate alternative metal combinations to improve the resolution of the thermocouple to be able to overcome the signal-to-noise ratio.

In 2011, Shrestha *et al.* investigated a micropipette-cased thermosensor with the intention of cellular-level thermal characterization [88]. This thermocouple consisted of a solid tin-based solder core encased in a nickel coated glass pipette. A borosilicate micropipette with a submicron tip opening was filled with a molten lead-free tin solder alloy by an injection molding process while simultaneously locally heating the pipette tip. The tip was beveled to remove any excess metal and sharpen the tip. Nickel was physically vapor deposited onto the exterior of the micropipette to form a nickel-tin junction at the beveled tip. The tip was then coated in silver to reduce cytotoxicity. This resulted in a sensor with a tip size of 2 to 30 μm.

The thermocouple was calibrated in a thermally insulated water bath from 35 °C to 39 °C and recorded a thermoelectric power of 8.46 to 8.86 $\mu V \cdot K^{-1}$. The standard deviation in the voltage measurements was 18 nV corresponding to a temperature resolution of 0.002 °C. The thermocouple was then used to interrogate live retinal pigment epithelium cells (10 – 20 μm) exposed to irradiation from a green laser beam focused to a spot size of 6 μm on the focal plane. During the 1.5 s laser-cell interactions, the thermocouple recorded the temperature of various cells as it rose from a baseline of approximately 25 °C to a maximum of 38 °C - 55 °C and subsequently cooled. The cell viability was confirmed by monitoring with a calcein fluorescent dye before and after laser irradiation.

In 2014, Zhang *et al.* reported a fabrication method for a thermocouple microelectrode for scanning electrochemical microscopy applications [89]. While this work also relied on a glass capillary, it differs from other micropipette-based thermocouples as it relies on a platinum-platinum/rhodium junction formed from two wires. Platinum and platinum/rhodium wires with a 25 μm diameter were thinned via electrochemical wet etching. The wires were inserted into the barrels of a theta capillary to electrically isolate them and the exposed ends were joined into a spherical junction by melting in a flame. The theta capillary was inserted into the large end of a borosilicate micropipette. The two capillaries were sealed heated and sealed with epoxy. The micropipette tip was polished with 0.05 μm alumina particles. This work resulted in 20 μm thermocouple with a theoretical Seebeck coefficient of 4.93 $\mu V \cdot K^{-1}$ while the measured Seebeck coefficient was not reported. The thermocouple was used as a scanning electrochemical microscopy tip to characterize the thermal profile of a circuit board.

The micropipette-based thermocouples described above have provided improvements in aspect ratio and ease-of-manufacture however they often have a reduced thermoelectric power due to their refined size and limited material selections. Thus, it is important to develop thermocouples with materials that enable better thermoelectric power without sacrificing the size of the sensing area.

3.1.4. Applications

The quantification of spatially localized temperature changes has relevance in studies of many physical and biological processes and systems including turbulent flows, cellular and subcellular biology, chemical reactions, point radiation microdetection, and microscopic domains [85,90]. Micro- and submicrometer thermocouples have emerged as useful tools for the thermal characterization of such microdomains. These thermocouples have provided improved spatial resolution and response times around a microsecond due to their reduced dimensions.

The spatial resolution of thermocouples refers to the distance over which changes in temperature can be repeatably resolved. The spatial resolution depends not only on the size of the thermocouple junction but also the temperature gradient of the system in which the sensor is operating. For a given temperature gradient, the spatial resolution is governed both by the thermocouple tip size and sensitivity (*i.e.* the change in voltage per temperature change). In an adequately high temperature gradient, the tip size is the limiting factor as significant temperature changes occur over the diameter of the tip and sharp temperature changes are averaged out. For systems with small temperature gradients, the sensitivity of the probe becomes the limiting factor as the voltage changes over a distances larger than the tip size are not adequately large to be discerned by the data acquisition system, as illustrated in Figure 3-2.

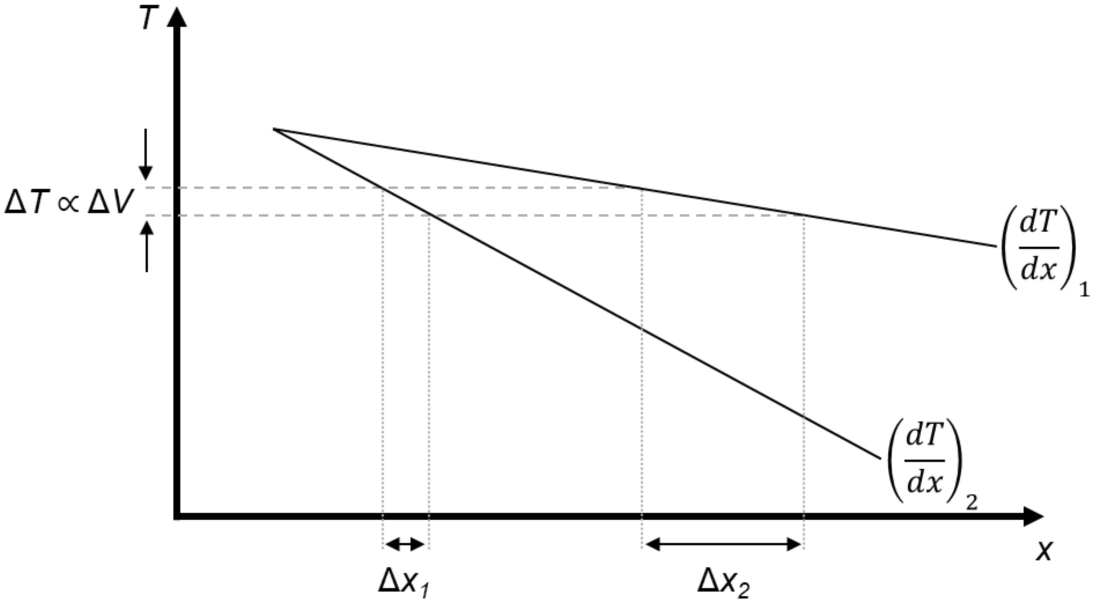

Figure 3-2: Schematic of the dependency of spatial resolution on the temperature gradient of the system assuming the tip size of the thermocouple is adequately small.

There are examples of using microscale thermocouples in high temperature gradient environments, such as boiling where bubbles in a subcooled liquid have a sharp temperature change at the infinitesimally thin vapor-liquid interface. For example, Delhaye *et al.* described the temperature fluctuations expected in such an experiment characterized by an increase in temperature as the vapor bubble approaches the thermocouple and the thermocouple enters the superheated liquid layer. When the thermocouple enters the bubble the temperature rapidly drops to the saturation temperature after the evaporation of remaining fluid on the thermocouple junction. The thermocouple remains at the saturation temperature while it is inside the bubble. As the thermocouple junction exits the bubble it again rises rapidly to the superheated liquid temperature before returning to the supercooled liquid temperature. Beckman *et al*. used a microscale thermocouple to detect the vapor phase (saturation temperature of 80.1 °C) of subcooled liquid.

An example of using a microscopic thermocouple in a system with small temperature gradients is found in cellular thermal sensing [91]. For example, cancer cells have been found to have temperatures 1.5 °C than normal cells due to increased metabolic activity [92]. Hyperthermia therapy uses temperatures exceeding 40 °C to damage cancer cells and thus requires an understanding of the influence of external environment on cells [93]. Further, subcellular temperature variations can arise in response to metabolic activities or exposure to pharmaceuticals. For example, localized heat production has been noted in the endoplasmic reticulum of cells after treatment with ionomycin, a molecule which causes an influx of calcium from the extracellular medium [94]. Certain compounds, including Carbonyl cyanide 4-(trifloromethoxy)phenylhydrazone (FCCP) and carbonyl cyanide 3-chlorophenylhydrazone (CCCP) cause heat generation in mitochondria [95]. Activities including DNA replication and transcription and RNA processes can cause a temperature difference of 0.96 °C between the nucleus and the cytoplasm [96].

Infrared thermography has been used to study temperature changes within cells but has a spatial resolution of only ~10 µm [97]. Organic fluorophores have been investigated for cellular thermography but are limited by photobleaching and pH sensitivity. Thus, micro- and nanoscale thermocouples have emerged as an area of interest for thermal characterization of cells.

Watanabe *et al*. and Shrestha *et al*. utilized microscale thermocouples to quantify temperature changes in individual living cells [87,98]. Watanabe *et al*. utilized a platinum-gold microthermcouple with a tip diameter of just over 1 µm to detect chemically induced temperature changes in adipose cells. However, the sensitivity of their thermocouple was not sufficient to overcome the noise in the data acquisition system and detect temperature changes. Shresta *et al*. used a tin-nickel thermocouple with a tip size of 2 µm to monitor laser induced temperature increases in cells. By using a thermocouple with a higher sensitivity and using a method of heating that lead to a larger temperature change, this group was able to quantify 12 °C temperature increases in the cells. However, due to the large tip diameter of the thermocouple they were unable to measure temperature gradients within the cell. Bai and Gu described the advantages offered by micro-thermocouples for cellular and subcellular thermal characterization while noting that the relatively large tip-size and low sensitivity of available sensors currently limit their use in such biological applications [91].

The characterization of the thermal conductivity of thin films (less than 1 µm) can be challenging due to the experimental requirements. Large thermocouples are not appropriate for such conditions as the lead to a significant heat loss due to convection. Traditional plate techniques of thermal conductivity measurement are dominated by interfacial thermal resistance rather than thermal conductivity of the thin film [99]. Thus, microthermal couples have emerged as useful tools to overcome these limitations and characterize the thermal conductivity of thin films [98]. However, as described in Section 3.1.2 the sensors used in such studies have a low thermoelectric power, relatively large tip sizes, and complex manufacturing requirements.

Small-scale thermocouples have also been employed in the temperature characterization of plasmonic devices. In 2014, Desiatov *et al.* identified one of the main challenges in thermal plasmonics is the lack of methods to accurately map the temperature profile of plasmonic devices [100]. Non-contact methods have been explored to overcome this obstacle however the spatial resolution of far-field techniques is limited by diffraction. Thus, the authors expressed the need of contact methods, including thermocouples, with adequately high spatial resolution resulting from a small tip size. The authors used a commercially available nanoscale thermocouple produced by Nanonics Imaging, Ltd. to map the temperature profile of a plasmonic device.

3.1.5. Thermocouple Design

To improve the sensitivity of micropipette-based thermocouples, alternative metal pairs were investigated. Nickel and gold were identified as they have Seebeck coefficients of -18.0 and +1.79 $\mu V \cdot K^{-1}$, respectively [101]. By taking the difference between the S of each material, the maximum thermoelectric power of a gold-nickel thermocouple is predicted to be 19.79 $\mu V \cdot K^{-1}$ which is higher than other micropipette-based thermocouples reported in the literature, as summarized in Table 3-1. While gold has been utilized in existing micropipette-based thermocouples, nickel has not yet been explored. Two possible manufacturing methods emerged to integrate nickel into the system. Firstly, a nickel wire could be sealed into a quartz capillary and drawn into a pipette using a laser-based pipette puller as commonly described in gold-platinum micropipette thermocouples. However, while there has been reports of sealing tungsten, stainless steel, and platinum in glass pipettes, this method has not been investigated with nickel wires. The second method involved depositing a nickel film on the pipette lumen. Traditionally, physical vapor deposition has been employed to deposit metallic films on the exterior of micropipette-based thermocouples however, due to practical limitations, this method is not conducive to depositing a film on the lumen of a pipette. There are commercially available solutions for the electrolytic deposition of nickel however these require an electrically conductive surface which does not exist on a glass pipette.

To overcome this obstacle, the thermocouple described in this chapter relies on the carbon-based single barrel micropipette described in Chapter 2. The carbon film serves as an electrode and enables the controlled deposition of nickel onto the lumen of the pipette, as seen in Figure 3-3. The quartz pipette serves as an electrically insulting layer between the two metallic films. Quartz also has a low thermal expansion and good thermal shock resistance which serves to prevent disruption of the metallic layers deposited on the template. A thin gold film is then deposited onto the exterior surface of the pipette via traditional physical vapor deposition methods. A junction is formed between the gold and nickel at the tip of the pipette and a second junction is formed at the macroscale end of the pipette. As mentioned above, it is important to have a high aspect ratio thermocouple to enable the maintenance of a reference temperature. Micropipettes have high aspect ratios and thus are good candidates for thermocouple templates.

As the exterior metallic film is formed from gold, the least reactive metal, degradation due to corrosion or oxidation is avoided. Nickel is also a nonreactive metal and when exposed to oxygen forms a thin protective coating of nickel oxide which prevents further corrosion from occurring. The low reactivity of the metallic films is expected to enable the thermocouple to perform well in a variety of practical environments.

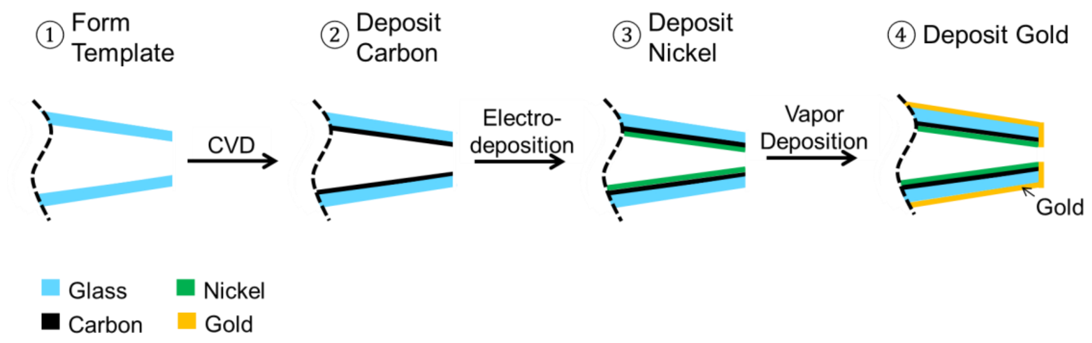

Figure 3-3: Schematic of the thermocouple fabrication process. Schematic of the steps involved in the manufacturing process: (1) a template is formed by drawing a quartz capillary into a nanopipette, (2) a thin layer of carbon is deposited within the template using chemical vapor deposition, (3) a layer of nickel is electrodeposited on the lumen (4) a layer of gold is vapor deposited onto the surface of the pipette.

The described thermocouple offers several advantages offer currently available micropipette-based thermocouples. Firstly, the proposed thermocouple has a higher thermoelectric power than similar sensors reported in the literature which will provide enhanced temperature sensitivity. The thermocouple has a minimized tip diameter to offer improvements in spatial and temporal resolution. The template-based manufacturing method is flexible and amenable to many different length-scales and geometries. Further, the manufacturing process was designed to enable the fabrication of a hollow thermocouple to simultaneously deliver reaction-enabling materials into microdomains and detect corresponding changes in temperature.

3.2. METHODOLOGY

3.2.1. Thermocouple Fabrication

The carbon-based thermocouple is manufactured in four main processing procedures: (i) Fabricate a single barrel carbon-based nanopipette as described in Section 2.2; (ii) Coat the lumen with nickel (iii) Coat the exterior of the pipette with gold (iii) Establish an electrical connection to the nickel and gold films at the macroscale end of the probe to enable direct interfacing with standard electrochemical equipment.

Fabrication of a Single Barrel Carbon Nanopipette

A single barrel quartz pipette was coated with carbon as described in Section 2.2. Briefly, a quartz capillary (Sutter Instruments) was drawn into a micropipette using a laser-based pipette puller (Sutter Instruments, P-2000F). The micropipette was used as a template in a CVD process which deposited a layer of carbon on the lumen of the pipette. For this work, the quartz template at the pipette tip was not removed. To ensure that the tip was not completely filled with carbon, filtered (20 nm pore size filter, Anotop 10 Plus, Whatman™) 15 µM rhodamine B labeled dextran (Invitrogen™, excitation/emission (nm): 555/580) was ejected from the tip of the pipette using an injection system (Eppendorf Femtojet) and observed under an optical microscope (AxioObserver.A1m, Zeiss) with a Cy 3 filter. As seen in Figure 3-4, the device was able to deliver the dextran into an aqueous environment.

Electrodeposition of Nickel

The carbon coated pipette was filled with 5 µL of Watts Nickel Plating Solution (Transene Company Inc) via a Microloader tip (Eppendorf) after preheating the solution to 50 °C. A preliminary electrical connection was established with the carbon film by a crimped tin-coated copper wire. A 60 pA current was applied for 90 s to form a nickel film on the carbon coating via electrodeposition. The tin-coated copper wire was removed once the electrodeposition process was completed. Any remaining plating solution was aspirated with a Microloader tip from the macroscale end of the pipette.

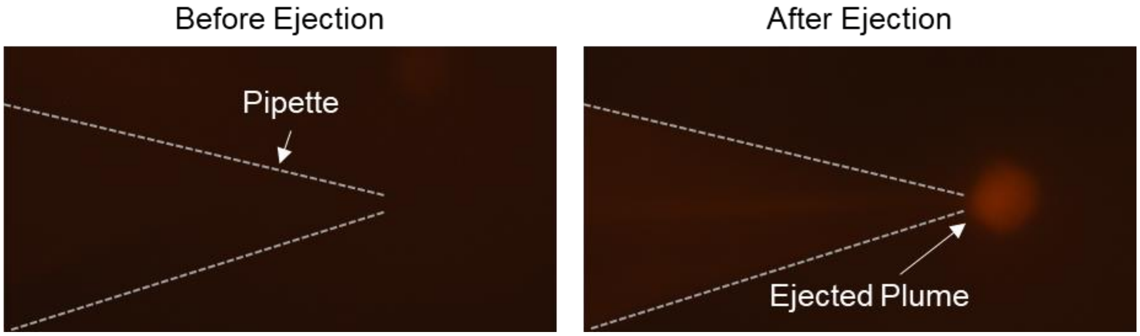

Figure 3-4: Ejection from micropipette.
Before and after ejection of rhodamine B labeled dextran from the tip of a single barrel pipette into an aqueous environment. Images were brightened for clarity.

Physical Vapor Deposition of Gold

Gold was deposited onto the surface of the quartz pipette via physical vapor deposition using a SPI-Module Sputter Coater and Vacuum Base (SPI Supplies). A gold target was used with argon as a sputtering gas. The pipette was positioned horizontally in the vacuum chamber and an 18 mA current was applied for 120 s. The pipette was then flipped, and the process repeated to coat both sides of the pipette.

The thickness of the gold film formed via vapor deposition can be predicted as follows:

$$d = KI_pVt \tag{3-3}$$

where d is the thickness of the film in angstroms, K is an experimentally determined constant (0.17 $\text{Å}\cdot\text{A}^{-1}\cdot\text{V}^{-1}\cdot\text{s}^{-1}$ for gold used with argon), I_p is the plasma current (18 mA), V is the applied voltage (1 kV), and t is the sputtering time in seconds (120 s) [102]. Thus, it was predicted that a 36 nm thick film was deposited onto the surface of the pipette.

Establishing an Electrical Connection to the Nickel and Gold Film

To ensure that the gold and nickel films were not in contact at the macroscale end of the pipette a fine-grit sandpaper was used to mechanically remove any material layer. Electrical connections to the nickel film was established by inserting a tin-coated copper wire into the lumen at the distal end of the pipette. The wire was then adhered to the distal end of the pipette with dielectric wax (Apiezon, Wax W). As the macroscale end is directly integrated into the ultramicro tip, by connecting the film at the large end of the pipette, electrical connection to the tip was established. Another tin-coated copper wire was wrapped around the macroscale end of the pipette in contact with the gold film. This wire was again adhered to the pipette with dielectric wax with care taken to avoid contacting the two individual wires.

3.2.2. Thermocouple Characterization

Fabricated thermocouples were visualized with an upright microscope (Zeiss, Axio Scope.A1) and captured with a camera (Zeiss, Axiocam 503, mono) and Zen microscope software. Micrographs were generated by scanning electron microscopy with a Tescan Mira3 Scanning Electron Microscope at 20 keV and 20 - 40 kX magnification. Thermocouple dimensions were measured from these micrographs.

The steady-state thermal response of the thermocouple was characterized in deionized water at four different temperatures. Ice water (~0 °C), room temperature (~20 °C), warm (~40 °C), and hot (~60 °C) water baths were analyzed. The warm and hot water baths were actively maintained on a hot plate. The reference water temperature was simultaneously recorded with a K Type thermocouple (Omega, ± 2.2°C). The tips of submicron and reference thermocouples were submerged into the water bath at each temperature. The voltage was recorded immediately upon placing the thermocouple tip into the water bath. The voltage was recorded using a Gamry Reference 600 (Gamry Instruments). When preparing the standard curve of potential versus temperature, discrete data points from multiple experiments and sensors were averaged and used to determine the standard deviation.

3.3. RESULTS AND DISCUSSION

3.3.1. Thermocouple Fabrication

As seen in Figure 3-5, the thermocouple produced with this method had a tip diameter of approximately 475 nm which corresponds to the sensing area of the thermocouple. The deposited gold was in the form of a heterogenous film with a maximum thickness of approximately 60 nm. As seen in Figure 3-6, the length of the thermocouple was 4.5 cm resulting in a tip diameter-to-length aspect ratio of 10^6. Having a high aspect ratio will enable the maintenance of the reference temperature at the junction located at the macroscopic end of the pipette.

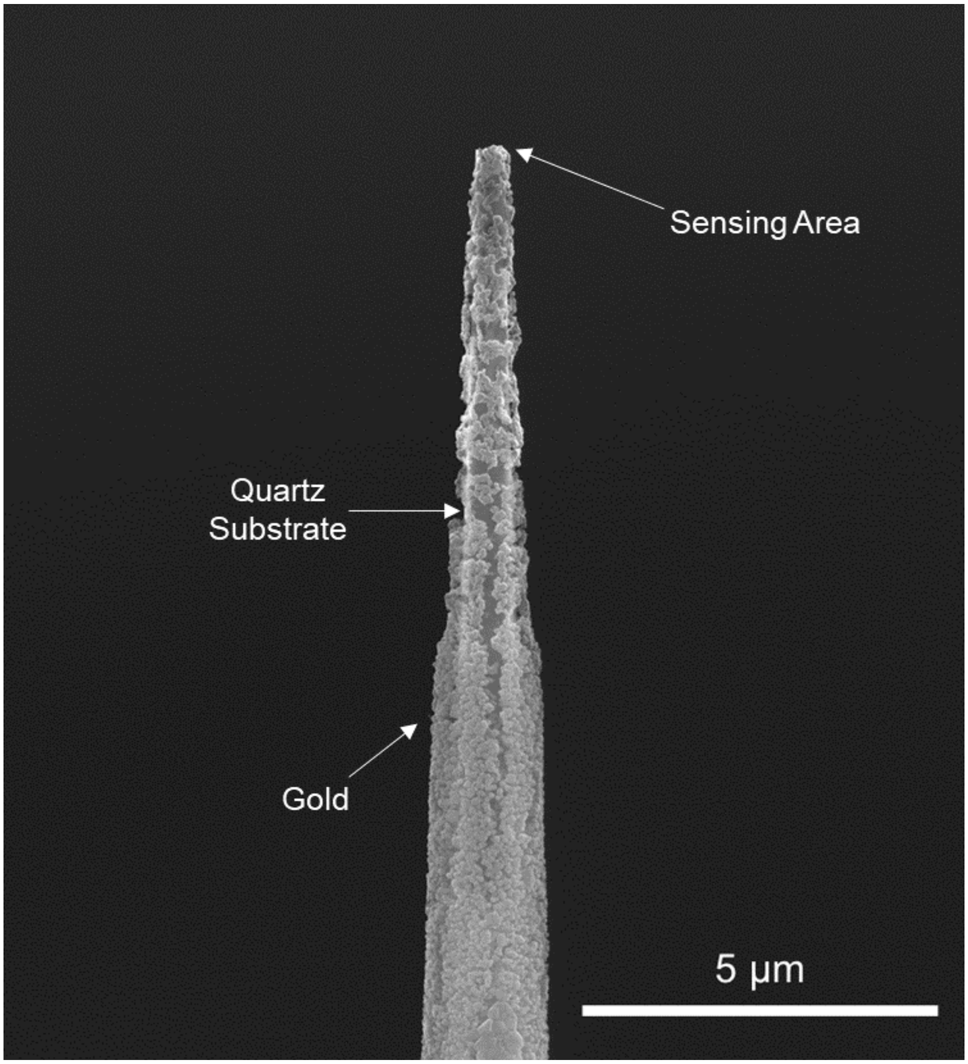

Figure 3-5: SEM micrograph of the thermocouple.

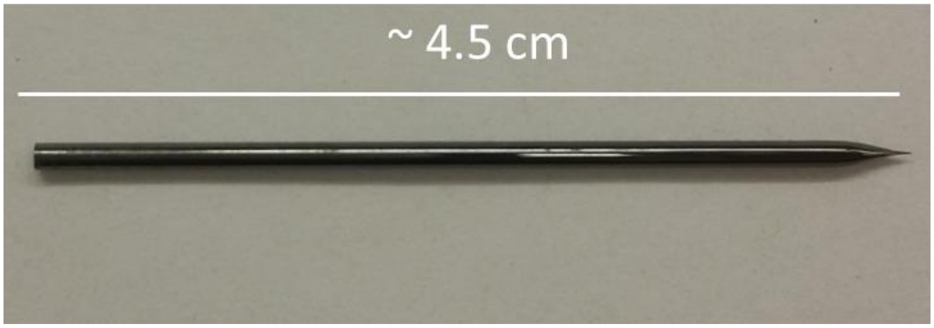

Figure 3-6: Image of entire micropipette-based thermocouple.

3.3.2. Steady-State Thermocouple Characterization

The thermoelectric performance of the thermocouple was characterized in an aqueous bath. The thermocouple generated an electric potential in response to changes in the junction temperature induced by submerging the micropipette tip in cooled, room temperature, and heated water baths. One thermocouple was used to record 7 continuous measurements each lasting 30 s with 1 data point collected per second (Figure 3-7).

It can be noted in Figure 3-7 that the thermocouple was able to respond to changes in environmental temperature consistently over several cycles. As predicted in Section 3.1.2, the response of the thermocouple was depressed as compared to the response predicted using Seebeck coefficients of bulk materials.

The response of the thermocouple was stable as shown by steady response of the thermocouple at ambient temperature where no or very minimal temperature changes are expected. The average response of the thermocouple over this period was -13.5 ± 1.2 µV. The standard deviation of the response is within the >2 µV rms noise and ripple, V_{rms}, of the potentiostat used in the data acquisition system as reported by the manufacturing company. The total peak-to-peak magnitude, $V_{p\text{-}p}$, of the noise and ripple is defined as follows:

$$V_{p-p} = 2\sqrt{2}\ \cdot V_{rms} \qquad 3\text{-}4$$

Thus, $V_{p\text{-}p}$ of the noise and ripple is 5.7 µV. As shown in Figure 3-8, all but one of the 60 data points collected over the 60 s period fall within the expected noise of the system. It can also be noted that although the two temperature junctions are at equivalent temperatures (ambient) the potential generated by the thermocouple is not centered on 0 V. This offset is likely due to the background noise of the system and could be eliminated by shielding the system with a Faraday cage during the experiment or background subtracting the data during post-processing as is standard practice in electrochemical experiments.

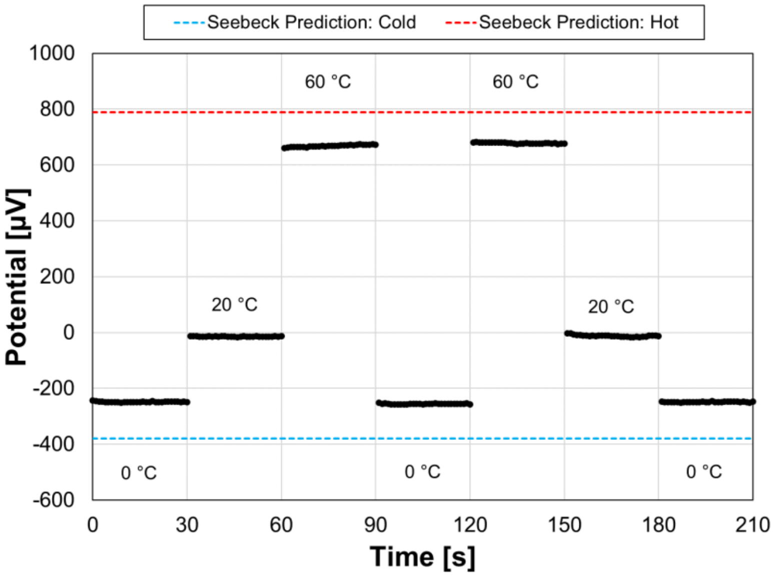

Figure 3-7: Thermocouple response in water baths.
The response of the thermocouple when submerged in water baths of varying temperatures. The dashed lines represent the values predicted by values of the Seebeck coefficient for bulk materials.

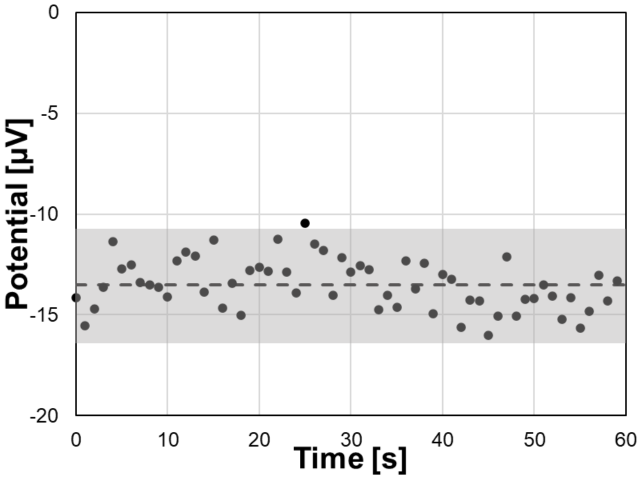

Figure 3-8: Thermocouple response at room temperature.
The response of the thermocouple at room temperature over a 60 s period. The dashed line is the average response and the shaded grey area represents the noise and ripple of the potentiostat reported by the manufacture.

In another experiment, a thermocouple produced in a different batch was used to collect 7 discrete data points in three different temperature baths. These 7 discrete data points were averaged with the final voltage recorded over the 60 s cycles shown in Figure 3-7 for each water temperature to generate the standard curve shown in Figure 3-9. The final voltage was selected to avoid averaging in the response of the thermocouple as the hot water bath was heating and the ice water bath was melting. A linear model of the form $y(x) = m \cdot x + b$ was fit to this data to determine the thermoelectric power. The slope, which indicates the thermoelectric power, was 14.9 $\mu V \cdot K^{-1}$ with an R^2 of 0.98. The thermoelectric power was predicted using the *S* values for the bulk materials (resulting in a thermoelectric power of 19.79 $\mu V \cdot K^{-1}$) and Equation 3-1 for the temperature range tested. As expected, the results obtained using the thermocouple were slightly less than the predicted thermoelectric power. As described above, the thermoelectric power of thin films is reduced compared to the bulk materials. This has specifically been observed for nickel thin films under 300 nm [83]. Further, Equation 3-1 also predicts this behavior, as described above. The heterogeneous gold film likely reduces the mean free path of the electrons thus reduces performance compared to the predicted behavior of bulk metals [88]. Even with these losses, the thermoelectric power of this thermocouple was still 68% higher than the best performing micropipette-based thermocouple available in the literature. This thermocouple performed comparably to larger silver-nickel thermocouples (silver and gold have the same *S* and are therefore expected to respond similarly). Despite having a significantly larger junction (50 µm^2 to 500 µm^2) and thicker metallic layers (above 1 µm) the microfabricated silver-nickel thermocouple produced by Allen *et al.* (described in detail in Section 3.1.2) had a thermoelectric power of 16 µV·K^{-1}, only 7% higher than the thermocouple produced in this work.

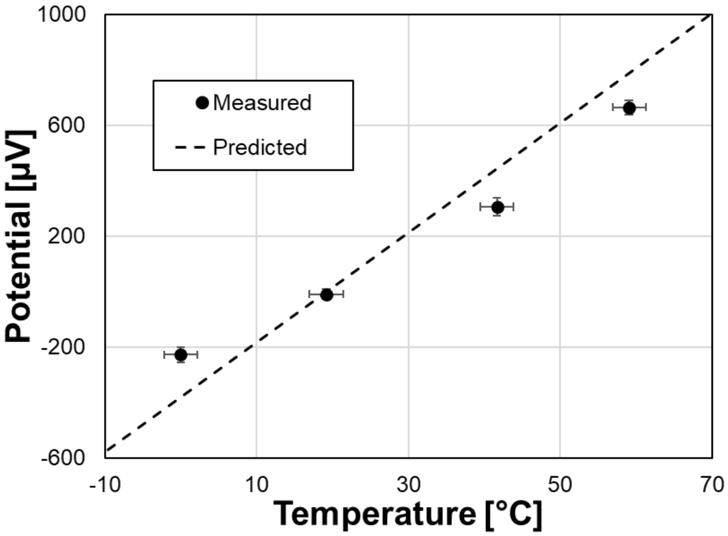

Figure 3-9: Standard response of the thermocouple.
Vertical error bars are the standard deviation in the measured potential generated by the thermocouple. The horizontal error bars are the error associated with a K-type thermocouple used to measure the temperature of the water bath. The dashed line represents the response of the thermocouple predicted using the Seebeck coefficients of the bulk materials, *i.e.* the maximum thermoelectric power.

The efficiency of the thermocouple is defined as the ratio of the electric energy generated to the thermal energy absorbed at the hot junction. The maximum efficiency is determined from the efficiency of both metals and the electrical and thermal losses resulting from connections and losses to the surroundings. When these losses are ignored, a figure of merit known as the Ioffe criteria, Z, which indicates the performance of thermocouples can be described as follows:

$$Z = \frac{\alpha_{AB}^2}{[(\rho_A \kappa_A)^{1/2} + (\rho_B \kappa_B)^{1/2}]^2} \qquad \text{3-5}$$

where α_{AB} is the thermoelectric power of the thermocouple, ρ is the electrical resistivity, and κ is the thermal conductivity of the two metals [103]. A higher Z typically is associated with a better performing thermocouple as it indicates that the device has a large thermoelectric power to produce adequate voltage and low thermal conductivity to minimize conductance between the hot and cold junctions and thereby maintain a reference temperature and a low electric resistivity to minimize Joule heating [104].

As determined above, the thermoelectric power of the thermocouple is 14.9 $\mu V \cdot K^{-1}$ and it is known that nickel and gold have an electrical resistivity of 6.03×10^{-8} and 2.44×10^{-8} $\Omega \cdot m$, respectively, and a thermal conductivity of 99 and 318 $W \cdot m^{-1} \cdot K^{-1}$, respectively. Given these parameters, the Z of the thermocouple was determined to be 0.9×10^{-5} K^{-1} which is comparable to the value reported for a microfabricated thermocouple with a 50 – 500 μm^2 sensing area (1.0×10^{-5} K^{-1}) [82]. For further comparison, the Z values for the micropipette thermocouples summarized in Table 3-1 were also calculated using the material properties and Equation 3-5. As seen in Table 3-2, the Z value for the thermocouple fabricated in this work was 207% higher than the next-best performing thermocouple. For reference, the Z of high-performing semiconductor microthermocouples can be as high as 1.8 × 10^{-5} K^{-1} [105].

The time constant, τ_J, of the thermocouple junction, which is indicative of the response time, is calculated as follows:

$$\tau_J = \frac{\rho_J V_J c_{pJ}}{h_{conv} A_J} \qquad 3\text{-}6$$

Where ρ_J is the mass density of the junction, c_J is the specific heat of the junction, V_J *is* the volume of the junction, A_J is the area of the junction, and h_{conv} is the convective heat transfer coefficient at the surface of the junction. To assume a worse-case scenario, the ratio of V_J to A_J was calculated assuming that the gold film completely covered the thermocouple tip (*i.e.* the thermocouple was not hollow) and that the fluid environment is water in the state of natural convection (h_{conv} is ~ 10 $W^{-1}\cdot m\cdot K^{-1}$). Using Equation 3-6 and the material properties of gold, the time constant of the thermocouple is 10 µs.

Table 3-1: Summary of Micropipette-Based Thermoelectric Power.

Authors	Year	Material A	Material B	Thermoelectric Power [$\mu V \cdot K^{-1}$]		Tip Diameter	Solid (S) or Hollow (H)
				Predicted	Measured		
Fish et al.	1995	Platinum	Gold	5.83	7	50 nm	S
Kakuta et al.	2001	Platinum	Gold	5.83	2.1	>1 μm	H
Shrestha et al.	2011	Tin	Nickel	17.5	8.46 - 8.86	2 -30 μm	S
Zhang et al.	2014	Platinum	Platinum-Rhodium	4.93		20 μm	S
This Work	2020	Gold	Nickel	19.79	14.9	475 nm	H

Table 3-2: Summary of Figure of Merit, Z, for Micropipette-Based Thermocouples.

Authors	Year	α [$\mu V \cdot K^{-1}$]	Material A			Material B			Z [K^{-1}]
			Material	ρ [$\Omega \cdot m$]	κ [$W \cdot m^{-1} \cdot K^{-1}$]	Material	ρ [$\Omega \cdot m$]	κ [$W \cdot m^{-1} \cdot K^{-1}$]	
Fish et al.	1995	7	Platinum	1.06×10^{-7}	71.6	Gold	2.44×10^{-8}	314	0.16×10^{-5}
Kakuta et al.	2001	2.1	Platinum	1.06×10^{-7}	71.6	Gold	2.44×10^{-8}	314	0.01×10^{-5}
Shrestha et al.	2011	8.86	Tin	1.10×10^{-7}	62.1	Nickel	6.03×10^{-8}	99	0.28×10^{-5}
This Work	2020	14.9	Gold	2.44×10^{-8}	314	Nickel	6.03×10^{-8}	99	0.86×10^{-5}

3.4. CONCLUSIONS

In this Chapter the development of a novel carbon-based, thermocouple was described. Nickel and gold films were deposited on the micropipette to enable temperature sensing in aqueous environments. The manufacturing process and material selection resulted in a thermocouple with an improved performance over other thermocouples with larger tips. The thermocouple was shown to have an 68% increase in thermoelectric power and 207% increase in the Ioffe criteria relative to other micropipette-based thermocouples while maintaining a sub-500 nm tip size. The ultramicro-thermocouple was designed to readily interface with standard laboratory equipment due to its direct integration into a macroscale quartz capillary. This sensor has the potential to become a widely available tool for the thermal characterization of microenvironments.

Chapter 4

4. DESIGN AND FABRICATION OF AN ELECTROCHEMICAL NANOSENSOR

The development, fabrication, and characterization of a novel two-electrode nanosensor contained within the tip of a needle-like probe is described below. This sensor consists of two, vertically aligned, carbon structures which function as individual electrodes. One of the carbon structures was modified by silver electrodeposition and chlorination to enable it to function as a pseudo-reference electrode. Performance of this pseudo-reference electrode was found to be comparable to that of commercially available Ag/AgCl reference electrodes. The unmodified carbon structure was employed as a working electrode versus the silver-plated carbon structure to form a two-electrode sensor capable of characterizing redox-active analytes. The nanosensor was demonstrated to be capable of electrochemically characterizing the redox behavior of *para*-aminophenol (PAP) in both bulk solutions and microenvironments. PAP was also measured in cell lysate to show that the nanosensor can detect small concentrations of analyte in heterogenous environments. As the working and reference electrodes are contained within a single nanoprobe, there was no requirement to position external electrodes within the electrochemical cell enabling analysis within very small domains. Due to the low-cost manufacturing process, described in Figure 4-1, this nanoprobe has the potential to become a unique and widely accessible tool for the electrochemical characterization of microenvironments.

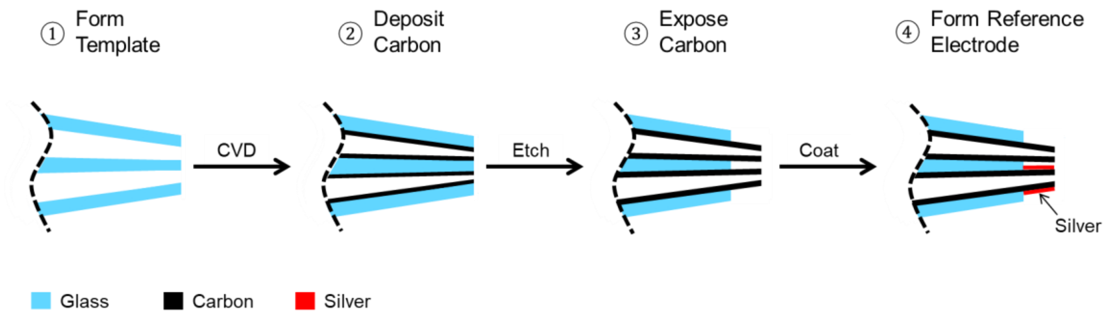

Figure 4-1: Schematic of the steps involved in the nanoelectrode manufacturing process.
(1) a template is formed by drawing a quartz theta capillary into a nanopipette, (2) a thin layer of carbon is deposited within the template using chemical vapor deposition, (3) the quartz template is selectively removed at the tip of the nanoprobe using wet-etching techniques (4) a layer of silver is electrodeposited onto one of the carbon electrodes.

4.1. BACKGROUND

4.1.1. Development of Ultramicroelectrodes

Ultramicroelectrodes have emerged as promising tools for the electrochemical investigation of small domain systems including individual cells. Nanoelectrodes offer several advantages over traditional macro- and microscale electrodes the most obvious of which is a high spatial resolution and the ability to interrogate extremely small spaces which were previously inaccessible due to large electrode sizes. This ability to manipulate and position electrodes in confined spaces enables highly localized sensing. Further, electrodes are only capable of sensing species within their diffusion layer which decreases linearly with electrode size [106]. The miniaturized diffusion layer associated with nanoelectrodes ensures measurements with high spatial resolution.

The reduced electrode area results in a relatively large electrical double layer capacitance and a small resistor-capacitor time constant, indicative of a quickly charging capacitor [107]. As such, it is possible to perform voltammetric measurements at a megavolt per second rate permitting ultrafast analysis. Further, ultramicroelectrodes express a minimal voltage drop, also known as an *iR* drop, and thus can be used to perform electrochemical analysis in solutions with high electrical resistance such as those containing little or no added supporting electrolyte. This is advantageous in physiological environments where it is potentially harmful to add supporting electrolytes.

The most common ultramicroelectrodes fabrication methods include glass-sealed metal nanoelectrodes, mass-produced nanoelectrodes, and carbon filled nanopipettes [66,108–111]. Carbon filled nanopipettes rely upon an amorphous carbon tip which is flexible yet strong.

Carbon-based nanopipettes were fabricated using a template-based CVD manufacturing protocol which produces integrated carbon structures [34]. These carbon nanopipettes were demonstrated as useful tools for intracellular delivery and electrochemical sensors [66,112,113]. A pyrolytic method of producing carbon nanopipettes was developed which relied on the decomposition of a carbon-based gas such as methane or butane [114,115]. Although this method was unique in that it allowed for the selective deposition of carbon in an individual barrel of a multi-barrel probe it did not permit for high-throughput manufacturing of the devices as only a single device can be produced at a time.

4.1.2. Electrochemical Detection in Microenvironments

Micro- and nanoscale electrodes have been an area of active research interest due to their ability to investigate microenvironments and provide insight into both fundamental and applied science including single-cell physiology, single-molecule and particle detection, reaction kinetics, electrical double layer effects, and high-resolution imaging [3,113,116–118]. Microdroplets are used to mimic small-volume environments such as those found in biological research and portable devices or in the pursuit of "green" analytical chemistry which aims to minimize the economic and ecological costs of research by reducing the amount of expensive reagents required and waste produced [47]. Prior to advancements in micro- and nanofabrication processes, droplets would be deposited on the surface of the working electrode with a reference electrode positioned within the droplet, limiting the applicability and spatial resolution of such systems [119,120].

As manufacturing techniques advanced and electrode size reduced, needle-like working electrodes could be positioned within microdroplets, ranging from pico- to micro- liter volumes [47,121,122]. Insulated scanning tunneling microscope tips and fibers with sharp tips down to 50 nm in diameter were employed as working electrodes in small domains including individual cells [123,124]. Metallic sputter-deposited nanopipettes and optical fibers were reported as electrodes for scanning electrochemical imaging [125,126]. Concurrently, metals fused in quartz nanopipettes, with tip diameters approaching 1 nm, were being employed as small-scale electrodes [127,128]. This fabrication method led to the development of dual-electrode systems formed by encasing two 200 nm platinum wires within micrometer-sized pipette tips [129]. Additional nanoelectrode fabrication methods include attaching a single carbon nanotube or metal nanowire to a macroscopic structure for use in microdroplets and individual cells [115,121,130]. These manufacturing methods produce single working electrodes and required the use of external liquid junction reference electrodes or pseudo-reference electrodes, which ultimately increased the overall footprint of the electrochemical cell.

Electrode systems consisting of working and reference electrodes contained within a single tip emerged as convenient tools for performing electrochemical analysis in droplets but had relatively large tip dimensions of tens of µm to 1 mm [131,132]. Multifunctional nanoprobes developed for scanning electrochemical microscopy, with liquid junction working and reference electrodes contained within a single 200 nm to 1 µm tip emerged as tools for high-resolution imaging [52,114]. While these tools worked well for imaging, they rely on the use of aqueous electrolyte filled barrels, which presents integration challenges for point-of-care or consumable sensing device applications. Further, aqueous electrolyte-based sensor systems inhibit interfacing with non-aqueous environments which have sparked recent interest as solvents due to their ability to enhance enzyme stability and activity as well as the facilitating enzymatic catalysis of water sensitive reactions [133].

Changes in the voltammetric and amperometirc behavior of microelectrodes have been demonstrated as the electrochemical environment was reduced from micro- and nano- to picoliter volumes [122]. Thus, it is crucial to perform calibration experiments in environments with similar volumes to that of the intended domain as results obtained in bulk volumes will not mimic those obtained in the small volumes found in many physical and biological applications.

Typically, either microfabricated electrochemical cells or microdroplets are used to mimic the small-volume biological environments for initial electrochemical characterization of an electrode [121,122,132,134–136]. These droplet-based methods allow for electrodes to be positioned within the small volume cell while avoiding complicated microfabrication processes. Prior to the reduction of electrode size, the droplet would be deposited on the surface of the WE [119,120]. As manufacturing techniques advanced and electrode size reduced, needle-like working electrodes could be positioned within the microdroplets [121,122,131,132,137]. The relatively large size of traditional liquid junction REs, such as saturated calomel electrodes, prohibit their use in the study of microenvironments. Thus, pseudo-reference electrodes (including Ag, Ag/AgCl, and Pt wires) are often employed as they can be positioned within the droplet.

A self-contained, solid two-electrode system has not yet been reported in the literature. To produce a working and reference electrode contained within a single nanoscopic tip, we developed, fabricated, and characterized a fine-tipped dual-electrode system that relies on a carbon-based working electrode and silver-plated carbon pseudo-reference electrode. To promote scalability and thus widespread accessibility of the technology, template-based nanomanufacturing methods were employed [34,49,138–140], along with a novel method of forming a reference electrode. Carbon nanostructures were formed at the tips of pulled glass capillaries and exposed via wet etching to form nanoscale electrodes. One electrode was coated with silver using electrodeposition to form a pseudo-reference electrode. The nanoscale tip was directly integrated into a 1 mm diameter structure to allow for convenient handling and interfacing with standard laboratory equipment. The manufacturing process is low-cost and high-throughput with the potential for large-scale production, enabling future wide-spread utilization of the technology. The fabrication of the nanoprobe is completed entirely outside of a clean room, resulting in a highly accessible tool. The reported manufacturing procedure resulted in a structure with a fine, yet robust tip capable of withstanding modification and electrochemical characterization.

4.1.3. Electrochemical Detection of *Para*-Aminophenol

The utility of the novel two-electrode nanosensor was demonstrated using *para*-aminophenol (PAP). PAP has relevance in several areas of industry and research and has been found in the pharmaceutical preparation of the antipyretic and analgesic paracetamol [141]. As PAP is associated with nephrotoxic and teratogenic effects, the United States and Europe have placed limits on the concentration of PAP contamination in pharmaceutical acetaminophen [142,143]. PAP is also used in the production of commercial dyes, as a photographic developer, and a petroleum additive. The wide-spread use of PAP in industrial applications resulted in a high risk of it being released into the environment as a pollutant, motivating researchers to develop PAP sensors [144,145]. Further, PAP has been determined to have biological significance as it is the product formed when β-galactosidase hydrolyzes p-aminophenyl galactopyranoside (PAPG). PAP has been widely used as a marker of β-galactosidase for the detection of senescent cells, anti-HIV antibodies, and bacterial contamination in water and dairy samples [146–149]. The widespread significance of PAP necessitates the development of a simple analytical method of detecting PAP.

Previous works focused on characterizing the redox behavior of PAP have studied single concentrations of 1 mM and 0.5 mM or considered a range of concentrations from 0 - 550 µM [67,150,151]. Here, the lower range of PAP concentrations was investigated in small increments to demonstrate the improved sensitivity and resolution of the electrode system. In this work, the electrodes ability to detect PAP in bulk solution as well as in 50 nL aqueous droplets was investigated. The probe was capable of measuring PAP concentrations in the range of 10 – 50 µM with a response comparable to that of the probe's carbon nanoelectrode versus a larger commercially available reference electrode. This work demonstrates a low-cost, high-throughput method of forming two working electrodes in very close proximity, a method of modifying nanoscale electrodes to form nanoscale pseudo-reference electrodes, and a self-contained, solid two-electrode nanosensor for electrochemical analysis in aqueous microenvironments.

4.1.4. Electrochemical Detection of β-Galactosidase

β-galactosidase (β-gal), an enzyme that catalyzes the hydrolysis of β-galactoside into monosaccharides, has served as an indicator for the detection of *Escherichia coli* in clinical, food, dairy, and water samples, and anti-HIV antibodies in serum [147,148,152–155]. Electrochemical detection methods must rely on indirect measurements of β-gal as the enzyme is not electrochemically active. The oxidation of p-aminophenol (PAP), a product of the catalytic reaction of β-gal and p-aminophenyl β-D-galactopyranoside (PAPG), has been used to indirectly detect the presence of β-gal [156]. The utility of electrochemical techniques lies in the capability to detect β-Gal activity in real-time.

Initial attempts of electrochemically monitoring β-Gal activity began in the 1990s and utilized amperometric detection techniques. As previously described, β-Gal is not electrochemically active and thus requires the use of a substrate for detection. *p*-Aminophenyl-β-ᴅ-galactopyranoside (PAPG) was identified as a suitable substrate as it undergoes an enzymatic reaction in the presence of β-Gal to produce *p*-aminophenol (PAP). *p*-Aminophenol was detectable at 200 mV vs Ag/AgCl with a 50 nM detection limit using a glassy carbon working electrode in a pH 7 phosphate buffer [157]. A peak separation of 92 mV was found indicating a fully reversible, two-electron transfer reaction.

Scanning electrochemical microscopy was utilized to characterize the activity of β-Gal from *Escherichia coli* [158]. Again, PAPG was utilized as a substrate with a platinum ultramicroelectrode working electrode in a pH 7 phosphate buffer. The reversible oxidation peak of PAP was identified at 190 mV vs 3M Ag/AgCl at a scan rate of 100 $mV \cdot s^{-1}$. An irreversible oxidation peak of PAPG was identified at approximately 590 mV. This high, relative to that of PAP, oxidation peak occurs as the reaction involves the energy-consuming process of breaking a strong ether bond. By scanning only to a maximum of 400 mV vs 3M Ag/AgCl, the oxidation of PAP can be identified without interference from PAPG.

The electrochemical characterization of β-Gal activity was compared to the traditional fluorometric Miller assay in *Escherichia coli* [159]. The amperometrically generated signal from the enzymatic β-Gal and PAPG reaction was compared to that of PAP to estimate the concentration of enzyme within live cells. The developed correlations between electrochemical measurements and Miller Units enabled the prediction of one response from the other. While the Miller assay is limited to use in lysed cells, the electrochemical detection of β-Gal can be performed in both lysed and whole cells. Further, electrochemical characterization provides more rapid responses using simpler techniques.

4.2. METHODOLOGY

4.2.1. Electrode Fabrication

The carbon-based nanoprobe is manufactured in three main processing procedures: (i) Fabricate a carbon-based nanopipette with two independent carbon pipes contained within a single nanoscopic tip as described in Section 2.2; (ii) Establish a connection between the carbon film at the microscale ends of the probe to enable direct interfacing with standard electrochemical equipment; and (iii) Coat one of the carbon nanopipes with Ag/AgCl to serve as a RE.

Establishing an Electrical Connection to the Carbon Film

Electrical connections to the carbon tips were established by inserting a tin-coated copper wire into each lumen at the distal end of the pipette. To reduce contact resistance between the wire and carbon coating the lumen, the wire was coated with two-part silver paint (Electron Microscopy Sciences). Each wire was then adhered to the distal end of the pipette with dielectric wax (Apiezon, Wax W), with care taken to avoid contact of the two individual wires. The continuous carbon coating electrically connected the point-of-contact of the wire with the exposed nanostructures at the tip of the pipette. It was noted that the CVD process resulted in a layer of carbon on the exterior of the probe that led to extraneous signals during electrochemical experiments. Thus, a fine-grit sandpaper was used to mechanically disconnect the layer, rendering it inert.

Formation of a Reference Electrode

To produce a nanoprobe capable of performing electrochemical measurements, one of the carbon tips was modified to serve as a reference electrode while the other remained unmodified to serve as a working electrode. One of the two carbon electrodes was coated with silver via electrodeposition and then chlorinated to form a pseudo-Ag/AgCl reference electrode. Electrodeposition is the process of depositing a thin metallic layer on the surface of an electrode by passing an electric current through an electrolyte containing dissolved metal cations, as depicted in Figure 4-2. Faraday's law of electrolysis was utilized to determine the current required to deposit a thin layer of silver onto one of the carbon barrels:

$$m = \frac{QM}{\mathrm{F}z} \qquad \text{4-1}$$

where m is the mass of substance, Q is the total electric charge passed through the substance, F is Faraday's Constant (96485 $\mathrm{C \cdot mol^{-1}}$), M is the molar mass of the substance (108 $\mathrm{g \cdot mol^{-1}}$), and z is the number of valence ions in the substance (1). The mass of silver deposited on the carbon barrel can be determined as follows:

$$m = \rho A_s l \mu \qquad \text{4-2}$$

Where ρ is the density (10.49 $\mathrm{g \cdot cm^{-3}}$), A_s is the surface area, and d is the thickness of the deposited substance. Further, Q can be expressed as the product of i, the current passed through the electrode, and t, the duration which the current is applied to the electrode. Thus, Faraday's law can be expressed as follows:

$$it = \rho A_s d \frac{\mathrm{F}z}{M} \qquad \text{4-3}$$

Based on micrographs of the barrel, it can be approximated that A_s is 10 μm^2. As it was not yet determined what d would produce a sufficient layer of silver to function as a pseudo-reference electrode while not significantly increasing the diameter of the nanosensor, 5 nm was selected. A Q of 9.4×10^{-10} C was calculated however as it was anticipated that this may underestimate the deposition rate and due to limitations of the potentiostat, a 60 pA current was applied to one of the carbon electrodes for 60s, corresponding to a *Q* of 3.6 × 10^{-9} C.

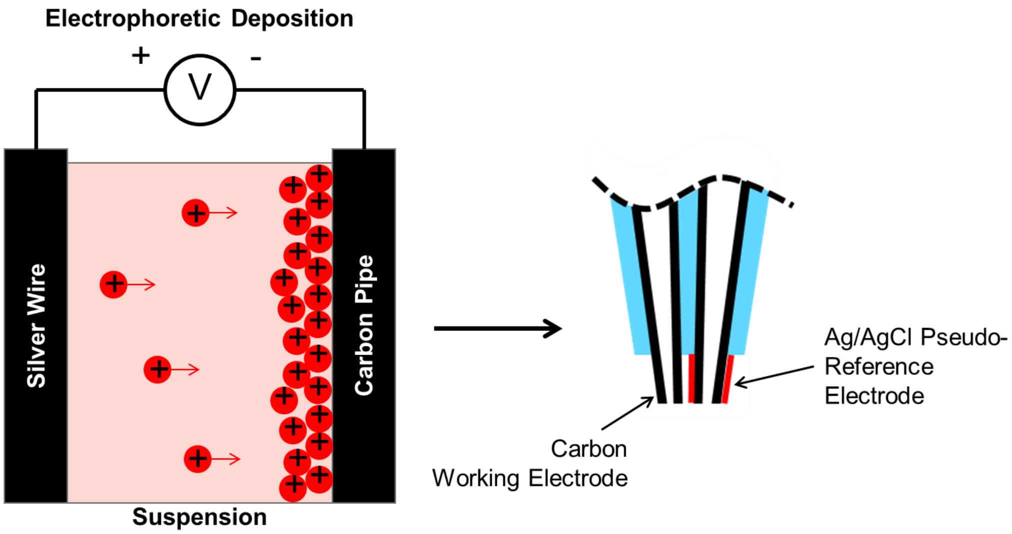

Figure 4-2: Schematic of electrodeposition process.
Electrophoretic deposition of silver onto the surface of one of the carbon pipes to form a chlorinated silver pseudo-reference electrode.

The electrodeposition of silver was isolated to a single nanostructure while the entire pipette tip was immersed in a commercially available standard silver-plating solution (Transene Company Inc.) due to the insulating layer of quartz. A silver wire served as the anode. The silver-coated electrode was chlorinated to form an Ag/AgCl pseudo-reference electrode by bathing in a chlorine-based solution (Liquid Clorox) for a minimum of 15 minutes. The resultant probe consists of distinct working and reference nanoelectrodes protruding from a single sub-500 nm tip to form a two-electrode electrochemical cell localized at the end of a pulled glass capillary.

4.2.2. Electrode Characterization

Fabricated electrodes were visualized by scanning electron microscopy with a Tescan Mira3 Scanning Electron Microscope at 20 keV after sputter coating with gold/palladium (SPI Supplies). Average values of electrode diameter, length, and separation were obtained from these micrographs.

Electrochemical characterization was conducted in phosphate buffered saline (PBS) and cell lysate. PBS was prepared using sodium phosphate dibasic (Fisher Scientific), potassium phosphate monobasic (Sigma-Aldrich) mixed to pH 7.2, 50 mM of phosphate. 100 mM sodium chloride (EMD Chemicals) was added as a supporting electrolyte. A stock solution of 40 mM PAP (Sigma-Aldrich) was prepared daily in PBS at 70 °C. All solutions were sparged with N_2 and care was taken to reduce the amount of light the PAP was exposed to minimize oxidative effects. Human embryonic kidney 293 (HEK-293) whole cell lysate (2×10^6 cells $\cdot$ ml^{-1}) was prepared in PBS without supporting electrolyte or N_2 sparging.

Cyclic voltammograms were obtained for PBS as baseline and concentrations of 10-50 µM PAP using a Gamry Reference 600 (Gamry Instruments) within a Faraday cage. To capture the oxidation peak of PAP at +160 mV and avoid extraneous side reactions, cyclic voltammetry was conducted in the potential range of -100 to 400 mV at a scan rate of 10 mV s^{-1} [157,158]. The potential range was scanned three times at each analyte concentration to ensure stabilization of the system. Standard curves were generated from baseline-subtracted current measurements at 400 mV from the third scan. Electrode capacitance was calculated by dividing the total voltammetric charge by the scan rate [160].

Cyclic voltammograms were obtained for the unmodified carbon pipe (henceforth referred to as CP) versus a commercially available Ag/AgCl reference electrode (CH Instruments, CHI111) in an 80 mL electrochemical cell and for CP versus the electroplated carbon pipe (henceforth referred to as "CP-Ag/AgCl") in an 80 mL electrochemical cell.

The enzymatic β-Gal and PAPG reaction was characterized. Recent electrochemical β-Gal sensors have had sensitivities in the range of $9.4 \times 10^{-5} – 4.7 \times 10^{-1}$ $U \cdot mL^{-1}$ [154,161–163]. For this work, 2.5×10^{-2} $U \cdot mL^{-1}$ β-Gal was characterized with 10 – 50 µM PAPG in 7.2 pH PBS with 100 mM NaCl added as a supporting electrolyte. Voltammograms were collected 5 minutes after adding PAPG to the β-Gal solution to allow the reaction to progress. The PBS solution was exchanged and the electrode was cleaned between each differrent PAPG concentration.

4.2.3. Electrode Characterization in Microenvironments

Optical characterization and monitoring of the droplet electrochemistry experiments were performed using an upright microscope (Zeiss, Axio Scope.A1) and captured with a camera (Zeiss, Axiocam 503, mono) and Zen microscope software. The droplet and nanosensor were positioned in the view field with a manual micromanipulator (World Precision Instruments, Kite Manual Micromanipulator KITE-R).

Microenvironments were prepared by placing 50 nL droplets of varying PAP concentration on the end of a 1 mm diameter solid quartz rod (Sutter Instrument). The carbon nanoprobe was positioned in the droplet using a manual micromanipulator under an optical microscope enclosed in a custom Faraday cage. The probe was rinsed in PBS between each change in concentration. Reagents were prepared and voltammograms were collected as described in Section 4.2.2.

4.3. RESULTS AND DISCUSSION

4.3.1. Single Nanoelectrode Characterization

As a proof of concept, initial experiments were performed using a three-electrode system consisting of a single-barrel sensor (Figure 4-3) as a working electrode, a commercially available reference electrode, and a platinum wire counter electrode in a pH 7.2 phosphate buffer with 100 mM NaCl as a supporting electrolyte. The single barrel electrode was produced as described in Section 2.2 with three minutes of etching to expose the carbon nanoelectrode. The redox conversion of PAP to p-iminoquinone was studied from concentrations 10 – 100 µM. Increases in analyte concentration led to a proportional increase in peak current as seen in Figure 4-4 A. This experiment was repeated with single-barrel sensors produced from different batches. As seen in Figure 4-4 B, a linear relationship was found between the concentration of PAP and the current measured at 400 mV with an average R^2 of 0.99 for three electrodes. These results indicated that it was possible to establish an electrical connection to the nanoscopic carbon electrode.

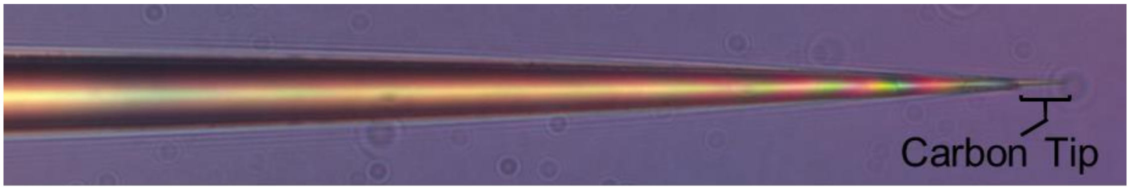

Figure 4-3: Micrograph of single-barrel electrode

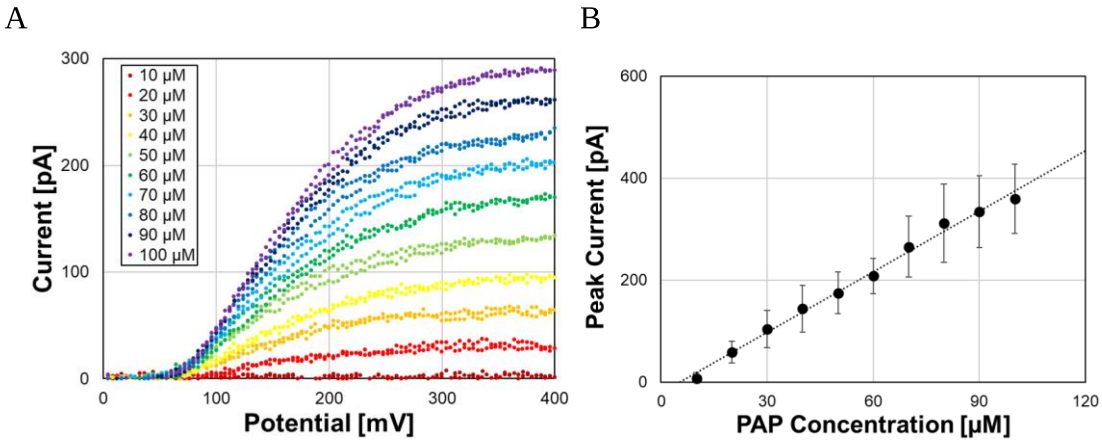

Figure 4-4: Electrochemical characterization of PAP using a single barrel nanosensor WE and a commercially available Ag/AgCl RE. A) Background subtracted response and B) Standard curve of the average electrochemical characterization. Error bars represent the standard deviation for a n of three. Cyclic voltammograms were recorded in a PBS solution containing 100 mM NaCl at a scan rate of 10 mV·s^{-1}.

It is known the PAP will oxidize when exposed to light and oxygen. While care was taken to minimize exposure by sparging all solutions with argon and performing experiments in a dark Faraday cage, some exposure to light and oxygen was inevitable. To quantify these effects, voltammograms were collected every 10 minutes for 130 minutes at 20 µM PAP in PBS with 100 mM NaCl as a supporting electrolyte. As seen in Figure 4-5, degradation of the species, indicated by deviation from the peak current from the initial peak current, was noted at a rate of 0.8% per minute. As a typical set of experiments takes approximately 45 minutes to complete, this corresponds to only a 3.6% loss of signal over the course of the analysis.

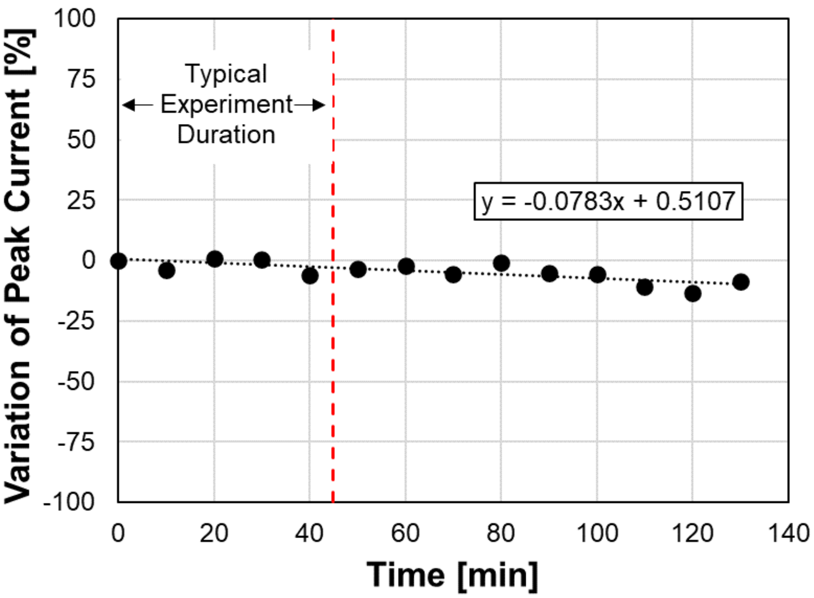

Figure 4-5: Degradation of PAP over time.
Degradation of PAP due to oxidative effects of light and oxygen. Cyclic voltammograms were recorded in a PBS solution containing 100 mM NaCl at a scan rate of 10 mV·s^{-1}.

4.3.2. Characterization of Reference Electrode Performance

As seen in the X-ray photoelectron spectroscopy (XPS) spectra shown Figure 4-6, a silver peak was identified in samples after the electrodeposition process but not before, indicating that a silver layer was formed on one of the CNPs. To investigate the ability to manufacture a pseudo-reference electrode by electroplating and chlorinating a single barrel electrode, again a three-electrode electrochemical cell was used to characterize the PAP-p-iminoquinone redox couple. A commercially available glassy carbon electrode (CH Instruments CHI111) was used as a working electrode, an electroplated single-barrel probe was used as a reference electrode, and a platinum wire was used as a counter electrode in a pH 7.2 PBS with 100 mM of NaCl as a supporting electrolyte. The results of this measurement were compared to those obtained using a commercially available

Ag/AgCl reference electrode and an uncoated single barrel. As seen in Figure 4-7, the results obtained with the electroplated single and commercially available Ag/AgCl reference electrode were consistent while the uncoated single was unable to serve as a stable reference electrode. This indicates that the electroplating processes enables the probe to function as a RE and not some other intrinsic property of the single-barrel probes.

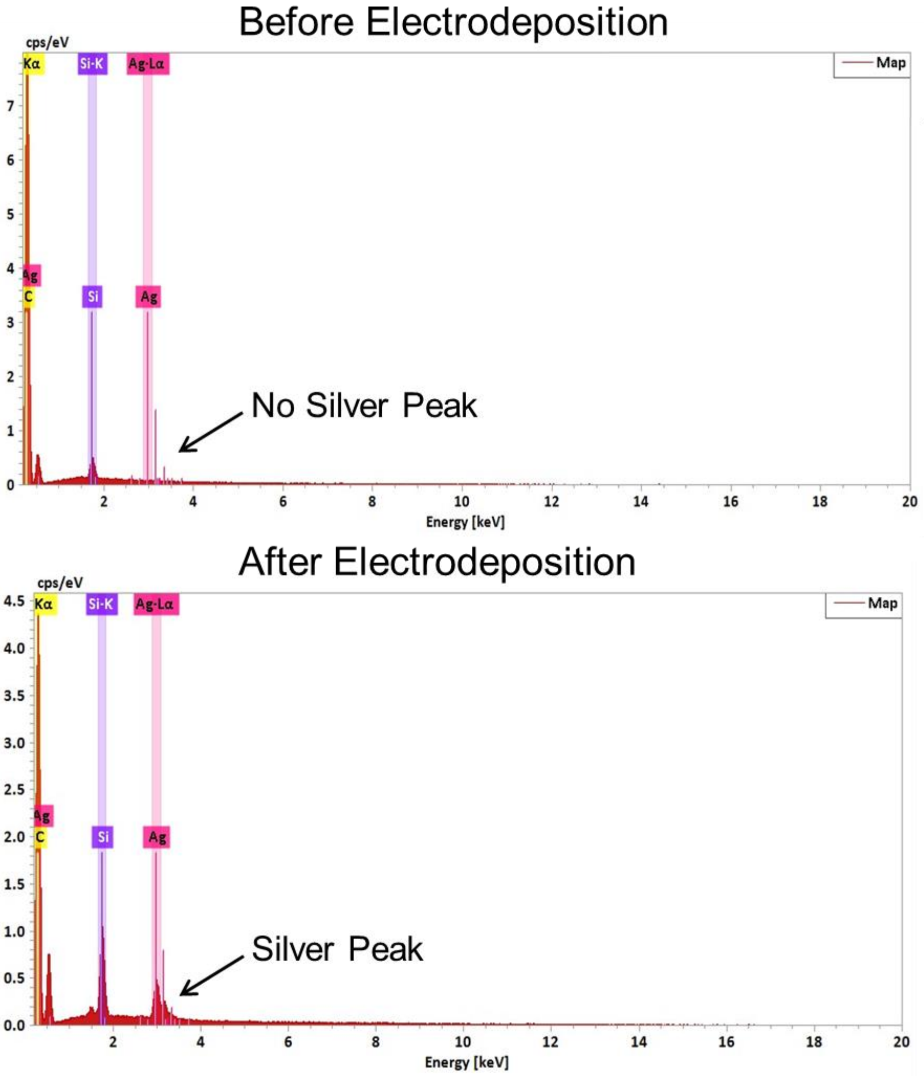
Before Electrodeposition

After Electrodeposition

Figure 4-6: XPS spectra of samples before and after silver electrodeposition.

A two-electrode cell consisting of a nanoprobe WE and electroplated nanoprobe RE was used to characterize the redox reaction of PAP. Again, the analysis was performed in pH 7.2 PBS with 100 mM NaCl as a supporting electrolyte. Concentrations of PAP ranging from 0 to 50 µM were characterized, as seen in Figure 4-8. As seen in Figure 4-9, the standard curve with this two-electrode cell was similar to that obtained when using a three-electrode cell with a commercially available RE and counter electrode. The peak current increased linearly with concentration of PAP with an R^2 value of 0.98. These results indicated that it was possible to convert a nanoscale carbon electrode to a stable chlorinated silver pseudo-reference electrode that would perform comparably to commercially available Ag/AgCl electrode.

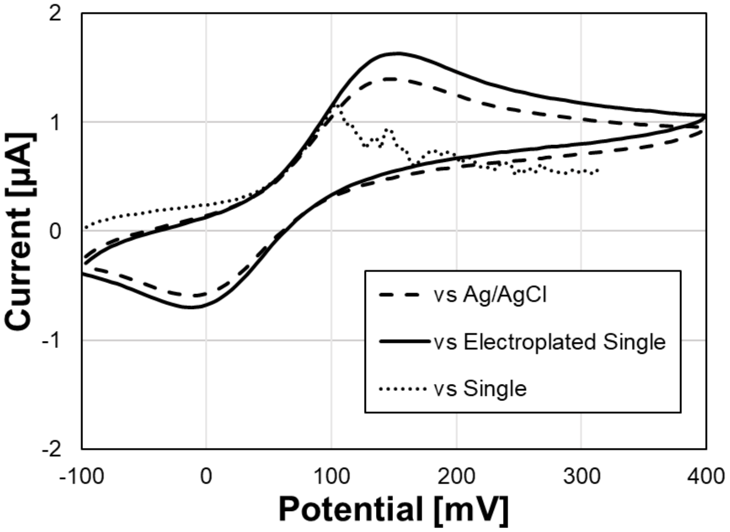

Figure 4-7: IV curve of the electrochemical characterization of PAP for three scenarios:
i) glassy carbon WE vs a commercially available Ag/AgCl RE, ii) glassy carbon WE vs an electroplated single barrel nanosensor, and iii) glassy carbon WE vs a single barrel nanosensor. Cyclic voltammograms were recorded in a PBS solution with 100 mM NaCl at a scan rate of 10 $mV \cdot s^{-1}$.

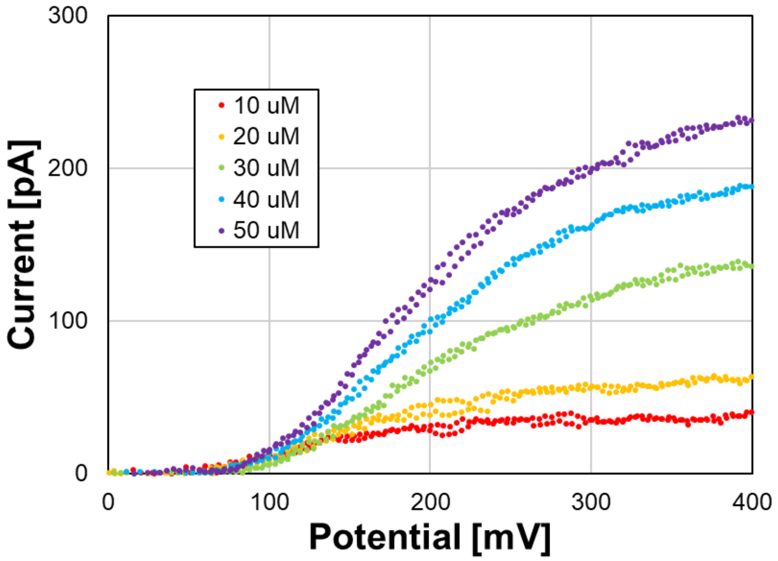

Figure 4-8: IV curve of the electrochemical characterization of PAP utilizing a single barrel nanosensor WE vs an electroplated single barrel nanosensor RE.
Cyclic voltammograms were recorded in a PBS solution containing 100 mM NaCl at a scan rate of 10 mV·s^{-1}.

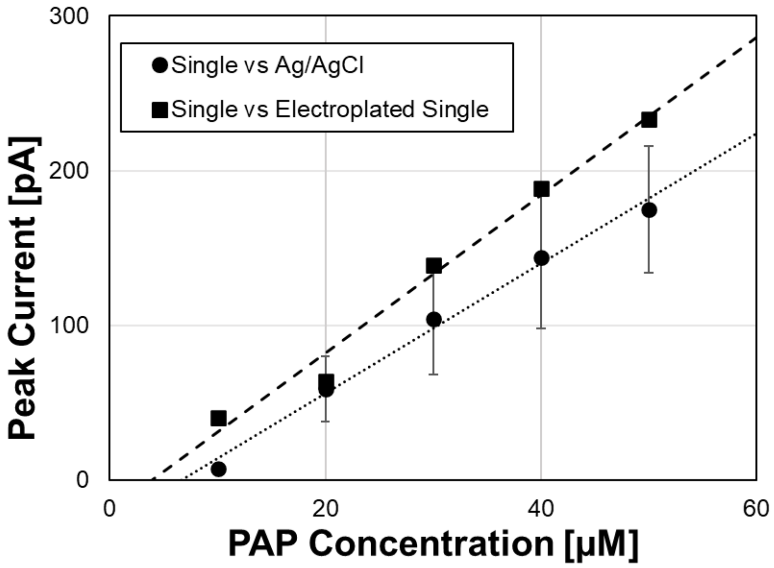

Figure 4-9: Standard curve of a single barrel electrode versus an electroplated single barrel electrode compared to the average response when using a commercially available Ag/AgCl RE.
Cyclic voltammograms were recorded in a PBS solution containing 100 mM NaCl at a scan rate of 10 mV·s^{-1}.

4.3.3. Characterization of Independent Electrode Performance

The needle-like probe, shown in Figure 4-10, consists of two independent nanoelectrodes within a nanoscopic tip as described in Section 2.2. The electrical connections and insulation of each barrel, prior to modification by electroplating, was initially tested by cyclic voltammetry in bulk solutions. Each barrel was independently utilized as a working electrode versus a commercially available Ag/AgCl reference electrode (CH Instruments). The redox potential of PAP was studied in concentrations of 10 – 50 µM. Figure 4-11 shows the typical relationship between the concentration of analyte and the peak current obtained upon stabilization of the voltammogram. A linear model of the form $y(x) = m \cdot x + b$ was fit to this data. The response of each electrode was similar with slopes of approximately 2 and 2.5 pA/µM and R^2 values of 0.97 and 0.99 for CP and CP-Ag/AgCl respectively, indicating that the two working electrodes had similar electrochemically active areas. While Figure 4-11 shows the typical response of the electrodes, five additional electrodes were characterized and the resulting average and standard deviation of the limit of detection (LOD), R^2, slope, and capacitance are reported in Table 4-1. The LOD was calculated using the established formula LOD=3σ/*m* where σ is the standard error of the ordinate intercept and m is the slope of the linear model [164]. The average background current of the six electrodes was 6 pA.

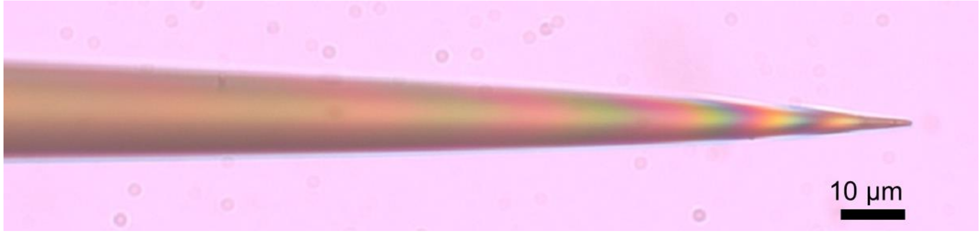

Figure 4-10: Optical micrograph of electrochemical sensor.

Micrographs were analyzed to determine the average individual electrode diameter (*d*), length (*L*), and electrode separation (*S*) by measuring these parameters to the nearest 5 nm. For a sample size of six, average dimensions of *w* = 113 ± 50 nm, *L* = 194 ± 112 nm, and *S* = 43 ± 3 nm were measured.

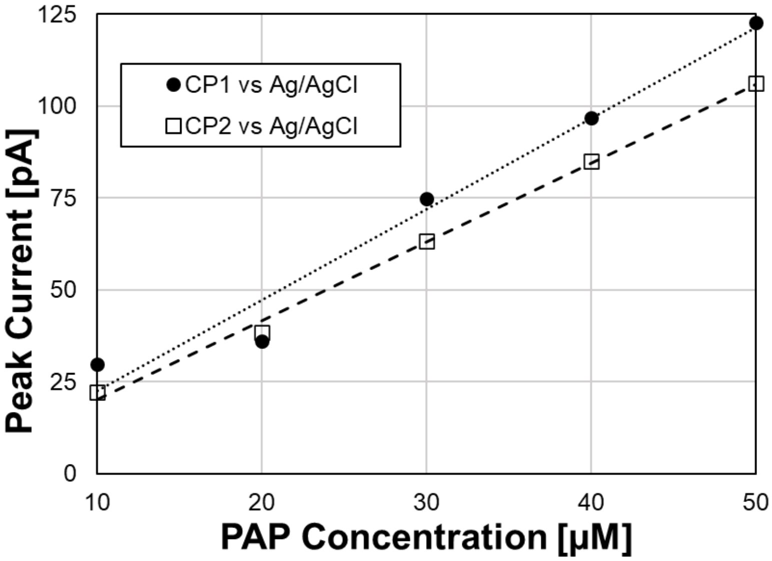

Figure 4-11: Electrochemical characterization of individual carbon electrodes.
Voltammetric response of each carbon tip, prior to modification, versus a commercially available Ag/AgCl reference electrode in a PBS solution containing 100 mM NaCl and 0 – 50 µM PAP at a scan rate of 10 $mV \cdot s^{-1}$.

The results of this electrochemical characterization and subsequent analysis indicated that there were two electrically independent nanoelectrodes contained within a single nanoscopic tip capable of detecting small concentrations of redox species. These results were significant as they demonstrate that two independent nanoelectrodes exist within a nanoscale footprint which can be used individually for analyte sensing and duplicity. As the electrodes function independently, they can be individually functionalized and addressed for multi-analyte sensing. Further, these results indicate that a single electrode can be modified to serve as a reference electrode resulting in an all-in-one electrochemical sensor.

Table 4-1: Average behavior of nanosensors in various experimental configurations.

	CP vs Ag/AgCl	CP vs CP-Ag/AgCl	CP vs CP-Ag/AgCl
n	6	6	3
Environment	PBS + NaCl	PBS + NaCl	PBS + Cell Lysate
LOD [µM]	8.6 ± 5.0	12.6 ± 5.3	12.4 ± 2.8
R^2	0.97	0.95	0.97
Current at 50 µM [pA]	108.4 ± 43.4	67.4 ± 13.5	16.6 ± 2.2
Slope [pA·μM^{-1}]	2.1	1.6	0.4
Capacitance [nF]	0.6 ± 0.3	1.0 ± 0.8	0.4 ± 0.1

4.3.4. Characterization of Self-Contained Electrochemical Nanosensor Performance

Silver electrodeposition and chlorination of one of the carbon electrodes enabled it to serve as a pseudo-reference electrode in a two-electrode electrochemical cell. The resulting nanosensor is shown in the SEM micrograph in Figure 4-12. As seen in Figure 4-13, cyclic voltammograms were obtained before and after electroplating the probe to demonstrate that the silver-coating was enabling CP-Ag/AgCl to function as a reference electrode. Prior to electroplating (Figure 4-13 A), CP versus CP-Ag/AgCl was unable to detect changes in PAP concentration. Upon electroplating and chlorinating CP-Ag/AgCl

(Figure 4-13 B), the two-electrode system was able to detect changes in PAP concentration. The voltammetric response of CP versus CP-Ag/AgCl was comparable to results obtained from CP versus a commercially available Ag/AgCl reference electrode. Figure 4-14 shows the average response of each scenario for six different nanosensors. The average LOD, R^2, slope, and capacitance are reported in Table 4-1. The average background current of six nanosensors was 32 pA.

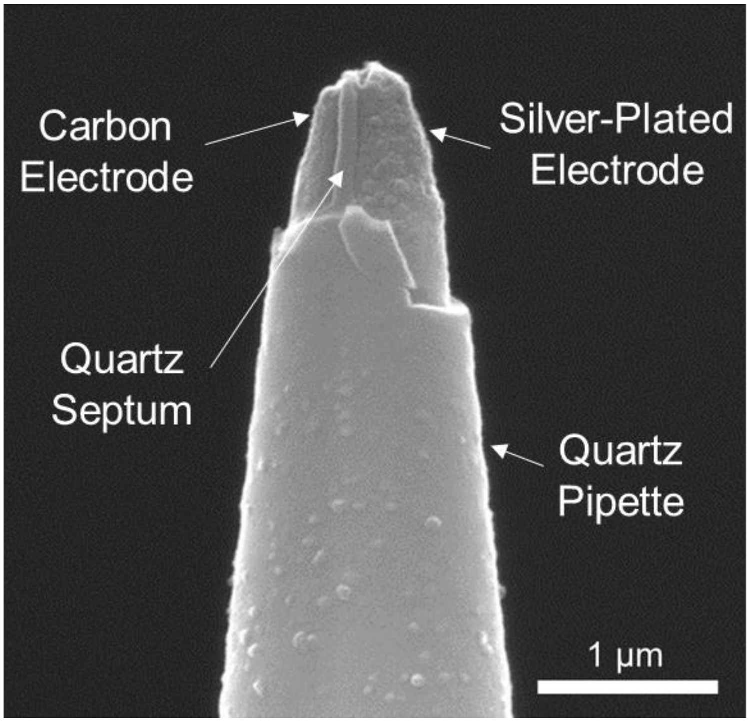

Figure 4-12: SEM micrograph of the tip of the fabricated electrode system.

As shown in Figure 4-13 A, when one unmodified electrode was used as a working electrode and the other unmodified barrel as a reference electrode in a two-electrode configuration, the average current at 400 mV and 50 μM PAP deviated 4 pA from the baseline and fell within the noise of the current indicating that the two-carbon electrode configuration was unable to detect changes in PAP concentration. However, when used in the CP vs Cp-Ag/AgCl configuration, a linear increase of current with respect to PAP concentration was observed with an average slope of approximately 1.6 pA per µM and an R^2 value of 0.95 for six different electrodes, indicating that the electrode was functional and able to detect changes in PAP concentration. It was therefore concluded that the unmodified probe was not capable of serving as a reference electrode and that the change in electrode behavior was a result of the electroplating process. These results demonstrate that a stable pseudo-reference electrode with performance similar to large commercially available reference electrodes can be formed at the nanoscale tip of a nanoprobe.

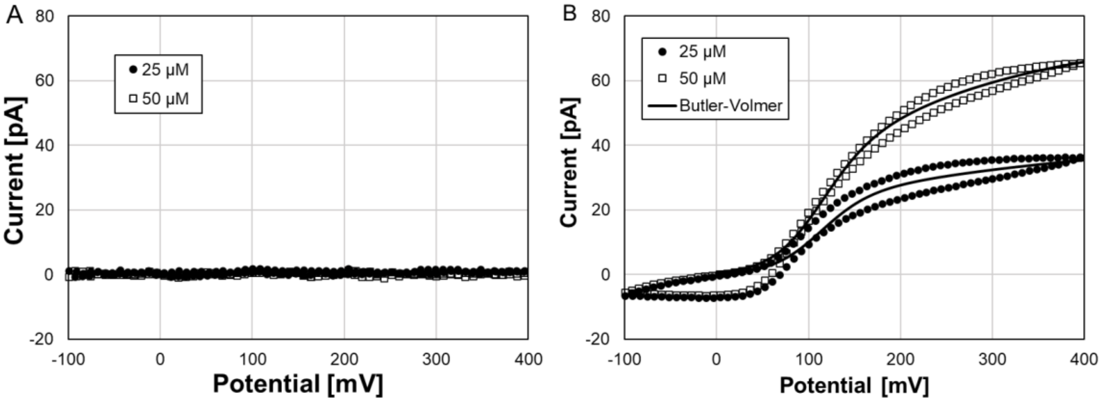

Figure 4-13: Electrochemical characterization of the two-electrode nanoprobe.
Voltammetric response of one carbon pipe versus the second (A) before and (B) after modifying the second to serve as a reference electrode by electrodepositing silver on the carbon surface. Data has been down sampled at a 1:2 ratio. The solid line in B shows the Butler-Volmer model curve fit to the 25 and 50 µM PAP data. Cyclic voltammograms were recorded in a PBS solution containing 100 mM NaCl at a scan rate of 10 mV·s^{-1}.

The nanosensor's voltammetric response is quasi-steady state as predicted by theoretical models for cylindrical ultramicroelectrodes [165] and is similar to experimental voltammetric responses of ultramicroelectrodes reported by others [121,128,166,167]. The voltammetric response of nanoelectrodes has been described using the Butler-Volmer model which incorporates the electrode kinetics and diffusive mass transport to predict the current (i) at a given applied potential (E) [121,160,168]:

$$i = \frac{i_d}{1 + e^{\pm F(E-E^{0'})/RT} + K_0^{-1} e^{\pm F\beta(E-E^{0'})/RT}} \qquad \text{4-4}$$

where F and R are the Faraday and molar gas constant, respectively, and T is the absolute temperature. When used to represent oxidation, the negative sign and $\beta = (1 - \alpha)$ are used where α is the charge transfer coefficient. This dimensionless variable signifies the fraction of the potential at the electrode-electrolyte interface that lowers the free energy barrier of the electrochemical reaction. Equation 1 was fit to experimental voltammograms using the nonlinear least-squares fitting procedure to determine the diffusion limited current (i_d), the formal potential ($E^{0'}$), the heterogeneous electron transfer rate constant (K_0), and α. Equation 4-4 was fit to the experimental voltammograms in Figure 4-13 and the resulting parameters are shown in Table 4-2. The $E^{0'}$ and α were found to be statistically equivalent for both the 25 and 50 µM PAP voltammograms. As expected, the K_0 varied between the two curve fits as it is dependent on the analyte concentration. The K_0 provides information on the electrode performance by indicating the rate of electron transfer between the electrochemically active species and the electrode surface.

Table 4-2: Butler-Volmer curve fit parameters the equivalent electrode radius.

PAP Concentration [μM]	E'_0 [mV]	K_0	i_d [pA]	α	R^2	r [μm]
25	112.5 ± 13.7	1.48 ± 1.04	42 ± 16	0.88 ± 0.15	0.98	1.07
50	112.5 ± 02.2	1.21 ± 0.13	73 ± 06	0.82 ± 0.06	0.99	1.86

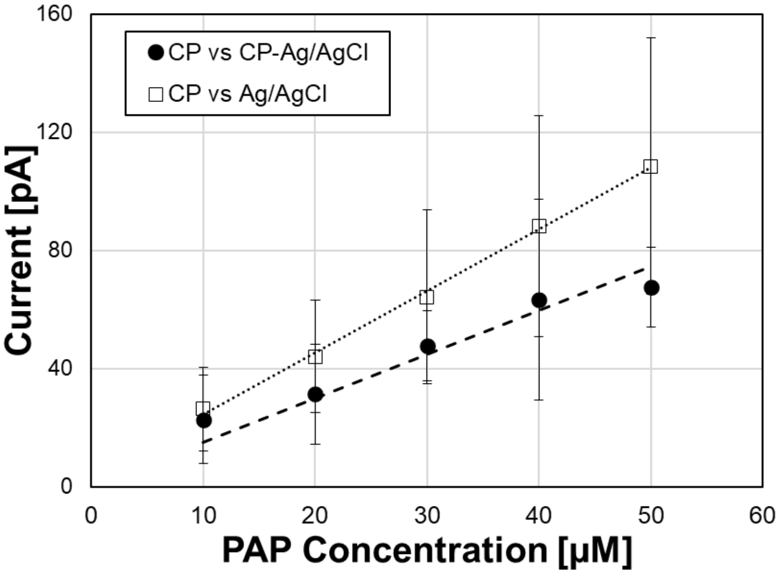

Figure 4-14: Comparison of fabricated reference electrode and commercially available reference electrode average voltammetric response.
Each case represents a sample size of 6 nanosensors.

The voltammetric responses of ultramicro- and nanoelectrodes can be further described using a variant of the Cottrell equation. Ultramicroelectrodes have traditionally been modeled as hemispherical electrodes at steady state [116,121,141,160]. The relationship between the diffusion limited current can be estimated as follows:

$$i_d = 2\pi nFDCr \tag{4-5}$$

where n is the number of electrons transferred during the redox reaction (2 electrons for the redox of PAP), D is the diffusion coefficient of the redox species (6.47×10^{-6} cm^2 s^{-1} for PAP [169]), C is the bulk concentration of redox species, and r is the electrode radius. From Figure 4-12, we approximated each electrode as a hemisphere with $r = 0.5$ µm, corresponding to the diameter of the electrode at its axial middle. Using i_d determined above, it was calculated that the average corresponding r of the electrode is 1.47 µm, which is larger than the value of r measured from micrographs of the electrode.

There are several possible causes for this discrepancy including an underestimation of the electrochemically active area due to surface roughness of the electrode as seen in Figure 4-12. Relative to a realistic convective transport scenario, an assumption of purely diffusive transport would result in an underestimation of the expected current [141]. Small-scale vibrations of the nanosensor could lead to convective disruption of the diffusion layer surrounding the electrode and result in larger currents than those predicted by the Cottrell equation, which assumes purely diffusive transport. Further, it has been proposed that although the Cottrell equation can provide a useful approximation of the relationship between electrochemically active area and current, it does not account for nonequilibrium conditions induced in the electrical double layer by the high flux of charged species [160,169]. The differences of our measured and calculated current are within the magnitude of those previously reported in the literature using the Cottrell equation [121].

The heterogeneous rate constant, k^0, is of particularly use when examining the performance of electrode materials [170]. This constant, which is the dimensionalized form of K_0, indicates the speed of electron transfer between the electrochemically active species and the electrode surface and whether the rate of reaction is determined by the electrode material [170,171]. In general, a higher k^0 indicates a better performing electrode. The k^0 of a given system depends both on the analyte and electrode material and dimensions. The following equation is used to described k^0 for an electrode:

$$k^0 = \frac{K_0 i_d}{FAC} \tag{4-6}$$

Thus, Equation 4-6 can be used to dimensionalize K_0 determined above. The results for this work and other works described in the literature are presented in Table 4-3. In this work, a k^0 330% higher than the next best performing electrode was achieved, indicating that the self-contained electrochemical sensor has the capability to function as a high-performance electrode [172,173]. The k^0 of when analyzing PAP was only reported for macroscale electrodes and thus the performance of the self-contained electrochemical sensor could not be directly compared to other nanoelectrodes.

Table 4-3: Heterogeneous rate constants for the electrochemical characterization of PAP

Authors	Year	Electrode	[PAP]	k^0 [cm·s^{-1}]
Tohidinia et al.	2020	Graphite Paste Electrode	70 µM	1.49×10^{-3}
Filik et al.	2015	Modified Glassy Carbon	100 µM	2.26×10^{-3}
Tohidinia et al.	2020	Modified Graphite Paste Electrode	70 µM	3.32×10^{-1}
This Work	2020	Amorphous Carbon Nanoelectrode	50 µM	1.43

4.3.5. Characterization of Electrochemical Nanosensor Aging

The effects of repeated use on the electrochemical nanosensor was investigated by characterizing the redox of PAP from 10 - 50 µM three times over the course of three days. As seen in Figure 4-15 A, the response of the electrode varied randomly over the three uses with the maximum standard deviation of 4.2 pA occurring at 10 µM PAP. The average response of the electrode was similar to the average response of six different nanosensors as shown in Figure 4-15 B. These results indicate that short-term aging does not appreciably affect the performance of the nanosensor. In Section 4.3.4 it was determined that the response of the nanosensor was highly linear with an average R^2 of 0.95. Thus, it would be appropriate to perform a two-point calibration prior to using the nanosensor in a sensing application to achieve the most accurate results. The results of this Section indicate that the nanosensor would be able to withstand this additional characterization without negatively affecting the electrodes sensing capabilities in future tests.

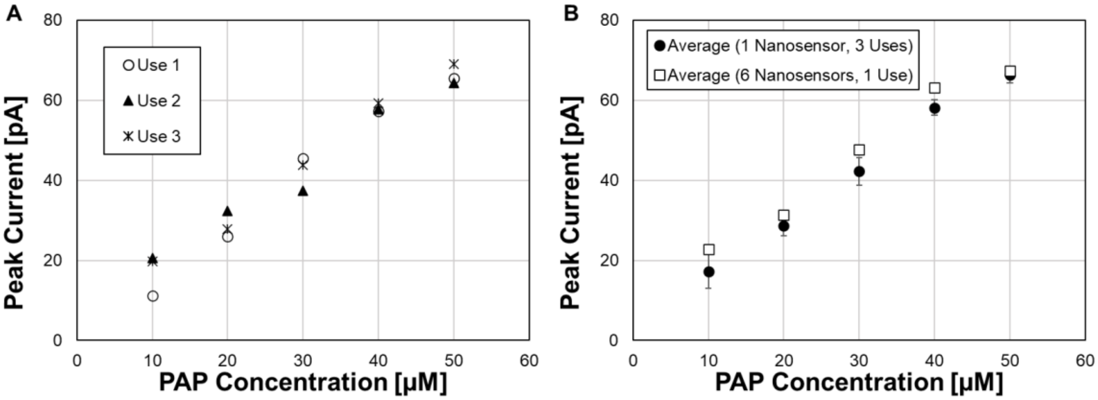

Figure 4-15: Standard curve of nanosensor aging.
A) Standard curve of the nanosensor response when used repeatedly. B) Standard curves showing the average response of a single nanosensor used three times over the course of three days to characterize the redox of PAP from 10 – 50 μM compared to the average response of 6 nanosensors, each used for a single characterization. Error bars represent the standard deviation of the electrode response over three uses. Cyclic voltammograms were recorded in a PBS solution containing 100 mM NaCl at a scan rate of 10 mV·s^{-1}.

4.3.6. Electrode Characterization in Heterogeneous Environments

The two-electrode nanosensor can detect PAP in cell lysate, demonstrating the utility of measuring electroactive analytes in heterogeneous environments. In biological applications, electrodes can become passivated when exposed to biological fluids as the adsorption of proteins onto the surface reduces the electrochemically active area of the electrode. The effects of biofouling on the nanoprobe were investigated by collecting voltammograms in 80 mL of HEK-293 whole cell lysate for PAP concentrations of 10 – 50 μM. Figure 4-16 shows the average standard response for 3 unique nanosensors. As expected, the average maximum current and slope of the standard curve of PAP measurements in cell lysate decreased compared to the same PAP measurements made in PBS. However, as noted in Table 4-1, the nanosensor's LOD in cell lysate was similar to the LOD in the less contaminated PBS environment. These results highlight the utility of the nanosensor in detecting PAP, and potentially other electroactive analytes, in heterogeneous environments where biofouling is a concern.

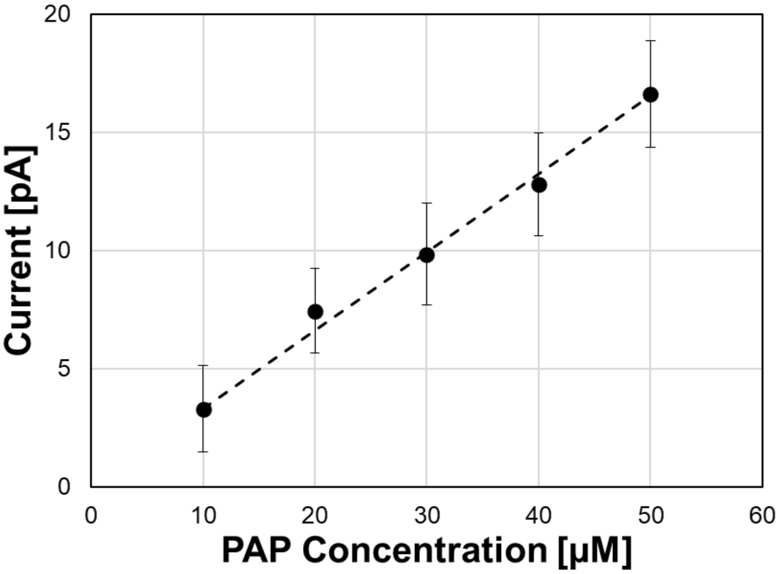

Figure 4-16: Voltammetric response of nanosensor in cell lysate. Average voltammetric response of 3 nanosensors in HEK-293 lysate without supporting electrolyte. Error bars denote the standard deviation. All voltammograms were recorded at a scan rate of 10 mV·s^{-1}.

Many other works have reported the use of carbon ultramicro- and nanoelectrodes for use in cellular environments which have the potential for biofouling [112,113,117,118,124,174,175]. All the groups were able to quantify analyte within individual cells irrespective of biofouling. These reports, along with the results of this work, indicate that carbon nanoelectrodes are a useful electrode for analyzing environments where biofouling may occur. These carbon-based sensors were able to quantify species of interest in biological domains despite biofouling. This evidence supports that no additional steps need to be taken to prevent biofouling.

4.3.7. Electrode Characterization of Enzymatic Reactions

To further demonstrate the utility of the nanosensor, the enzymatic reaction of β-Gal and PAPG was characterized and the resulting data used to evaluate the enzyme kinetics. As seen in Figure 4-17, the reaction progressed until approximately 50 minutes after the addition of 40 µM PAPG. For consistency, voltammograms were collected at 5 minutes to generate the standard curve seen in Figure 4-18. The Lineweaver–Burk plot shown in Figure 4-19 was used to determined the Michaelis–Menten constant (K_m), a value which indicates the substrate affinity when reacting with an enzyme. A linear model of the form $y(x) = m \cdot x + b$ was fit to the inverse of the peak current versus the inverse of the substrate concentration. The y-intercept ($1/I_{max}$) and slope (K_m/I_{max}) or the x-intercept ($-1/K_m$) of this linear model can be used to determine K_m. Through this method it was experimentally determined that the K_m of β-gal and PAPG was 352 µM. This is in agreement with the experimentally determined values reported in the literature of 360, 430 and 330 µM using electrochemical and spectrophotometric methods [147,176,177].

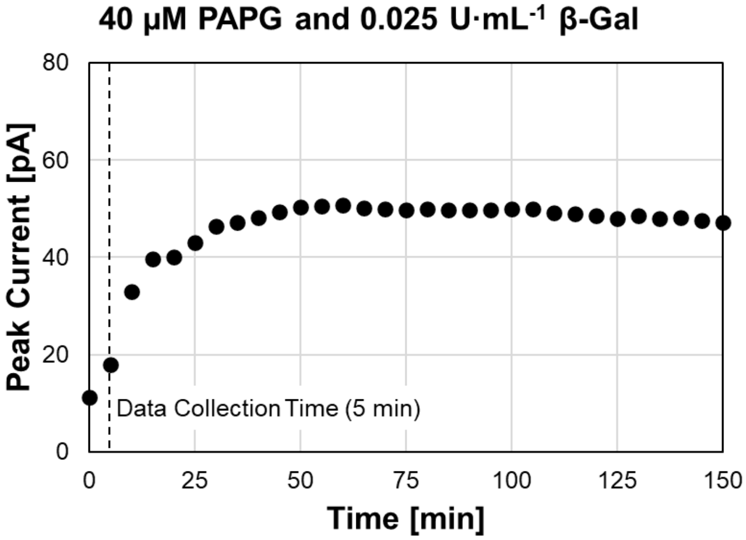

Figure 4-17: Time dependence of the standard curve of the PAPG and β-gal enzymatic reaction.

All voltammograms were recorded at a scan rate of 10 mV·s^{-1}.

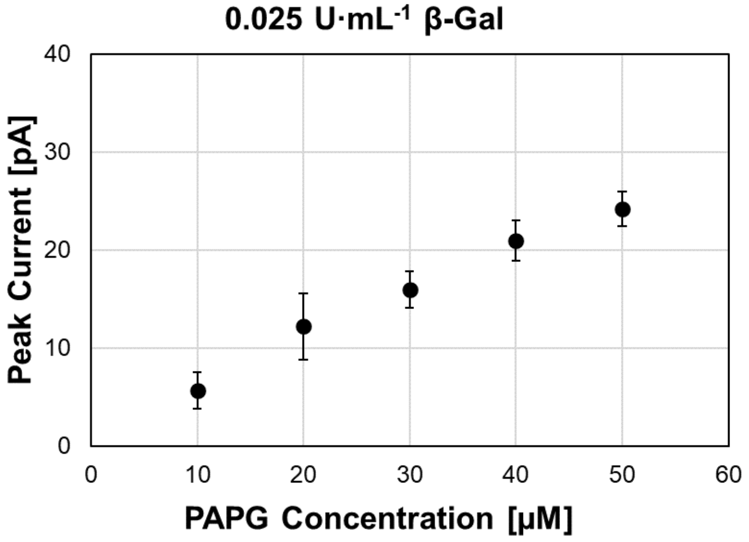

Figure 4-18: Standard curve of the b-gal and PAPG reaction.
Average voltammetric response of 4 nanosensors while characterizing the enzymatic PAPG and β-gal in a PBS solution with 100 mM NaCl as a supporting electrolyte. Error bars represent the standard deviation of the electrode response. All voltammograms were recorded at a scan rate of 10 mV·s^{-1}.

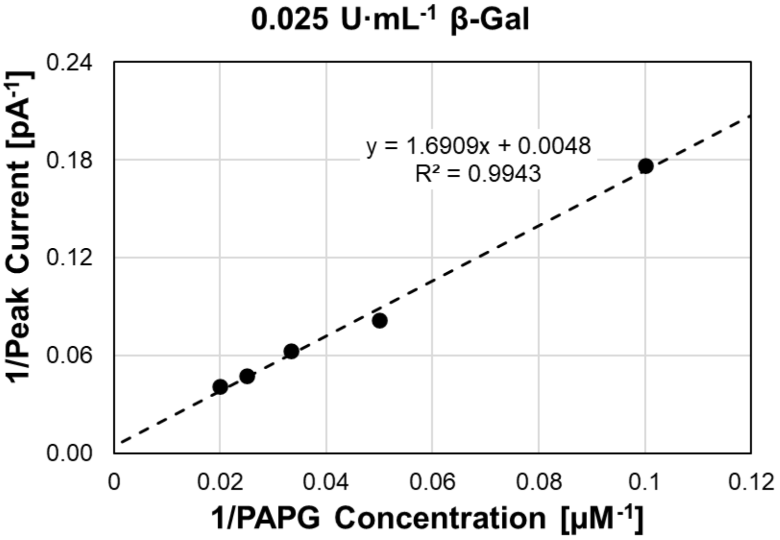

Figure 4-19: Lineweaver−Burk plot
Lineweaver−Burk plot created from the average response of 4 electrodes while characterizing the enzymatic PAPG and β-gal. All voltammograms were recorded at a scan rate of 10 mV·s^{-1}.

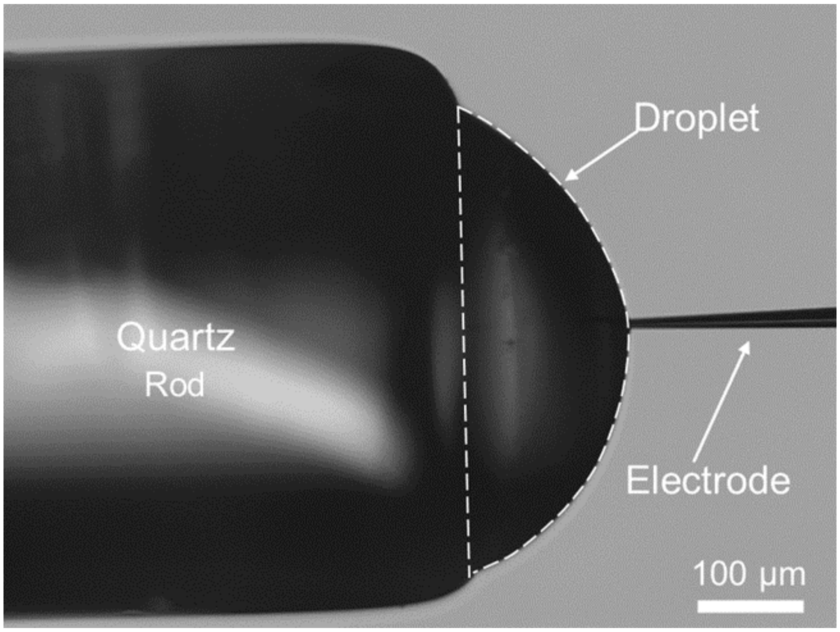

Figure 4-20: Two-electrode nanosensor interrogating a microenvironment.
Optical micrograph of the two-electrode nanoprobe positioned in a 50 nL PBS droplet placed on the end of a 1 mm diameter quartz rod.

4.3.8. Electrode Characterization in Microenvironments

The nanosensor was able to detect small concentrations of redox species within an aqueous microenvironment. Single 50 nL droplets of 0-50 µM PAP in PBS were positioned on the end of a quartz rod. The nanosensor was positioned in each droplet using a micromanipulator under an optical microscope, as shown in Figure 4-20. To better mimic nonideal conditions, where the microdroplet is exposed to an atmospheric environment, evaporation of the droplet was not prevented.

Evaporation increased the concentration of analyte within the droplet and resulted in a standard curve with a slope higher than expected, as shown in Figure 4-21. Optical imaging was used to quantify the impact of droplet evaporation on the change in analyte concentration to accurately quantify the dependence of current on PAP concentration. A series of images of the droplet was collected every 5 seconds until the droplet completely evaporated at approximately 220 s. From these images, the droplet volume was calculated by modeled the droplet as a spherical segment and a plot of the droplet volume as a function of time, shown in Figure 4-22, was generated. A linear model of the form $y(x) = m \cdot x + b$ was fit to this data and the slope was used to determine that the evaporation rate was approximately 25 nL·s. This information could then be used to determine the concentration of the droplet at the time the peak current was measured (60 s) using conservation of mass.

$$C_e = \frac{C_o V_o}{V_e} \tag{4-7}$$

Where C_e and V_e are the concentration and volume of the evaporated droplet at 60 s and C_o and V_o are the concentration and volume of the original, 50 nL droplet. Based on an evaporation rate of 25 nL·s, the droplet had lost 15 nL of volume by 60 s. The corresponding C_e for each C_o was calculated and used to scale the standard curve. When the concentration of the droplet is scaled to account for evaporation during the experiment, the nanosensor was found to perform similarly in bulk solutions and microenvironments, as seen in Figure 4-21. After scaling for droplet evaporation, a linear increase of current with respect to PAP concentration was observed with a slope of 5.4 pA per µM and an R^2 value of 0.97.

These results indicate that the nanoelectrode system is capable of interrogating small environments without the need of positioning multiple electrodes within the droplet. By reducing the number of probes required to perform the electrochemical analysis, the accessible domain size is also reduced.

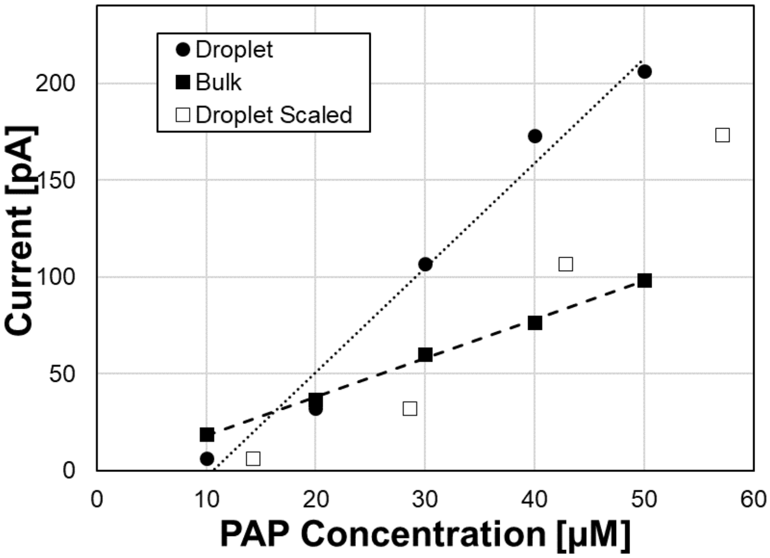

Figure 4-21: Voltammetric response in a microenvironment. Voltammetric response of the nanoprobe while characterizing the redox behavior of PAP in 50 nL droplets containing PBS, 100 mM NaCl, and 0 – 50 µM PAP at a scan rate of 10 mV·s^{-1}.

4.4. CONCLUSIONS

In this Chapter a novel carbon-based, two electrode system contained within a single nanoscale tip capable of electrochemical analysis within microenvironments was described. The low-cost fabrication method was shown to be capable of producing two independent electrodes located within 50 nm of each other. An electrodeposition procedure was developed and implemented to reliably convert one of the carbon working electrodes to a chlorinated silver pseudo-reference electrode while maintaining the performance of the other working electrode. The voltammetric response of the self-contained electrode system was modeled with the Butler-Volmer model. Cell lysate was used to demonstrate that the nanosensor can still detect small concentrations of analyte despite biofouling. As the working and reference electrodes are contained within a single nanosensor, there was no need to position external electrodes within the electrochemical cell, enabling analysis within very small domains.

This nanosensor has the potential to become a unique and widely accessible tool for the electrochemical characterization of microenvironments such as single living cells, “green” electrochemistry, or applications requiring high spatial resolution. The results of this work are significant beyond the scope of the developed nanosensor as they present a new method for fabricating reference electrodes which could be extended to an array of geometries and length-scales.

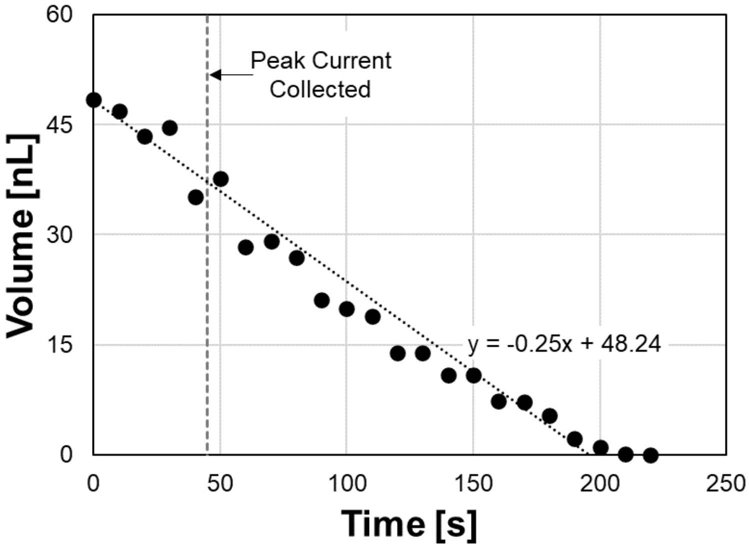

Figure 4-22: Evaporation rate of microenvironment.
Volume of the aqueous droplet determined via optical micrographs as a function of time.

Chapter 5

5. CONTRIBUTIONS AND FUTURE DIRECTIONS

Nanoscale sensors are required to study the interesting and complex physical and biological phenomenon which occurs in microdomains. Even microscale sensors are often prohibitively large and cannot access such small domains or disrupt the phenomena they are intended to study. As manufacturing techniques have improved, the production of nanoscale sensors has become an active area of research. Such sensors are often costly to produce and require complex manufacturing procedures. In this work, a simple manufacturing process was developed which enables the production of low-cost aligned carbon nanostructures which are directly integrated into macroscale templates. These carbon structures serve as the scaffold for the production of electrochemical and thermal nanosensors. The thermocouple developed through this research uses a novel manufacturing method and set of materials to overcome the reduction in thermoelectric performance associated with small sensor sizes. The electrochemical sensor presented in this work overcomes challenges associated with other nanoscale sensors by allowing a working and reference electrode to be located within 50 nm of each other, minimizing the overall sensor footprint and enabling chemical detection in microdomains.

5.1. KEY CONTRIBUTIONS

- A template-based method for fabricating a diverse range of aligned carbon micro- and nanostructures was developed.
- Template-based synthesis enables the scalable production of carbon-structures that readily interface with standard laboratory equipment.

- The carbon structures generated with template-based synthesis were shown to be amenable to modification enabling them to serve as unique nanosensors.
- Electrodeposition and physical vapor deposition were utilized to modify a carbon nanostructure and form a novel thermocouple with a 450 nm tip diameter.
- The nanoscale thermocouple was able to readily interface with standard laboratory equipment because of its integration into a macroscale quartz capillary.
- The nanoscale thermocouple was shown to have a 68% increase in thermoelectric power relative to other micropipette-based thermocouples.
- The nanoscale thermocouple was shown to have a 207% increase in the Ioffe criteria relative to other micropipette-based thermocouples.
- A novel carbon-based two electrode system with two, independent electrodes separated by less than 50 nm separation was developed.
- An electrodeposition process was explored to convert a carbon nanoelectrode to a chlorinated silver pseudo-reference electrode while maintaining the performance of the nearby carbon working electrode. This enabled the production of an electrochemical sensor with a working and reference electrode positioned within 50 nm of each other.
- The electrochemical nanosensor was demonstrated to be capable of quantifying small concentrations of analyte in bulk environments.
- The voltammetric response of the nanosensor was described with the Butler-Volmer model.
- The electrochemical nanosensor was shown to be capable of interrogating 50 nL aqueous droplets without the need of an external reference electrode.

- The electrochemical nanosensor was demonstrated to be capable of withstanding biofouling by detecting small concentrations of analyte in cell lysate.
- The electrochemical nanosensor was utilized to characterize the enzymatic reaction of PAPG and β-gal.

5.2. FUTURE DIRECTIONS

In this work, a unique method for producing nanoscopic sensors for interrogating microdomains was presented. A novel self-contained electrochemical nanosensor was described and demonstrated to be capable of detecting small concentrations of analyte in small aqueous droplets and heterogenous environments. A thermocouple with an improved thermoelectric power was described and calibrated. Some potential future research directions are suggested below.

5.2.1. Thermocouple Future Directions

Explore Alternative Metallic Coatings: As described in Chapter 3, the thermoelectric power of a thermocouple is dependent on the type of metals used and the quality of the films. As the scale of the thermocouple approaches the nanoscale, reduction in the quality of the film is inevitable and thus the thermoelectric power is reduced compared to that using the Seebeck coefficients of the bulk materials. To overcome this reduction in thermoelectric power and maintain adequate thermocouple sensitivity, care must be taken to select metals with substantially different Seebeck coefficients. In this work, nickel and gold were selected as they have a maximum thermoelectric power of 19.79 $\mu V \cdot K^{-1}$ which is higher than that of other similar micropipette-based thermocouples. However, other materials can be explored to further improve the thermoelectric power of the nanoscale thermocouple. For example, chromium has a bulk Seebeck coefficient of 21.8 $\mu V \cdot K^{-1}$ at 300 K and can be physical vapor deposited to form a thin continuous film [178]. An external chromium thin film coupled with a nickel core could offer a maximum thermoelectric power of 39.8 $\mu V \cdot K^{-1}$, double that presented in this work. Further, a 57 mm diameter chromium sputter target costs 675.00 USD compared to 625.00 USD for a 57 mm gold sputter target. Thus, the potential increase in thermoelectric power would not pose a significant increase in financial cost [179]. Further work would need to be done to determine if the coating produced by physical vapor deposition of chromium was high enough quality to suit this application.

Additional Characterization of the Thermocouple: Additional characterization of the thermocouple would provide insights into its potential to interrogate practical applications. The aging characteristics and mechanical degradation of the thermocouple due to fluid contamination, fouling, and chaotic turbulent flows of the thin metallic films should be investigated. The thermocouple was characterized from 0 to 60 °F however this range should be extended to determine the temperature limits of the sensor. Additionally, dynamic characterization of the thermocouple should be performed to determine the response time of the thermocouple.

Expand Experimental Conditions: Characterization of the electrochemical and thermal sensor was performed in aqueous conditions. Numerous applications, including ion-batteries, nano-porous separation membranes, and supercapacitors, would benefit from enhanced characterization provided by nanoscale sensors due to the heterogenous ion transfer that occurs in such systems [164]. As such, characterization of the sensors in nonaqueous environments would provide potentially useful insights. The sensors were designed such that aqueous electrolytes are not required however their suitability for nonaqueous environments has not yet been investigated. In addition, the response of the thermocouple in nonhomogeneous environments should be investigated to determine the effects of fouling on the performance of the sensor.

Polymer Coating: It may be advantageous to coat the exterior of the thermocouple in a thin polymer film to protect the exterior gold film. Gold is the most noble of the noble metals and is thus immune to corrosion and oxidation however the thin gold film may be prone to mechanical damage along the pipette shank. Thus, an exterior polymer coating may enhance the mechanical durability of the thermocouple. In addition, a polymer coating may improve the biocompatibility of the sensor. For example, Kakuta *et al.* utilized the biocompatible 2-methacryloyloxyethyl phosphorylcholine polymer on their micropipette based thermocouple [86]. Further, da Silva *et al.* utilized polyvinyl chloride (PVC) to reinforce the structure of their self-contained electrochemical sensor [131]. The process used to form this thin protective coating consisted dissolving PVC in tetrahydrofuran (THF) (1:6 w/v) and submerging the device into the solution. The THF solvent evaporates leaving a coating of PVC on the sensor.

Investigate Hollow Sensors: Hollow electrochemical and thermal sensors have been an area of active research interest to enable the simultaneous delivery of reactants to and characterization of microdomains. The fabrication methods of both the electrochemical sensor and thermocouple were designed to facilitate the production of hollow devices. The thickness of the carbon and subsequent coatings can be optimized such that the lumen of the micropipette is not filled yet the device is sufficiently robust to withstand subsequent characterization.

5.2.2. Self-contained Electrochemical Sensor Future Directions

Improve Electrochemical Sensor Manufacturing Rate of Production: As described in Chapter 4, the self-contained electrochemical sensor is produced in a four-step manufacturing process which, briefly, includes forming a template, depositing carbon via CVD, selectively etching the template to expose the amorphous CNPs, and electrodepositing a layer of silver to enable one CNP to serve as a reference electrode. Currently, this sequence of manufacturing steps produces six sensors in two days. The template formation process is limited to forming two micropipettes at a time however there exists a potential for scale-up for the other three fabrication steps.

The CVD process should be examined to determine what modifications should be made to the parameters (gas flow rate, time, etc.) to enable the deposition of carbon on an increased number of micropipettes. As seen in Figure 5-1, when the number of samples in the CVD process increases, the amount of deposited carbon decreases. There, it is necessary to either increase the deposition time or increase the flow rate of methane relative to the argon flow rate.

6 Samples in CVD

12 Samples in CVD

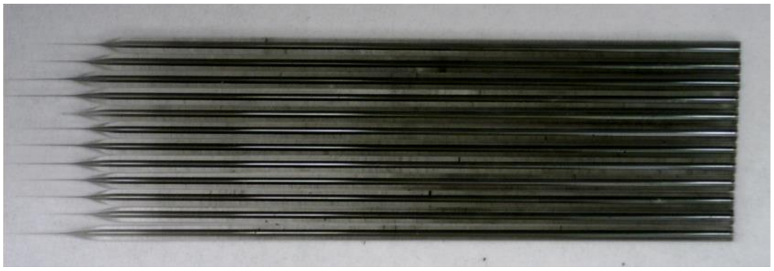

Figure 5-1: Effect of number of samples in CVD process on the amount of carbon deposited on template.

Currently all six carbon pipettes are simultaneously etched in hydrofluoric acid but with modification to the sample holder, the throughput of this process could be increased. Further, the current electrodeposition process enables the deposition of a thin silver film onto a single pipette however the process should be modified to enable the simultaneous electrodeposition onto multiple electrodes. Again, the process parameters, specifically the applied current, would need to be modified to ensure that a 60 p A current was still applied to each sample.

Utilize Electrochemical Sensor for Intracellular Analysis: The quantification of intracellular biomolecules is a critical step in understanding cellular processes, communication, and disease pathology [1]. The CNP-based electrochemical sensor developed in Chapter 4 is a good candidate for performing intracellular electrochemistry and selectively identifying and quantifying biomolecules within individual living cells. In this work the sensor was shown to be capable of detecting analyte in microdomains and in cell lysate. Further, the sensor was capable of quantifying biologically relevant enzymatic reactions. It is hypothesized that the electrochemical probe will have several distinct advantages over other detection techniques. *Firstly*, the proposed CNT-based sensor has a very refined tip size and would therefore be minimally invasive and reduce the possibility of irreversible cell damage. This will allow for individual living cells to be monitored over extended periods of time. *Secondly*, with modification to produce a hollow sensor, the CNP-based nanoprobe could inject reagents or other tagging molecules to serve as markers which allow high selectivity in quantifying target biomolecules. *Thirdly*, the nanoscale tip of the probe can provide high spatial resolution within the cell.

5.2.3. Expanded Future Directions

Develop an Integrated Thermal and Electrochemical Sensor: In their 2017 work, Pan *et al.* identified temperature as a crucial parameter in chemical processes including those found in energy storage and conversion and biosensors [180]. They further stressed the importance of integrated electrochemical and thermal sensors capable of simultaneous thermal imaging and electrochemical analysis to provide insights in the kinetic and transport processes of reactions. As the thermocouple and electrochemical sensors developed in this work rely on the same micropipette scaffold, it is possible to integrate the two sensors into a single device. The multibarrel pipette developed in Section 2.2 has the potential to serve as a scaffold for such a sensor. As such, the manufacturing process should be refined to produce distinct barrels and the techniques used to deposit thin films on the resultant carbon structures should be used to modify the amorphous CNPs to serve as reference electrodes and thermal sensors.

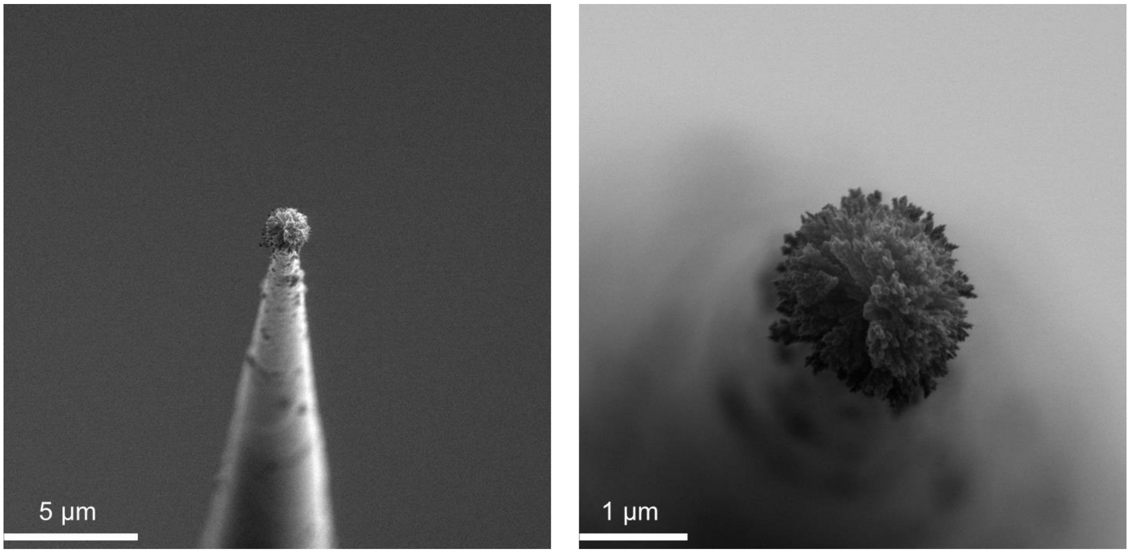

Figure 5-2: SEM micrographs of gold agglomerations formed on perpendicularly oriented samples.

Investigate Enhanced Surface Area Electrodes: As described in Chapter 4, the response of an electrode is related to the electrochemically active area of the electrode. Increasing the surface area of electrodes has been an active area of research [181–183]. During preparation of electrodes for SEM imaging, it was noted that if the samples were positioned perpendicularly to the sputter coater target, a unique agglomeration of gold would form on the tip of the electrode, as shown in Figure 5-2. This unique feature contains significant surface area within a 2 µm tip. As gold has been demonstrated to be a stable electrode material, this structure may have promise as a high-area gold microelectrode. The carbon lumen would provide a convenient electrical connection to the microscale gold agglomerate. It is recommended that this phenomenon be further explored to determine if this structure can be utilized as an electrode.

References

[1] Armbrecht, L., and Dittrich, P. S., 2017, “Recent Advances in the Analysis of Single Cells,” Anal. Chem., **89**(1), pp. 2–21.

[2] Sun, P., Laforge, F. O., and Mirkin, M. V., 2007, “Scanning Electrochemical Microscopy in the 21st Century,” Phys. Chem. Chem. Phys., **9**(7), pp. 802–823.

[3] Ying, Y. L., Ding, Z., Zhan, D., and Long, Y. T., 2017, “Advanced Electroanalytical Chemistry at Nanoelectrodes,” Chem. Sci., **8**(5), pp. 3338–3348.

[4] Kim, M. M., Giry, A., Mastiani, M., Rodrigues, G. O., Reis, A., and Mandin, P., 2015, “Microscale Thermometry: A Review,” Microelectron. Eng., **148**, pp. 129–142.

[5] Khanna, V. K., 2011, *Nanosensors : Physical, Chemical, and Biological*, Taylor & Francis.

[6] Scheibel, O. V, and Schrlau, M. G., 2017, “Carbon Nanotube-Based Sensors: Overview,” *Comprehensive Biomaterials II*, P. Ducheyne, ed., Elsevier, Oxford, United Kingdom, pp. 690–702.

[7] Al-Jumaili, A., Alancherry, S., Bazaka, K., and Jacob, M. V., 2017, “Review on the Antimicrobial Properties of Carbon Nanostructures,” Materials (Basel)., **10**(9), p. 1066.

[8] Rasheed, P. A., and Sandhyarani, N., 2017, “Carbon Nanostructures as Immobilization Platform for DNA: A Review on Current Progress in Electrochemical DNA Sensors,” Biosens. Bioelectron., **97**, pp. 226–237.

[9] Chen, R. S., Huang, W. H., Tong, H., Wang, Z. L., and Cheng, J. K., 2003, “Carbon Fiber Nanoelectrodes Modified by Single-Walled Carbon Nanotubes,”

Anal. Chem., **75**(22), pp. 6341–6345.

[10] Agrawal, K. V., Shimizu, S., Drahushuk, L. W., Kilcoyne, D., and Strano, M. S., 2017, “Observation of Extreme Phase Transition Temperatures of Water Confined inside Isolated Carbon Nanotubes,” Nat. Nanotechnol., **12**(3), pp. 267–273.

[11] Golshadi, M., and Schrlau, M. G., 2012, “Template-Based Synthesis of Aligned Carbon Nanotube Arrays for Microfluidic and Nanofluidic Applications,” ECS Trans., **50**(33), pp. 1–14.

[12] Sun, L., and Crooks, R. M., 2000, “Single Carbon Nanotube Membranes: A Well-Defined Model for Studying Mass Transport through Nanoporous Materials,” J. Am. Chem. Soc., **122**(49), pp. 12340–12345.

[13] Ito, T., Sun, L., and Crooks, R. M., 2003, “Simultaneous Determination of the Size and Surface Charge of Individual Nanoparticles Using a Carbon Nanotube-Based Coulter Counter,” Anal. Chem., **75**(10), pp. 2399–2406.

[14] Kim, B. M., Murray, T., and Bau, H. H., 2005, “The Fabrication of Integrated Carbon Pipes with Sub-Micron Diameters,” Nanotechnology, **16**(8), pp. 1317–1320.

[15] Mohamed, A., 2018, “Synthesis, Characterization, and Applications Carbon Nanofibers,” *Carbon-Based Nanofillers and Their Rubber Nanocomposites: Carbon Nano-Objects*, Elsevier, pp. 243–257.

[16] Tasis, D., Tagmatarchis, N., Bianco, A., and Prato, M., 2006, “Chemistry of Carbon Nanotubes,” Chem. Rev., **106**(3), pp. 1105–1136.

[17] Xiong, Y., Xie, Y., Li, X., and Li, Z., 2004, “Production of Novel Amorphous Carbon Nanostructures from Ferrocene in Low-Temperature Solution,” Carbon N.

Y., **42**(8–9), pp. 1447–1453.

[18] Bethune, D. S., Kiang, C. H., de Vries, M. S., Gorman, G., Savoy, R., Vazquez, J., and Beyers, R., 1993, "Cobalt-Catalysed Growth of Carbon Nanotubes with Single-Atomic-Layer Walls," Nature, **363**(6430), pp. 605–607.

[19] Guo, T., Nikolaev, P., Thess, A., Colbert, D. T., and Smalley, R. E., 1995, "Catalytic Growth of Single-Walled Manotubes by Laser Vaporization," Chem. Phys. Lett., **243**(1–2), pp. 49–54.

[20] Amelinckx, S., Zhang, X. B., Bernaerts, D., Zhang, X. F., Ivanov, V., and Nagy, J. B., 1994, "A Formation Mechanism for Catalytically Grown Helix-Shaped Graphite Nanotubes," Science (80-.)., **265**(5172), pp. 635 LP – 639.

[21] Melechko, A. V., Merkulov, V. I., McKnight, T. E., Guillorn, M. A., Klein, K. L., Lowndes, D. H., and Simpson, M. L., 2005, "Vertically Aligned Carbon Nanofibers and Related Structures: Controlled Synthesis and Directed Assembly," J. Appl. Phys., **97**(4).

[22] Iijima, S., 1991, "Helical Microtubules of Graphitic Carbon," Nature, **354**(6348), pp. 56–58.

[23] Arora, N., and Sharma, N. N., 2014, "Arc Discharge Synthesis of Carbon Nanotubes: Comprehensive Review," Diam. Relat. Mater., **50**, pp. 135–150.

[24] Prasek, J., Drbohlavova, J., Chomoucka, J., Hubalek, J., Jasek, O., Adam, V., and Kizek, R., 2011, "Methods for Carbon Nanotubes Synthesis - Review," J. Mater. Chem., **21**(40), pp. 15872–15884.

[25] Eatemadi, A., Daraee, H., Karimkhanloo, H., Kouhi, M., Zarghami, N., Akbarzadeh, A., Abasi, M., Hanifehpour, Y., and Joo, S. W., 2014, "Carbon

Nanotubes: Properties, Synthesis, Purification, and Medical Applications," Nanoscale Res. Lett., **9**(1), pp. 1–13.

[26] Baddour, C. E., and Briens, C., 2005, "Carbon Nanotube Synthesis: A Review," Int. J. Chem. React. Eng., **3**(1).

[27] Li, W. Z., Xie, S. S., Qian, L. X., Chang, B. H., Zou, B. S., Zhou, W. Y., Zhao, R. A., and Wang, G., 1996, "Large-Scale Synthesis of Aligned Carbon Nanotubes," Science (80-.)., **274**(5293), pp. 1701 LP – 1703.

[28] Che, G., Lakshmi, B. B., Martin, C. R., Fisher, E. R., and Ruoff, R. S., 1998, "Chemical Vapor Deposition Based Synthesis of Carbon Nanotubes and Nanofibers Using a Template Method," Chem. Mater., **10**(1), pp. 260–267.

[29] Schrlau, M. G., and Bau, H. H., 2009, "Carbon-Based Nanoprobes for Cell Biology," Microfluid. Nanofluidics, **7**(4), pp. 439–450.

[30] Ajayan, P. M., 1999, "Nanotubes from Carbon," Chem. Rev., **99**(7), pp. 1787–1799.

[31] Ebbesen, T. W., Lezec, H. J., Hiura, H., Bennett, J. W., Ghaemi, H. F., and Thio, T., 1996, "Electrical Conductivity of Individual Carbon Nanotubes," Nature, **382**(6586), pp. 54–56.

[32] Bandaru, P. R., 2007, "Electrical Properties and Applications of Carbon Nanotube Structures," J. Nanosci. Nanotechnol., **7**(4–5), pp. 1239–1267.

[33] Stransfield, A., 1912, *The Electric Furnace: It's Construction, Operation and Uses*.

[34] Schrlau, M. G., Falls, E. M., Ziober, B. L., and Bau, H. H., 2008, "Carbon Nanopipettes for Cell Probes and Intracellular Injection," Nanotechnology, **19**(1),

p. 015101.

[35] Shim, B. S., Chen, W., Doty, C., Xu, C., and Kotov, N. A., 2008, “Smart Electronic Yarns and Wearable Fabrics for Human Biomonitoring Made by Carbon Nanotube Coating with Polyelectrolytes,” Nano Lett., **8**(12), pp. 4151–4157.

[36] Huang, X. J., and Choi, Y. K., 2007, “Chemical Sensors Based on Nanostructured Materials,” Sensors Actuators, B Chem., **122**(2), pp. 659–671.

[37] Koehne, J., Chen, H., Li, J., Cassel, A. M., Ye, Q., Ng, H. T., Han, J., and Meyyappan, M., 2003, “Ultrasensitive Label-Free DNA Analysis Using an Electronic Chip Based on Carbon Nanotube Nanoelectrode Arrays,” Nanotechnology, **14**(12), pp. 1239–1245.

[38] McKnight, T. E., Melechko, A. V., Griffin, G. D., Guillorn, M. A., Merkulov, V. I., Serna, F., Hensley, D. K., Doktycz, M. J., Lowndes, D. H., and Simpson, M. L., 2003, “Intracellular Integration of Synthetic Nanostructures with Viable Cells for Controlled Biochemical Manipulation,” Nanotechnology, **14**(5), pp. 551–556.

[39] Li, J., Cassell, A., Delzeit, L., Han, J., and Meyyappan, M., 2002, “Novel Three-Dimensional Electrodes: Electrochemical Properties of Carbon Nanotube Ensembles,” J. Phys. Chem. B, **106**(36), pp. 9299–9305.

[40] Dai, H., Hafner, J. H., Rinzler, A. G., Colbert, D. T., and Smalley, R. E., 1996, “Nanotubes as Nanoprobes in Scanning Probe Microscopy,” Nature, **384**(6605), pp. 147–150.

[41] Patil, A., Sippel, J., Martin, G. W., and Rinzler, A. G., 2004, “Enhanced Functionality of Nanotube Atomic Force Microscopy Tips by Polymer Coating,”

Nano Lett., **4**(2), pp. 303–308.

[42] Chen, X., Kis, A., Zettl, A., and Bertozzi, C. R., 2007, “A Cell Nanoinjector Based on Carbon Nanotubes,” Proc. Natl. Acad. Sci. U. S. A., **104**(20), pp. 8218–8222.

[43] Kaempgen, M., and Roth, S., 2005, “Ultra Microelectrodes from MWCNT Bundles,” *Synthetic Metals*, Elsevier, pp. 353–356.

[44] Kouklin, N. A., Kim, W. E., Lazareck, A. D., and Xu, J. M., 2005, “Carbon Nanotube Probes for Single-Cell Experimentation and Assays,” Appl. Phys. Lett., **87**(17), pp. 1–3.

[45] Freedman, J. R., Mattia, D., Korneva, G., Gogotsi, Y., Friedman, G., and Fontecchio, A. K., 2007, “Magnetically Assembled Carbon Nanotube Tipped Pipettes,” Appl. Phys. Lett., **90**(10), p. 103108.

[46] Parthasarathy, R. V., Phani, K. L. N., and Martin, C. R., 1995, “Template Synthesis of Graphitic Nanotubules,” Adv. Mater., **7**(11), pp. 896–897.

[47] Jimenez, A. I. P., Challier, L., Di Pisa, M., Guille-Collignon, M., Lemaître, F., Lavielle, S., Mansuy, C., Amatore, C., Labbé, E., and Buriez, O., 2015, “Three-Electrode Analytical and Preparative Electrochemistry in Micro-Volume Hanging Droplets,” Electrochem. commun., **54**, pp. 41–45.

[48] Che, G., Lakshmi, B. B., Fisher, E. R., and Martin, C. R., 1998, “Carbon Nanotubule Membranes for Electrochemical Energy Storage and Production,” Nature, **393**(6683), pp. 346–349.

[49] Che, G., Lakshmi, B. B., Martin, C. R., Fisher, E. R., and Ruoff, R. S., 1998, “Chemical Vapor Deposition Based Synthesis of Carbon Nanotubes and Nanofibers Using a Template Method,” Chem. Mater., **10**(1), pp. 260–267.

[50] Scheibel, O. V, Lanza, D., and Schrlau, M. G., 2017, “Template-Based Synthesis of Integrated Carbon Micro- and Nanostructures,” *ASME International Mechanicl Engineering Congress and Exposition*, p. 6.

[51] Fang, D. Z., Striemer, C. C., Gaborski, T. R., McGrath, J. L., and Fauchet, P. M., 2010, “Pore Size Control of Ultrathin Silicon Membranes by Rapid Thermal Carbonization,” Nano Lett., **10**(10), pp. 3904–3908.

[52] Paulose Nadappuram, B., McKelvey, K., Byers, J. C., Gu, A. G., Colburn, A. W., Lazenby, R. A., and Unwin, P. R., 2015, “Quad-Barrel Multifunctional Electrochemical and Ion Conductance Probe for Voltammetric Analysis and Imaging,” Anal. Chem, **87**(7), pp. 3566–3573.

[53] Liu, D., Zhang, J., Liu, Y., Xu, J., and Benstetter, G., 2005, “Growth Processes and Surface Properties of Diamondlike Carbon Films,” J. Appl. Phys., **97**(10), p. 104901.

[54] Ito, A. M., Takayama, A., Saito, S., Ohno, N., Kajita, S., and Nakamura, H., 2011, “Molecular Dynamics Simulation of Chemical Vapor Deposition of Amorphous Carbon: Dependence on H/C Ratio of Source Gas,” *Japanese Journal of Applied Physics*, p. 01AB01.

[55] Bretag, A. H., 2017, “The Glass Micropipette Electrode: A History of Its Inventors and Users to 1950,” J. Gen. Physiol., **149**(4), pp. 417–430.

[56] Barber, M. A., 1904, “A New Method of Isolating Micro-Organisms,” J. Kans. Med. Soc., **4**, pp. 489–494.

[57] Taylor, C. V, and Whitaker, D. M., 1927, “Potentiometric Determinations in the Protoplasm and Cell-Sap of Nitella,” Protoplasma, **3**(1), pp. 1–6.

[58] Graham, J., and Graham, R. W., 1942, “Membrane and Injury Potentials of Single Muscle Fibers,” Fed. Proc., **1**, p. 31.

[59] Graham, J., and Gerard, R. W., 1946, “Membrane Potentials and Excitation of Impaled Single Muscle Fibers,” J. Cell. Comp. Physiol., **28**(1), pp. 99–117.

[60] Ling, G., and Gerard, R. W., 1949, “The Normal Membrane Potential of Frog Sartorius Fibers,” J. Cell. Comp. Physiol., **34**(3), pp. 383–396.

[61] Alexander, J. ~T., and Nastuk, W. ~L., 1953, “An Instrument for the Production of Microelectrodes Used in Electrophysiological Studies,” Rev. Sci. Instrum., **24**(7), pp. 528–531.

[62] Brown, K. T., and Flaming, D. G., 1986, *Advanced Micropipette Techniques for Cell Physiology*, Wiley & Sons, New York.

[63] Dun, N. J., Kaibara, K., and Karczmar, A. G., 1977, “Dopamine and Adenosine 3’,5’-Monophosphate Responses of Single Mammalian Sympathetic Neurons,” Science (80-.)., **197**(4305), pp. 778–780.

[64] Brailoiu, E., and Miyamoto, M. ., 1999, “Inositol Trisphosphate and Cyclic Adenosine Diphosphate-Ribose Increase Quantal Transmitter Release at Frog Motor Nerve Terminals: Possible Involvement of Smooth Endoplasmic Reticulum,” Neuroscience, **95**(4), pp. 927–931.

[65] Lalley, P. ., Moschovakis, A. K., and Windhorst, U., 1999, “Electrical Activity of Individual Neurons in Situ: Extra- and Intracellular Recording,” *Modern Techniques in Neuroscience Research*, U. Windhorst, and H. Johansson, eds., Springer, Berlin, Heidelberg, pp. 127–172.

[66] Schrlau, M. G., Dun, N. J., and Bau, H. H., 2009, “Cell Electrophysiology with

Carbon Nanopipettes," ACS Nano, **3**(3), pp. 563–568.

[67] Arowosola, A., Fujimoto, A., Scheibel, O., and Schrlau, M. G., 2015, "Fabrication of Theta Carbon Nanopipettes Using a Template-Based Chemical Vapor Deposition Nanomanufacturing Process," J. Multidiscip. Eng. Sci. Technol., **2**(5), pp. 3159–3199.

[68] Bergman, T. L., and F.P., I., 2011, *Fundamentals of Heat and Mass Transfer*, Wiley, Hoboken, NJ.

[69] Hüttinger, K. J., 1998, "CVD in Hot Wall Reactors - The Interaction between Homogeneous Gas-Phase and Heterogeneous Surface Reactions," Chem. Vap. Depos., **4**(4), pp. 151–158.

[70] Williams, K. R., Gupta, K., and Wasilik, M., 2003, "Etch Rates for Micromachining Processing - Part II," J. Microelectromechanical Syst., **12**(6), pp. 761–778.

[71] Schrlau, M. G., 2009, "Carbon-Based Nanoprobes for Cell Nanosurgery & Biological Applications," University of Pennsylvania.

[72] Grachev, M. A., Annenkov, V. V., and Likhoshway, Y. V., 2008, "Silicon Nanotechnologies of Pigmented Heterokonts," BioEssays, **30**(4), pp. 328–337.

[73] Pollock, D. D., 1991, *Thermocouples: Theory and Properties*.

[74] Datta, S., 2005, *Quantum Transport: Atom to Transistor*, Cambridge University Press.

[75] Bulusu, A., and Walker, D. G., 2008, "Review of Electronic Transport Models for Thermoelectric Materials," Superlattices Microstruct., **44**(1), pp. 1–36.

[76] Hill, D. E., Williams, L., Mah, G., and Bradley, W. L., 1977, "The Effect of

Physical Vapor Deposition Parameters on the Thermoelectric Power of Thin Film Molybdenum-Nickel Junctions," Thin Solid Films, **40**(C), pp. 263–270.

[77] Zhang, W., Brongersma, S. H., Richard, O., Brijs, B., Palmans, R., Froyen, L., and Maex, K., 2004, "Influence of the Electron Mean Free Path on the Resistivity of Thin Metal Films," *Microelectronic Engineering*, Elsevier, pp. 146–152.

[78] Shrestha, R., Choi, T. Y., Chang, W., and Kim, D., 2011, "A High-Precision Micropipette Sensor for Cellular-Level Real-Time Thermal Characterization," Sensors, **11**(9), pp. 8826–8835.

[79] Beckman, P., Roy, R. P., Velidandla, V., and Capizzano, M., 1993, "A Fast-Response Microthermocouple," Rev. Sci. Instrum., **64**(10), pp. 2947–2951.

[80] Huo, X., Xu, J., Wang, Z., Yang, F., and Xu, S., 2016, "Performance of Nano-Submicron-Stripe Pd Thin-Film Temperature Sensors," Nanoscale Res. Lett., **11**(1).

[81] Zhang, J., Wang, W., Liu, D., Zhang, Y., and Shi, P., 2018, "Structural and Electric Response of ITO/In2O3 Transparent Thin Film Thermocouples Derived from RF Sputtering at Room Temperature," J. Mater. Sci. Mater. Electron., **29**(23), pp. 20253–20259.

[82] Allen, P. B., Rodriguez, I., Kuyper, C. L., Lorenz, R. M., Spicar-Mihalic, P., Kuo, J. S., and Chiu, D. T., 2003, "Selective Electroless and Electrolytic Deposition of Metal for Applications in Microfluidics: Fabrication of a Microthermocouple," Anal. Chem., **75**(7), pp. 1578–1583.

[83] Shapira, E., Marchak, D., Tsukernik, A., and Selzer, Y., 2008, "Segmented Metal Nanowires as Nanoscale Thermocouples," Nanotechnology, **19**(12).

[84] Brandner, J. J., 2019, “In-Situ Measurements in Microscale Gas Flows-Conventional Sensors or Something Else?,” Micromachines, **10**(5), p. 292.

[85] Fish, G., Bouevitch, O., Kokotov, S., Lieberman, K., Palanker, D., Turovets, I., and Lewis, A., 1995, “Ultrafast Response Micropipette-Based Submicrometer Thermocouple,” Rev. Sci. Instrum., **66**(5), pp. 3300–3306.

[86] Kakuta, N., Suzuki, T., Saito, T., Nishimura, H., and Mabuchi, K., 2001, “Measurement of Microscale Bio-Thermal Responses by Means of a Micro-Thermocouple Probe,” Annu. Reports Res. React. Institute, Kyoto Univ., **3**(c), pp. 3114–3117.

[87] Watanabe, M. S., Kakuta, N., Mabuchi, K., and Yamada, Y., 2005, “Micro-Thermocouple Probe for Measurement of Cellular Thermal Responses,” *Annual International Conference of the IEEE Engineering in Medicine and Biology - Proceedings*, pp. 4858–4861.

[88] Shrestha, R., Choi, T.-Y., Chang, W., and Kim, D., 2011, “A High-Precision Micropipette Sensor for Cellular-Level Real-Time Thermal Characterization,” Sensors, **11**(9), pp. 8826–8835.

[89] Zhang, H., Xiao, X., Su, T., Gu, X., Jin, T., Du, L., and Tang, J., 2014, “A Novel Thermocouple Microelectrode for Applications in SECM and Variable Temperature Electrochemistry,” Electrochem. commun., **47**, pp. 71–74.

[90] Srinivas, T. A. S., Timans, P. J., Butcher, R. J., and Ahmed, H., 1993, “Thermal and Infrared Performance of a Free-Standing Microthermocouple,” Rev. Sci. Instrum., **64**(12), pp. 3602–3611.

[91] Bai, T., and Gu, N., 2016, “Micro/Nanoscale Thermometry for Cellular Thermal

Sensing," Small, **12**(34), pp. 4590–4610.

[92] Gavriloaia, G. V., Hurduc, A., Ghimigean, A.-M., and Fumarel, R., 2009, "Spatial-Temperature High Resolution Map for Early Cancer Diagnosis," *Multimodal Biomedical Imaging IV,* SPIE, p. 71710W.

[93] Wust, P., Hildebrandt, B., Sreenivasa, G., Rau, B., Gellermann, J., Riess, H., Felix, R., and Schlag, P., 2002, "Hyperthermia in Combined Treatment of Cancer," Lancet Oncol., **3**(8), pp. 487–497.

[94] Arai, S., Lee, S. C., Zhai, D., Suzuki, M., and Chang, Y. T., 2014, "A Molecular Fluorescent Probe for Targeted Visualization of Temperature at the Endoplasmic Reticulum," Sci. Rep., **4**.

[95] Homma, M., Takei, Y., Murata, A., Inoue, T., and Takeoka, S., 2015, "A Ratiometric Fluorescent Molecular Probe for Visualization of Mitochondrial Temperature in Living Cells," Chem. Commun., **51**(28), pp. 6194–6197.

[96] Sakaguchi, R., Kiyonaka, S., and Mori, Y., 2015, "Fluorescent Sensors Reveal Subcellular Thermal Changes," Curr. Opin. Biotechnol., **31**, pp. 57–64.

[97] Wang, X. D., Wolfbeis, O. S., and Meier, R. J., 2013, "Luminescent Probes and Sensors for Temperature," Chem. Soc. Rev., **42**(19), pp. 7834–7869.

[98] Shrestha, R., Choi, T. Y., Han, C. S., Chang, W. S., and Kim, S. Y., 2012, "Measurement of Thermal Conductivity of Thin and Thick Films Based on Micropipette Thermocouple," Intersoc. Conf. Therm. Thermomechanical Phenom. Electron. Syst. ITHERM, pp. 1052–1058.

[99] Völklein, F., and Kessler, D. P. E., 1987, "Methods for the Measurement of Thermal Conductivity and Thermal Diffusivity of Very Thin Films and Foils,"

Measurement, **5**(1), pp. 38–45.

[100] Desiatov, B., Goykhman, I., and Levy, U., 2014, “Direct Temperature Mapping of Nanoscale Plasmonic Devices,” Nano Lett., **14**(2), pp. 648–652.

[101] Maciá-Barber, E., 2015, *Thermoelectric Materials: Advances and Applications*, Pan Stanford Publishing Pte. Ltd.

[102] *SPI-Module Sputter Coater Instructio Manual*, Toronto, Canada.

[103] Rowe, D. M., ed., 2005, *Thermoelectrics Handbook: Macro to Nano*, CRC Press.

[104] Chen, M., Lu, S. S., and Liao, B., 2005, “On the Figure of Merit of Thermoelectric Generators,” J. Energy Resour. Technol. Trans. ASME, **127**(1), pp. 37–41.

[105] Baltes, H., Paul, O., and Brand, O., 1998, “Micromachined Thermally Based CMOS Microsensors,” Proc. IEEE, **86**(8), pp. 1660–1678.

[106] Clausmeyer, J., and Schuhmann, W., 2016, “Nanoelectrodes: Applications in Electrocatalysis, Single-Cell Analysis and High-Resolution Electrochemical Imaging,” TrAC - Trends Anal. Chem., **79**, pp. 46–59.

[107] Fan, Y., Han, C., and Zhang, B., 2016, “Recent Advances in the Development and Application of Nanoelectrodes,” Analyst, **141**(19), pp. 5474–5487.

[108] Hao, R., and Zhang, B., 2016, “Nanopipette-Based Electroplated Nanoelectrodes,” Anal. Chem., **88**(1), pp. 614–620.

[109] An, T., Choi, W. S., Lee, E., Kim, I. tae, Moon, W., and Lim, G., 2011, “Fabrication of Functional Micro- and Nanoneedle Electrodes Using a Carbon Nanotube Template and Electrodeposition,” Nanoscale Res. Lett., **6**(1), pp. 1–6.

[110] Shao, Y., Mirkin, M. V., Fish, G., Kokotov, S., Palanker, D., and Lewis, A., 1997, “Nanometer-Sized Electrochemical Sensors,” Anal. Chem., **69**(8), pp. 1627–1634.

[111] Johnson, T. W., Lapin, Z. J., Beams, R., Lindquist, N. C., Rodrigo, S. G., Novotny, L., and Oh, S. H., 2012, “Highly Reproducible Near-Field Optical Imaging with Sub-20-Nm Resolution Based on Template-Stripped Gold Pyramids,” ACS Nano, **6**(10), pp. 9168–9174.

[112] Schrlau, M. G., Brailoiu, E., Patel, S., Gogotsi, Y., Dun, N. J., and Bau, H. H., 2008, “Carbon Nanopipettes Characterize Calcium Release Pathways in Breast Cancer Cells,” Nanotechnology, **19**(32), pp. 17–22.

[113] Anderson, S. E., and Bau, H. H., 2015, “Carbon Nanoelectrodes for Single-Cell Probing,” Nanotechnology, **26**(18), pp. 1–10.

[114] Takahashi, Y., Shevchuk, A. I., Novak, P., Zhang, Y., Ebejer, N., MacPherson, J. V., Unwin, P. R., Pollard, A. J., Roy, D., Clifford, C. A., Shiku, H., Matsue, T., Klenerman, D., and Korchev, Y. E., 2011, “Multifunctional Nanoprobes for Nanoscale Chemical Imaging and Localized Chemical Delivery at Surfaces and Interfaces,” Angew. Chemie - Int. Ed., **50**(41), pp. 9638–9642.

[115] Singhal, R., Orynbayeva, Z., Venkat, R., Sundaram, K., Jie Niu, J., Bhattacharyya, S., Vitol, E. A., Schrlau, M. G., Papazoglou, E. S., Friedman, G., and Gogotsi, Y., 2011, “Multifunctional Carbon-Nanotube Cellular Endoscopes,” Nanotechnology, **6**, pp. 57–64.

[116] Cox, J. T., and Zhang, B., 2012, “Nanoelectrodes: Recent Advances and New Directions,” Annu. Rev. Anal. Chem., **5**(1), pp. 253–272.

[117] Anderson, S. E., and Bau, H. H., 2014, “Electrical Detection of Cellular Penetration during Microinjection with Carbon Nanopipettes,” Nanotechnology, **25**(24), p. 245102.

[118] Rees, H. R., Anderson, S. E., Privman, E., Bau, H. H., and Venton, B. J., 2015, “Carbon Nanopipette Electrodes for Dopamine Detection in Drosophila,” Anal. Chem., **87**(7), pp. 3849–3855.

[119] Willman, K. W., and Murray, R. W., 1983, “Contact Angle Bewteen Water and a Poly(Vinylferrocene) Film on a Potential-Controlled Platinum Electrode,” Anal. Chem, **55**(7), p. 4.

[120] Schröder, U., Wadhawan, J. D., Compton, R. G., Marken, F., Suarez, P. A. Z., Consorti, C. S., De Souza, R. F., and Dupont, J., 2000, “Water-Induced Accelerated Ion Diffusion: Voltammetric Studies in 1-Methyl-3-[2,6-(S)-Dimethylocten-2-Yl]Imidazolium Tetrafluoroborate, 1-Butyl-3-Methylimidazolium Tetrafluoroborate and Hexafluorophosphate Ionic Liquids,” New J. Chem., **24**(12), pp. 1009–1015.

[121] Yum, K., Cho, H. N., Hu, J., and Yu, M.-F. F., 2007, “Individual Nanotube-Based Needle Nanoprobes for Electrochemical Studies in Picoliter Microenvironments,” ACS Nano, **1**(5), pp. 440–448.

[122] Kashyap, R., and Gratzl, M., 1998, “Electrochemistry in Microscopic Domains. 1. The Electrochemical Cell and Its Voltammetric and Amperometric Response,” Anal. Chem., **70**(8), pp. 1468–1476.

[123] Penner, R. M., Heben, M. J., Longin, T. L., and Lewis, N. S., 1990, “Fabrication and Use of Nanometer-Sized Electrodes in Electrochemistry,” Science (80-.)., **250**(4984), pp. 1118–1121.

[124] Li, X., Majdi, S., Dunevall, J., Fathali, H., and Ewing, A. G., 2015, “Quantitative Measurements of Transmitters in Vesicles One at a Time in Single Cell Cytoplasm

with Nano-Tip Electrodes ** HHS Public Access," Angew Chem Int Ed Engl, **54**(41), pp. 11978–11982.

[125] Comstock, D. J., Elam, J. W., Pellin, M. J., and Hersam, M. C., 2003, "Integrated Ultramicroelectrode-Nanopipet Probe for Concurrent Scanning Electrochemical Microscopy and Scanning Ion Conductance Microscopy," Phys. Chem. Chem. Phys, **209**(11), p. 12.

[126] Zheng, X. T., Hu, W., Wang, H., Yang, H., Zhou, W., and Li, C. M., 2011, "Bifunctional Electro-Optical Nanoprobe to Real-Time Detect Local Biochemical Processes in Single Cells," Biosens. Bioelectron., **26**(11), pp. 4484–4490.

[127] Pendley, B. D., and Abruna, H. D., 1990, "Construction of Submicrometer Voltammetric Electrodes," J. Electroanal. Chem. Interfacial Electro-chem, **62**(16), pp. 2692–2699.

[128] Li, Y., Bergman, D., and Zhang, B., 2002, "Preparation and Electrochemical Response of 1−3 Nm Pt Disk Electrodes," J. Electroanal. Chem, **14**(1), pp. 5496–5502.

[129] Yang, C., and Sun, P., 2009, "Fabrication and Characterization of a Dual Submicrometer-Sized Electrode," Anal, **81**(17), pp. 7496–7500.

[130] Angle, M. R., and Schaefer, A. T., 2012, "Neuronal Recordings with Solid-Conductor Intracellular Nanoelectrodes (SCINEs)," PLoS One, **7**(8), p. e43194.

[131] da Silva, R. A. B., Rabelo, A. C., Munoz, R. A. A., and Richter, E. M., 2010, "Three-Electrode-Integrated Sensor into a Micropipette Tip," Electroanalysis, **22**(19), pp. 2167–2171.

[132] Miller, T. S., Macpherson, J. V., and Unwin, P. R., 2014, "Dual-Electrode

Measurements in a Meniscus Microcapillary Electrochemical Cell Using a High Aspect Ratio Carbon Fibre Ultramicroelectrode," J. Electroanal. Chem., **729**, pp. 80–86.

[133] Zaks, A., and Klibanov, A. M., 1988, "Enzymatic Catalysis in Nonaqueous Solvents.," J. Biol. Chem., **263**(7), pp. 3194–3201.

[134] Clark, R. A., Hietpas, P. B., and Ewing, A. G., 1997, "Electrochemical Analysis in Picoliter Microvials," Anal. Chem., **69**(2), pp. 259–263.

[135] Troyer, K. P., and Wightman, R. M., 2002, "Dopamine Transport into a Single Cell in a Picoliter Vial," Anal. Chem., **74**(20), pp. 5370–5375.

[136] Gao, N., Zhao, M., Zhang, X., and Jin, W., 2006, "Measurement of Enzyme Activity in Single Cells by Voltammetry Using a Microcell with a Positionable Dual Electrode," Anal. Chem., **78**(1), pp. 231–238.

[137] Waleed Shinwari, M., Zhitomirsky, D., Deen, I. A., Selvaganapathy, P. R., Jamal Deen, M., and Landheer, D., 2010, "Microfabricated Reference Electrodes and Their Biosensing Applications," Sensors, **10**(3), pp. 1679–1715.

[138] Wang, S., Meng, X., Zhou, H., Liu, Y., Secundo, F., and Liu, Y., 2016, "Enzyme Stability and Activity in Non-Aqueous Reaction Systems: A Mini Review," Catalysts, **6**(2).

[139] Golshadi, M., Maita, J., Lanza, D., Zeiger, M., Presser, V., and Schrlau, M. G., 2014, "Effects of Synthesis Parameters on Carbon Nanotubes Manufactured by Template-Based Chemical Vapor Deposition," Carbon N. Y., **80**(1), pp. 28–39.

[140] Scheibel, O. V., Lanza, D., and Schrlau, M. G., 2017, "Template-Based Synthesis of Integrated Carbon Micro- and Nanostructures," *ASME International*

Mechanical Engineering Congress and Exposition, Proceedings (IMECE).

[141] Yin, H., Ma, Q., Zhou, Y., Ai, S., and Zhu, L., 2010, "Electrochemical Behavior and Voltammetric Determination of 4-Aminophenol Based on Graphene-Chitosan Composite Film Modified Glassy Carbon Electrode," Electrochim. Acta, **55**(23), pp. 7102–7108.

[142] 2014, "227 4-Aminophenol In Acetaminophen-Containing Drug Products," *United States Pharmacopeia 37 - National Formulary 32*.

[143] 2008, *European Pharmacopoeia*, Council of Europe.

[144] Scandurra, G., Antonella, A., Ciofi, C., Saitta, G., and Lanza, M., 2014, "Electrochemical Detection of P-Aminophenol by Flexible Devices Based on Multi-Wall Carbon Nanotubes Dispersed in Electrochemically Modified Nafion," Sensors (Switzerland), **14**(5), pp. 8926–8939.

[145] Benavente, R., Lopez-Tejedor, D., Perez-Rizquez, C., and Palomo, J. M., 2018, "Ultra-Fast Degradation of p-Aminophenol by a Nanostructured Iron Catalyst," Molecules, **23**(9).

[146] Zhou, Y., Ino, K., Shiku, H., and Matsue, T., 2015, "Evaluation of Senescence in Individual MCF-7 Spheroids Based on Electrochemical Measurement of Senescence-Associated β-Galactosidase Activity," Electrochim. Acta, **186**, pp. 449–454.

[147] Laczka, O., Ferraz, R. M., Ferrer-Miralles, N., Villaverde, A., Muñoz, F. X., and Campo, F. J. del, 2009, "Fast Electrochemical Detection of Anti-HIV Antibodies: Coupling Allosteric Enzymes and Disk Microelectrode Arrays," Anal. Chim. Acta, **641**(1–2), pp. 1–6.

[148] Laczka, O., García-Aljaro, C., del Campo, F. J., Pascual, F. X. M., Mas-Gordi, J., and Baldrich, E., 2010, "Amperometric Detection of Enterobacteriaceae in River Water by Measuring β-Galactosidase Activity at Interdigitated Microelectrode Arrays," Anal. Chim. Acta, **677**(2), pp. 156–161.

[149] Sharma, S. K., and Leblanc, R. M., 2017, "Biosensors Based on β-Galactosidase Enzyme: Recent Advances and Perspectives," Anal. Biochem., **535**, pp. 1–11.

[150] Jamal, M., Sarac, A. S., and Magner, E., 2004, "Conductive Copolymer-Modified Carbon Fibre Microelectrodes: Electrode Characterisation and Electrochemical Detection of p-Aminophenol," Sensors Actuators, B Chem., **97**(1), pp. 59–66.

[151] Chia, X., Ambrosi, A., and Pumera, M., 2014, "Redox Reaction of P-Aminophenol at Carbon Nanotube Electrodes Is Accelerated by Carbonaceous Impurities," Electrochem. commun., **38**, pp. 1–3.

[152] Dimri, G. P., Lee, X., Basile, G., Acosta, M., Scott, G., Roskelley, C., Medrano, E. E., Linskens, M., Rubelj, I., Pereira-Smith, O., Peacocke, M., and Campisi, J., 1995, "A Biomarker That Identifies Senescent Human Cells in Culture and in Aging Skin in Vivo," Proc. Natl. Acad. Sci. U. S. A., **92**(20), pp. 9363–9367.

[153] Yang, X., and Gao, Z., 2015, "Enzyme-Catalysed Deposition of Ultrathin Silver Shells on Gold Nanorods: A Universal and Highly Efficient Signal Amplification Strategy for Translating Immunoassay into a Litmus-Type Test," Chem. Commun., **51**(32), pp. 6928–6931.

[154] Sezgintürk, M. K., and Dinçkaya, E., 2008, "β-Galactosidase Monitoring by a Biosensor Based on Clark Electrode: Its Optimization, Characterization and Application," Biosens. Bioelectron., **23**(12), pp. 1799–1804.

[155] Chen, J., Jackson, A., Rotello, V., and Nugen, S., 2016, “Colorimetric Detection of Escherichia Coli Based on the Enzyme- Induced Metallization of Gold Nanorods Juhong,” Small, **12**(18), pp. 2469–2475.

[156] Biran, I., Klimentiy, L., Hengge-Aronis, R., Ron, E. Z., and Rishpon, J., 1999, “On-Line Monitoring of Gene Expression,” Microbiology, **145**(8), pp. 2129–2133.

[157] Mássen, M., Liu, Z., Haruyama, T., Kobatake, E., Ikariyama, Y., and Aizawa, M., 1995, “Immunosensing with Amperometric Detection, Using Galactosidase as Label and P-Aminophenyl-β-D-Galactopyranoside as Substrate,” Anal. Chim. Acta, **304**(3), pp. 353–359.

[158] Zhao, C., Sinha, J., Wijayawardhana, C., and Wittstock, G., 2004, “Monitoring β-Galactosidase Activity by Means of Scanning Electrochemical Microscopy,” J. Electroanal. Chem. - J ELECTROANAL CHEM, **561**, pp. 83–91.

[159] Tschirhart, T., Zhou, X. Y., Ueda, H., Tsao, C. Y., Kim, E., Payne, G. F., and Bentley, W. E., 2016, “Electrochemical Measurement of the β-Galactosidase Reporter from Live Cells: A Comparison to the Miller Assay,” ACS Synth. Biol., **5**(1), pp. 28–35.

[160] Bard, A. J., and Faulkner, L. R., 2000, *Electrochemical Methods: Fundamentals and Applications*, John Wiley & Sons.

[161] Sezgintürk, M. K., and Dinçkaya, E., 2011, “A Biosensor for the Determination of β-Galactosidase Activity: A Different Viewpoint on Biosensors,” Artif. Cells, Blood Substitutes, Biotechnol., **39**(5), pp. 281–288.

[162] Jian, T.-R., Periasamy, A. P., Hsu, N.-Y., Wu, W.-P., Harroun, S. G., and Chang, H.-T., 2017, “Quantitation of β-Galactosidase and E. Coli through Electrochemical

Oxidation of Glucose on CuO/Cu2O/Ppy Paper Electrode," Sensors Actuators B Chem., **253**, pp. 1063–1070.

[163] Spring, S. A., Goggins, S., and Frost, C. G., 2017, "Ratiometric Electrochemical Detection of β-Galactosidase," Org. Biomol. Chem., **15**(34), pp. 7122–7126.

[164] Barton, Z. J., and Rodríguez-López, J., 2014, "Lithium Ion Quantification Using Mercury Amalgams as in Situ Electrochemical Probes in Nonaqueous Media," Anal. Chem., **86**(21), pp. 10660–10667.

[165] Aoki, K., 1993, "Theory of Ultramicroelectrodes," Electroanalysis, **5**, pp. 627–639.

[166] Li, Y., Cox, J. T., and Zhang, B., 2010, "Electrochemical Responses and Electrocatalysis at Single Au Nanoparticles," J. Am. Chem. Soc., **132**(9), pp. 3047–3054.

[167] Sun, P., Laforge, F. O., Abeyweera, T. P., Rotenberg, S. A., Carpino, J., and Mirkin, M. V., 2008, "Nanoelectrochemistry of Mammalian Cells," Proc. Natl. Acad. Sci. U. S. A., **105**(2), pp. 443–448.

[168] Katemann, B. B., and Schuhmann, W., 2002, "Fabrication and Characterization of Needle-Type," Electroanalysis, **14**(1), pp. 22–28.

[169] Krapf, D., Quinn, B. M., Wu, M.-Y., Zandbergen, H. W., Dekker, C., and Lemay, S. G., 2006, "Experimental Observation of Nonlinear Ionic Transport at the Nanometer Scale," Nano Lett., **6**(11), pp. 2531–2535.

[170] Randviir, E. P., 2018, "A Cross Examination of Electron Transfer Rate Constants for Carbon Screen-Printed Electrodes Using Electrochemical Impedance Spectroscopy and Cyclic Voltammetry," Electrochim. Acta, **286**, pp. 179–186.

[171] Marcus, R. A., 1956, “On the Theory of Oxidation-Reduction Reactions Involving Electron Transfer. I,” J. Chem. Phys., **24**(5), pp. 966–978.

[172] Filik, H., Aydar, S., and Avan, A. A., 2015, “Poly(2,2′-(1,4-Phenylenedivinylene) Bis-8-Hydroxyquinaldine) Modified Glassy Carbon Electrode for the Simultaneous Determination of Paracetamol and p-Aminophenol,” Anal. Lett., **48**(16), pp. 2581–2596.

[173] Tohidinia, M., Biabangard, A., and Noroozifar, M., 2020, “Platinized Agarose Microspheres as a New Modifier in Graphite Paste Electrodes for the Electrochemical Determination of 4-Aminophenol,” RSC Adv., **10**(5), pp. 2944–2951.

[174] Xin, Q., and Wightman, R. M., 1997, “Enzyme Modified Amperometric Sensors for Choline and Acetylcholine with Tetrathiafulvalene Tetracyanoquinodimethane as the Electron-Transfer Mediator,” Anal. Chim. Acta, **341**(1), pp. 43–51.

[175] Li, Y., Hu, K., Yu, Y., Rotenberg, S. A., Amatore, C., and Mirkin, M. V., 2017, “Direct Electrochemical Measurements of Reactive Oxygen and Nitrogen Species in Nontransformed and Metastatic Human Breast Cells,” J. Am. Chem. Soc., **139**(37), pp. 13055–13062.

[176] Adkins, J. A., Noviana, E., and Henry, C. S., 2016, “Development of a Quasi-Steady Flow Electrochemical Paper-Based Analytical Device,” Anal. Chem., **88**(21), pp. 10639–10647.

[177] Viratelle, O. M., and Yon, J. M., 1973, “Nucleophilic Competition in Some Beta-Galactosidase-Catalyzed Reactions,” Eur. J. Biochem., **33**(1), pp. 110–116.

[178] Moore, J. P., Williams, R. K., and Graves, R. S., 1977, “Thermal Conductivity,

Electrical Resistivity, and Seebeck Coefficient of High-Purity Chromium from 280 to 1000 K," J. Appl. Phys., **48**(2), pp. 610–617.

[179] "Sputter Coater Targets" [Online]. Available: https://www.emsdiasum.com/microscopy/products/vacuum/targets.aspx#91006. [Accessed: 12-May-2020].

[180] Pan, H., Zhang, H., Lai, J., Gu, X., Sun, J., Tang, J., and Jin, T., 2017, "Integration of Thermocouple Microelectrode in the Scanning Electrochemical Microscope at Variable Temperatures: Simultaneous Temperature and Electrochemical Imaging and Its Kinetic Studies," Sci. Rep., **7**(1), pp. 1–6.

[181] Morag, A., Golub, T., Becker, J., and Jelinek, R., 2016, "High Surface Area Electrodes by Template-Free Self-Assembled Hierarchical Porous Gold Architecture," J. Colloid Interface Sci., **472**, pp. 84–89.

[182] Arroyo-Currás, N., Scida, K., Ploense, K. L., Kippin, T. E., and Plaxco, K. W., 2017, "High Surface Area Electrodes Generated via Electrochemical Roughening Improve the Signaling of Electrochemical Aptamer-Based Biosensors," Anal. Chem., **89**(22), pp. 12185–12191.

[183] Movilli, J., Kolkman, R. W., Rozzi, A., Corradini, R., Segerink, L. I., and Huskens, J., 2020, "Increasing the Sensitivity of Electrochemical DNA Detection by a Micropillar-Structured Biosensing Surface," Langmuir, **36**(16), pp. 4272–4279.

Appendix: Publications

[1] **Scheibel, O. V**., and Schrlau, M. G., 2020, “A Self-Contained Two-Electrode Nanosensor for Electrochemical Analysis in Aqueous Microenvironments,” Electroanalysis, p. elan.201900672.

[2] **Scheibel, O. V**., Lanza, D., and Schrlau, M. G., 2017, “Template-Based Synthesis of Integrated Carbon Micro- and Nanostructures,” ASME International Mechanical Engineering Congress and Exposition, Proceedings (IMECE).

[3] **Scheibel, O. V**, and Schrlau, M. G., 2017, “Carbon Nanotube-Based Sensors: Overview,” Comprehensive Biomaterials II, P. Ducheyne, ed., Elsevier, Oxford, United Kingdom, pp. 690–702.